

DIGITAL ACCESS TO SCHOLARSHIP AT HARVARD

Directional Optical Antennas, Wafer-Scale Metasurfaces, and Single Molecule Surface-Enhanced Raman Scattering

The Harvard community has made this article openly available. Please share how this access benefits you. Your story matters.

Citation	Wang, Dongxing. 2013. Directional Optical Antennas, Wafer-Scale Metasurfaces, and Single Molecule Surface-Enhanced Raman Scattering. Doctoral dissertation, Harvard University.
Accessed	April 17, 2018 4:23:26 PM EDT
Citable Link	http://nrs.harvard.edu/urn-3:HUL.InstRepos:11181066
Terms of Use	This article was downloaded from Harvard University's DASH repository, and is made available under the terms and conditions applicable to Other Posted Material, as set forth at http://nrs.harvard.edu/urn-3:HUL.InstRepos:dash.current.terms-of-use#LAA

(Article begins on next page)

Directional Optical Antennas, Wafer-Scale Metasurfaces, and Single Molecule Surface-Enhanced Raman Scattering

A dissertation presented

by

Dongxing Wang

to

The School of Engineering and Applied Sciences

in partial fulfillment of the requirements

for the degree of

Doctor of Philosophy

in the subject of

Engineering Sciences

Harvard University

Cambridge, Massachusetts

September 2013

© 2013 - Dongxing Wang

All rights reserved.

Directional Optical Antennas, Wafer-Scale Metasurfaces, and Single Molecule Surface-Enhanced Raman Scattering

Abstract

Within the field of optics, one of the topics being currently investigated with considerable interest is that of plasmonics, which refers to the use of surface plasmons on metallic nanostructures to manipulate light. It can be argued that this has been largely driven by two reasons. First, surface plasmons enable light to be concentrated into deep sub-wavelength regions, and therefore provide a means for overcoming the diffraction limit, which states that light can be focused to dimensions no smaller than roughly half the wavelength. Second, recent years have seen rapid development in nanofabrication methods – largely driven by applications in silicon microelectronics – that permit the realization of the metallic nanostructures needed for plasmonics. The goal of this thesis has been to harness these recent dramatic advances in plasmonics to address a long-standing problem in optics: the fact that Raman scattering cross sections are very small.

In Chapter 1, we lay out the fundamentals of surface plasmon polaritons (SPPs), localized surface plasmons (LSPs), Raman scattering, and surface-enhanced Raman scattering (SERS), in order to place contributions of this thesis into context.

In Chapter 2, we investigate the optimal design of optical antennas. These refer to antennas that operate at optical frequencies, and are employed throughout this thesis due

to their ability to concentrate light into nanoscale regions. We primarily investigate these with the application of surface-enhanced Raman scattering in mind. Optical antenna designs comprising pairs of metallic nanoparticles with different shapes are studied, using electromagnetic simulations performed via the finite difference time domain (FDTD) method. The concepts of charge and current reservoirs are introduced.

In Chapter 3, we continue our investigations on the optimal design of optical antennas, with an emphasis on improving directionality. We specifically consider the case of a device consisting of a pair of gold nanoparticles surrounded by concentric gold rings, all above a gold mirror. We perform simulations showing that the SERS enhancement in this design is two orders of magnitude higher than that of the basic design, consisting solely of a pair of gold nanoparticles. These simulations take the realistic case of focused illumination.

In Chapter 4, we experimentally demonstrate a substrate that achieves very high SERS performance. It consists of an array of pairs of gold nanoparticles with gaps well below 10 nm and a one-dimensional array of gold strips. These formed above a gold film, with a dielectric spacer layer between them. We perform simulations that show that the device achieves local electric field enhancements that are far higher than those of the basic design, consisting solely of pairs of gold nanoparticles on a glass substrate. Our experimental results reveal average SERS enhancement factor of 1.2×10^{10}, representing an increase of about two orders of magnitude over the basic design.

In Chapter 5, we demonstrate, for the first time to the best of our knowledge, single molecule SERS using a top-down fabricated chip that contains multiple hot-spot producing nanostructures (optical antennas). Our chip consists of pairs of closely-spaced

silver nanoparticles surrounded by silver rings. These are formed above a silver film, with a dielectric spacer layer between them. We perform electromagnetic simulations that predict very strong electric field intensity enhancement that is ~two orders of magnitude higher than that of the basic design, consisting of pairs of silver nanoparticles on an SiO_2 substrate. We experimentally verify that the chip achieves single molecule SERS (SMSERS) sensitivity via the isotopologue method. The experimental results show that the fraction of optical antennas on the chip that achieve single molecule sensitivity is near unity. We furthermore measure, again for the first time to the best of our knowledge, the far-field emission patterns of SERS from single molecules on the optical antennas.

In Chapter 6, we present experimental results on metasurfaces. One of key developments in optics over the past decade has been that of metamaterials. These typically comprise dielectric or metallic nanostructures in a regular array throughout a three-dimensional region that enable the realization of a bulk electromagnetic behavior that may be difficult or impossible to obtain otherwise. The term “metasurface” has come to refer to the case where these nanostructures are formed at a surface. We demonstrate a metasurface that achieves the near-total absorption of light at visible wavelengths. We demonstrate the SERS detection of single molecules on the metasurface, enabled by the strong electric field enhancement it generates. The metasurface consists of silver islands formed above a silver mirror, with an SiO_2 spacer layer between them. Because these are formed via the standard fabrication techniques of evaporation and sputtering, the metasurfaces are formed on a wafer scale in highly economical fashion. We discuss the interpretation of the physics underlying the perfect absorption phenomenon, and accompanying field enhancement.

Contents

List of Publications

Journal papers

Dongxing Wang, Wenqi Zhu, Michael D. Best, Jon P. Camden, and Kenneth B. Crozier, "Wafer-scale metasurface for total power absorption, local field enhancement and single molecule Raman spectroscopy," submitted (2013)

Dongxing Wang, Wenqi Zhu, Michael D. Best, Jon P. Camden, and Kenneth B. Crozier, "Directional Raman scattering from single molecules in the feed gaps of optical antennas," Nano Letters vol. 13, p.p 2194–2198 (2013)

Dongxing Wang, Wenqi Zhu, Yizhuo Chu and Kenneth B. Crozier, "High directivity optical antenna substrates for surface enhanced Raman scattering," Advanced Materials vol. 24, pp. 4376–4380 (2012)

Dongxing Wang, Tian Yang, and Kenneth B. Crozier, "Optical antennas integrated with concentric ring gratings: electric field enhancement and directional radiation," Optics Express, vol. 19, Issue 3, pp. 2148-2157 (2011)

Dongxing Wang, Tian Yang, and Kenneth B. Crozier, "Charge and current reservoirs for electric and magnetic field enhancement," Optics Express, vol. 18, Issue 10, pp. 10388-10394 (2010)

Tal Ellenbogen, **Dongxing Wang** and Kenneth B. Crozier, "Generation of quasi-coherent cylindrical vector beams by leaky mirrorless laser," Optics Express vol. 20, pp. 28862-28870 (2012)

Wenqi Zhu, **Dongxing Wang** and Kenneth B. Crozier, "Direct observation of beamed Raman scattering," Nano Letters vol. 12, pp. 6235-6243 (2012)

Yizhuo Chu, **Dongxing Wang,** Wenqi Zhu, and Kenneth B. Crozier, "Double resonance surface enhanced Raman scattering substrates: an intuitive coupled oscillator model," Optics Express, vol. 19, Issue 16, pp. 14919-14928 (2011)

Baoan Liu, **Dongxing Wang,** Chuan Shi, Kenneth B. Crozier, and Tian Yang, "Vertical optical antennas integrated with spiral ring gratings for large local electric field enhancement and directional radiation," Optics Express, vol. 19, Issue 11, pp. 10049-10056 (2011)

Kenneth B. Crozier, Wenqi Zhu, **Dongxing Wang,** Shiyun Lin, Michael D. Best and Jon P. Camden, "Plasmonics for surface enhanced raman scattering: nanoantennas for single molecules," Journal of Selected Topics in Quantum Electronics, accepted (2013)

Yizhuo Chu, Wenqi Zhu, **Dongxing Wang,** and Kenneth B. Crozier, "Beamed Raman: directional excitation and emission enhancement in a plasmonic crystal double resonance SERS substrate," Optics Express, vol. 19, Issue 21, pp. 20054-20068 (2011)

Wenqi Zhu, Mohamad G. Banaee, **Dongxing Wang,** Yizhuo Chu, and Kenneth B. Crozier, "Lithographically fabricated optical antennas with gaps well below 10 nm," Small vol. 7, pp. 1761-1766 (2011).

Conference presentations

Dongxing Wang, Wenqi Zhu and Kenneth B. Crozier, "Silver islands over mirror for surface enhanced Raman scattering: large area, low cost and high performance," The 6th International Conference on Surface Plasmon Photonics (SPP6) Conference, Ottawa, Canada 2013

Dongxing Wang, Wenqi Zhu, Yizhuo Chu, Michael D. Best, Jon P. Camden, and Kenneth B. Crozier, "Single molecule surface enhanced Raman spectroscopy with an optical antenna chip," Conference on Laser and Electro-Optics (CLEO) 2012, San Jose, CA, Paper QM3H.1

Dongxing Wang, Wenqi Zhu, Yizhuo Chu, and Kenneth B. Crozier, "Optical antennas integrated with gratings and reflectors for surface enhanced Raman scattering," The 5th International Conference on Surface Plasmon Photonics (SPP5) Conference, Busan, Korea 2011, paper ThD-3

Dongxing Wang, Tian Yang, and Kenneth B. Crozier, "Modified surface Plasmon antenna for localized field enhancement," Conference on Laser and Electro-Optics/International Quantum Electronics Conference (CLEO/IQEC) 2009, Baltimore, MD

Wenqi Zhu, **Dongxing Wang** and Kenneth B. Crozier, "Surface-enhanced Raman scattering from plasmonic dimers with gap widths in the quantum regime," The 6th International Conference on Surface Plasmon Photonics (SPP6) Conference, Ottawa, Canada 2013

Tal Ellenbogen, **Dongxing Wang** and Kenneth B. Crozier, "Stimulated Emission of cylindrical vector beams from a dye-doped slab waveguide," Frontiers in Optics 2012, Rochester, NY, paper FTh4D.1

Wenqi Zhu, **Dongxing Wang,** Yizhuo Chu, and Kenneth B. Crozier, "Collimation of Raman scattering with plasmonic structures," Conference on Laser and Electro-Optics (CLEO) 2012, San Jose, CA, Paper QF2D.6

List of Contributions

1. We propose and study (with simulations) two new types of optical antennas. The first is termed the fan-rod antenna, and uses the concept of charge reservoirs to achieve large electric field enhancement. The second is a loop-shaped antenna with offsets, and uses the concept of current reserviors concept to achieve large magnetic field enhancement.
2. We propose and study (with simulations) a means for increasing the excitation field and collimating the Raman emission available from optical antennas (pairs of metal nanoparticles separated by small gaps). The method consists of integrating the optical antennas with concentric ring gratings.
3. We propose, simulate, fabricate and test a plasmonic chip for surface-enhanced Raman scattering (SERS). The chip consists of optical antennas (pairs of gold nanoparticles with sub-10 nm gaps) integrated with a one-dimensional array of gold strips and a gold mirror. A very large SERS enhancement factor (up to 1.2×10^{10}) is experimentally demonstrated.
4. We propose, simulate, fabricate and test a plasmonic chip for SERS. The chip contains thousands of optical antennas. Each antenna consists of a pair of silver nanoparticles, surrounded by a silver ring, and above a silver mirror. The optical antenna chip is experimentally verified to achieve single molecule SERS (SMSERS) sensitivity using the isotopologue method. This represents the first time, to the best of our knowledge, that SMSERS has been demonstrated with a chip containing multiple top-down fabricated structures. We also demonstrate, for the first time to the best of our knowledge, the directional emission patterns of Raman scattering from single

molecules.

5. We demonstrate metasurfaces, produced in a wafer scale fashion using a simple lithography-free process, consisting of silver islands formed above a silver mirror. The fabricated metasurfaces are experimentally demonstrated to act as near-perfect optical absorbers at visible wavelengths. We furthermore show that these enable SMSERS sensitivity. The near-perfect absorption phenomenon (and accompanying large local field enhancement) is interpreted with the aid of simulations.

Acknowledgments

I first want to express my deepest gratitude to my advisor Prof. Kenneth Crozier for his thoughtful guidance, systematic training, patience, consideration and encouragement during my study. From him, I have not only obtained knowledge and skills related to nano-optics, but also more importantly he has shaped my attitude toward science and research. He made my doctoral study and research at Harvard an enjoyable experience.

I would like to thank Prof. Lene Hau, Prof. Evelyn Hu, and Prof. Marko Lončar for serving on my research advising committee. They have given me much useful advice during my stay in Harvard.

I would like to thank my friends and colleagues in Prof. Crozier's group. It has been wonderful to study and work with them. I appreciate all the help and support they have given. Especially, I thank Dr. Tian Yang, Dr. Yizhuo Chu, Dr. Tal Ellenbogen, Dr. Kai Wang, Dr. Shiyun Lin, Dr. Yaping Dan, Mr. Wenqi Zhu, Mr. Antony Orth and Mr. Hyunsung Park.

I would like to thank our collaborators at the University of Tennessee. Prof. Michael Best and Prof. Jon Camden offered us generous help in making isotopologues available to us for experiments. I have also benefited from discussions with them.

I would like to thank the Harvard CNS staff, including Dr. Yuan Lu, Dr. Ling Xie, Mr. Ed Macomber, Dr. Jiangdong Deng, Dr. Dave Lange, and Mr. Mac Hathaway. The training they provided to me, and the maintenance they have performed on the nanofabrication and imaging instruments, have made it possible for me to fabricate the plasmonic devices in this thesis.

I give my thanks to my wife, Xuying Zheng. We have together shared happiness

and frustration over the past ten years. Her support, her encouragement and her love have made my doctoral study possible.

Finally, I would like to thank my parents, Jianhua Gao and Yubo Wang, my parents in law, Bixian Yang and Shimin Zheng, and my sister, Julia Chung for their love and support.

1 Introduction

1.1 Overview

The term “plasmonics” has come to refer to the use of surface plasmons on metallic nanostructures to manipulate light on a sub-wavelength scale [1]. Surface plasmons are coherent electron oscillations that exist at the interface between any two materials across which the real part of the permittivity changes sign. When a surface plasmon couples with a photon, a hybridized excitation results that is called a surface plasmon polariton (SPP). Surface plasmons enable electric fields to be strongly enhanced on a sub-wavelength scale, and this thesis employs this phenomenon for surface enhanced Raman scattering (SERS). In this Chapter, we aim to provide a background on the fundamentals of plasmonics and of SERS, in order to place the results of this thesis in context. The goal is to provide simple classical models that aid with physical interpretation.

The topic of plasmonics is one of the areas of optics that currently holds the greatest interest, yet we note that it dates back to ancient times when metallic nanoparticles were used to produce stained glass. One of the most famous examples of plasmonics is the Lycurgus cup [2] that, being of the Byzantine period, is more than 1500 years old. When viewed with a light source on the outside of the cup, it appears green, due to strong scattering of light by the metallic nanoparticles that are embedded in the glass from which it is formed. On the other hand, if the light source is placed inside the cup, it appears red when viewed from outside. This is due to modification of the transmission spectrum of the glass by the absorption of light by the particles. The

underlying physical phenomenon was not of course understood in these ancient times. Two key works were performed approximately one hundred years ago that proved to be important advances in the understanding of plasmonics. Arnold Sommerfeld described the mathematics underlying the propagation of radio waves on the surface of a conductor with finite loss [3], a problem that bears considerable similarity to that of the propagation of SPPs. Gustav Mie formulated the solution to scattering of electromagnetic waves by a sphere [4], a problem of direct relevance to the excitation of localized surface plasmons (LSPs) on metallic nanoparticles. Another key development occurred in the 1950s, when Rufus Ritchie recorded the energy loss for electrons passing through thin metal foils and linked the energy loss with plasmons occuring on the surface of the metal [5].

The field of plasmonics is currently attracting considerable interest, ranging from fundamental studies to commercial applications. A comprehensive review of the field is beyond the scope of this Chapter, but examples include studies on sensing [6-9], waveguiding [10-14], metamaterials [15-18], solar cells [19-22], near-field optics [23-27], high-density optical data storage [28-30], quantum effects [31-33] and surface-enhanced Raman scattering [34-38].

The overarching themes of my research are on the design and fabrication of plasmonics devices that enhance and spatially confine electromagnetic fields for surface enhanced Raman scattering (SERS). SERS refers to the phenomenon in which Raman scattering from molecules in the vicinity of metallic nanostructures is enhanced [39]. SERS presents a means for identifying molecules through their “fingerprint” vibrational spectra [37, 38]. The boost in the Raman scattering is largely due to the local fields being strongly increased in the vicinity of the surface of the nanostructure [40-42]. Recent years

have therefore seen considerable interest in maximizing this field enhancement [43-53]. In this thesis, we study various means by which the field enhancement can be increased, including by optimizing the shape of the nanoparticles that comprise the optical antenna, by integrating these devices with metallic gratings, and by harnessing the related phenomenon of perfect optical absorption. We study how to engineer the device to maximize directionality, in order to improve the collection efficiency. We furthermore develop methods for producing large area substrates with good performance in a highly economical fashion.

1.2 Optical properties of metals

Most plasmonic devices, especially those operating at optical frequencies, use metals. In this section we therefore consider a classical model that describes the permittivities of metals.

We begin by considering the Drude-Sommerfield model [54-56] of a metal as consisting of a gas of free electrons and a rigid ionic lattice. An equation of motion of an electron of the free-electron gas is given by:

$$m^* \frac{d^2 \bar{r}}{d^2 t} + m^* \gamma \frac{d\bar{r}}{dt} = -e\bar{E}_0 \exp(-i\omega t) \qquad (1.1)$$

where m^* is the effective mass of free electrons, γ is the damping coefficient describing the electron scattering, $-e$ is the charge of the electron and $\bar{E}_0 \exp(-i\omega t)$ is the external driving field. Taking the electron position as $\vec{r}(t) = \vec{r}_0 e^{-i\omega t}$, we rewrite Equation (1.1) as:

$$-\omega^2 m^* \bar{r} + -i\omega m^* \gamma \bar{r} = -e\bar{E}_0 \qquad (1.2)$$

Using this equation, we obtain the macroscopic polarization of the metal to be

$$\bar{P} = -ne\bar{r} = -\frac{ne^2}{m^*(\omega^2 + i\gamma\omega)}\bar{E}_0 \qquad (1.3)$$

where n is the density of electrons. From the polarization, we obtain the dispersive permittivity as

$$\varepsilon(\omega) = 1 - \frac{\omega_p^2}{\omega^2 + i\gamma\omega} = (1 - \frac{\omega_p^2}{\omega^2 + \gamma^2}) + i\frac{\gamma\omega_p^2}{\omega(\omega^2 + \gamma^2)} \qquad (1.4)$$

where ω_p is the plasma frequency, defined as $\omega_p = \sqrt{\frac{ne^2}{m^*\varepsilon_0}}$. The plasma frequencies of metals are in the ultraviolet and visible portions of the electromagnetic spectrum. The real part of the permittivity is therefore negative at frequencies smaller than ω_p, i.e. at visible and infrared wavelengths. The complex refractive index is given by the square root of the permittivity, i.e. $n = \sqrt{\varepsilon}$. A negative permittivity therefore means that the refractive index will have a substantial imaginary component. This in turn means that a plane wave will penetrate the metal with an extent that is limited, and will be strongly reflected. The imaginary part of the permittivity represents energy dissipation associated with motion of the electrons in the metal.

The Drude-Sommerfield model gives accurate results for the optical properties of metals at long wavelengths. At shorter wavelengths, such as in the visible, the assumption that only the free electrons need to be modeled is no longer valid, as there can be interband transitions [1]. This results in a substantial deviation between the permittivity predicted by the Drude-Sommerfeld model, and that measured experimentally, e.g. by Johnson and Christy [57]. To address this, the response of the bound electrons is modeled as the sum of Lorentz oscillators [58]. The approach is similar to that employed when

considering the free electrons, but with an additional term that describes a restoring force:

$$m_l \frac{d^2\bar{r}}{d^2t} + m_l\gamma_l \frac{d\bar{r}}{dt} + K\bar{r} = -e\bar{E}_0 \exp(-i\omega t) \qquad (1.5)$$

where m_l is the effective mass of bond electrons, γ_l is the damping constant of bond electrons and K is the spring constant representing the potential that keeps the electrons in place. As before, we assume that the electron position is given by $\vec{r}(t) = \vec{r}_0 e^{-i\omega t}$, and obtain

$$\bar{P} = -\tilde{n}e\bar{r} = \varepsilon_0 \frac{\tilde{\omega}_p^2}{(\omega_0^2 - \omega^2 + i\gamma\omega)} \bar{E}_0 \qquad (1.6)$$

where $\tilde{n}$ is the density of the bound electrons, $\tilde{\omega}_p = \sqrt{\frac{\tilde{n}e^2}{m_l\varepsilon_0}}$ is defined along similar lines to the plasma frequency, and $\omega_0 = \sqrt{\frac{K}{m_l}}$. The contribution of the bound electrons to the metal permittivity is then found from Equation (1.6) to be:

$$\varepsilon_l = \frac{\tilde{\omega}_p^2}{(\omega_0^2 - \omega^2 + i\gamma\omega)} \qquad (1.7)$$

Combining the contributions of free and bound electrons to the metal permittivity, we obtain

$$\varepsilon(\omega) = 1 - \frac{\omega_p^2}{\omega^2 + i\gamma\omega} + \sum_b \frac{\tilde{\omega}_{pb}^2}{(\omega_{0b}^2 - \omega^2 + i\gamma_b\omega)} \qquad (1.8)$$

where the terms in the summation are the contributions of different interband transitions of electrons, each modeled as a Lorentz oscillator with parameters $\tilde{\omega}_{pb}$, ω_{0b} and γ_b.

In the following chapters, simulations are performed using the metal permittivity modeling by Equation (1.8), with the parameters chosen to obtain a match with the

experimentally-measured permittivity [57]. We also note that both Drude term and Lorentz terms in Equation (1.8) follow the Kramers-Krönig relation [59], thereby ensuring causality.

1.3 Surface plasmons on planar interfaces

SPPs are the quanta of surface charge density oscillations [1, 10, 60-62]. In Figure 1-1(a), we show a 1D interface between dielectric materials and metal. This interface is a simple structure that supports SPPs. The SPPs are tightly confined to the interface as shown in Figure 1-1(b) and usually have penetration depth on the order of tens of nanometers, e.g. for silver, the penetration depth is 23 nm at a free-space wavelength of $\lambda = 617$ nm.

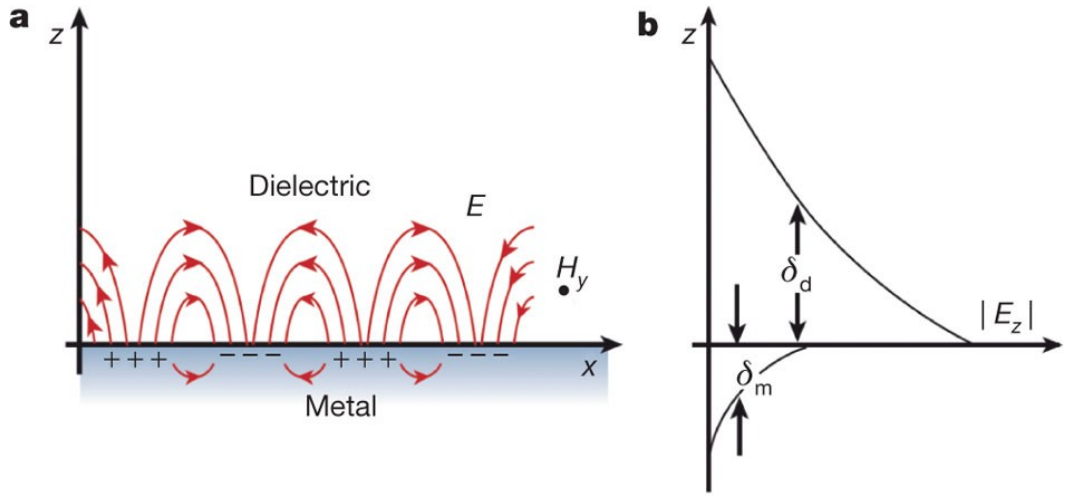

Figure 1-1. (a) SPPs propagating along the interface between metal and dielectric material (from Ref. [63]). Charge and field distributions associated with the SPPs are illustrated schematically. (b) Profile of perpendicular field component $|E_z|$ of SPPs with penetration depths δ_d on the dielectric side and δ_m on the dielectric side, respectively (from Ref. [63]).

To derive the dispersion relation of the SPP shown in Figure 1-1, we use the Maxwell equations with appropriate boundary conditions. The fields on the dielectric and

metal sides are denoted by subscripts 1 and 2, respectively. These subscripts are also used when referring to the constitutive parameters of the dielectric and of the metal. The fields are then given by:

$$\vec{E}_1 = \{\hat{x}E_{x1} + \hat{z}E_{z1}\} \exp[i(k_x x + k_{z1} z)] \qquad (1.9a)$$

$$\vec{H}_1 = \hat{y}H_{y1} \exp[i(k_x x + k_{z1} z)] \qquad (1.9b)$$

$$\vec{E}_2 = \{\hat{x}E_{x2} + \hat{z}E_{z2}\} \exp[i(k_x x + k_{z2} z)] \qquad (1.9c)$$

$$\vec{H}_2 = \hat{y}H_{y2} \exp[i(k_x x + k_{z2} z)] \qquad (1.9d)$$

Boundary conditions require continuity of the tangential components of the electric and magnetic fields across the boundary. These yield:

$$E_{x1} = E_{x2} \qquad (1.10a)$$

$$H_{y1} = H_{y2} \qquad (1.10b)$$

From the Maxwell equations and from the dispersion relation of the k vector in an isotropic medium, we have:

$$E_{x1,2} = \frac{k_{z1,2}}{\omega \varepsilon_{1,2} \varepsilon_0} H_{y1,2} \qquad (1.11a)$$

$$k_{z1,2}^2 + k_x^2 = \omega^2 \mu_0 \varepsilon_0 \varepsilon_{1,2} \qquad (1.11b)$$

Because SPPs are evanescent along the direction perpendicular to the interface, and are bound to it, we obtain

$$ik_{z1} < 0 \qquad (1.12a)$$

$$ik_{z2} > 0 \qquad (1.12b)$$

Using Equation (1.10a) through Equation (1.12b), we obtain the SPP dispersion relation to be:

$$k_x = \frac{\omega}{c}\sqrt{\frac{\varepsilon_1 \varepsilon_2}{\varepsilon_1 + \varepsilon_2}} \qquad (1.13)$$

For the case that the dielectric is free space and the permittivity of metal follows the Drude model of silver, the dispersion relationship of SPPs is as plotted in Figure 1-2.

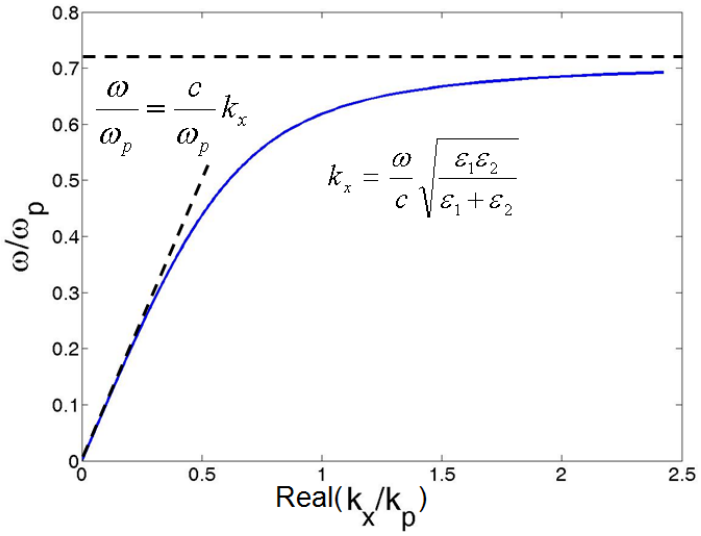

Figure 1-2. Dispersion relation for SPPs at interface between free space and silver (Drude model). Frequency is normalized by plasma frequency ω_p and real part of x component of wave vector k_x is normalized by $k_p = \omega_p / c$.

In Figure 1-2, the light line of the dielectric is also shown as a dashed line. It is seen that there is no intersection between the dispersion curve of SPPs and light line of the dielectric except for at the origin. There is therefore a momentum mismatch between these two curves, meaning that SPPs at the interface cannot be directly excited by shining a plane wave onto the metal from the dielectric side. Instead, prism or grating coupling is often used (Figure 1-3).

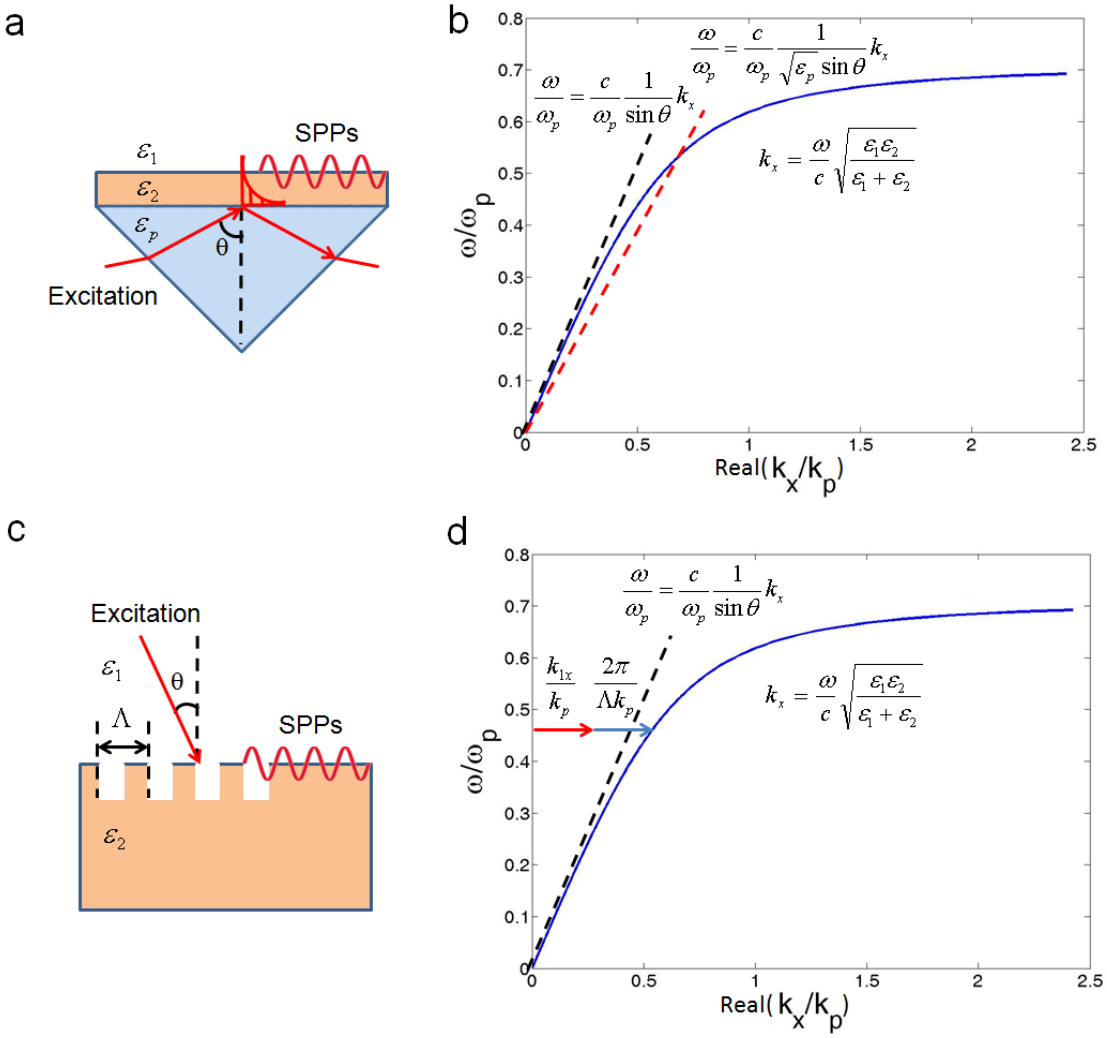

Figure 1-3. (a) Kretschmann configuration using prism for SPPs coupling. (b) Dispersion relationship of SPP, and light lines in free space and in prism. (c) Grating coupler for SPP excitation. Periodicity of grating is Λ. (d) Dispersion relationship of SPPs. Red arrow is normalized tangential component $k_{1x}/k_p = \omega\sin(\theta)/(ck_p)$ of wave vector of excitation wave. Blue arrow is normalized reciprocal lattice vector $G/k_p = 2\pi/(\Lambda k_p)$ of grating.

In the prism (or Kretschmann) configuration (Figure 1-3a), a prism with refractive index $n_p = \sqrt{\varepsilon_p}$ larger than that of the dielectric (air, $n_d = \sqrt{\varepsilon_1}$) is placed on the back side of the metal layer. The metal layer is thin enough to allow the excitation light from the prism side to be coupled to the dielectric side. Due to the larger refractive index of the prism, as shown in Figure 1-3b, the slope of light line of the prism is smaller than that of

the dielectric. The light line of the prism and the SPP dispersion relationship intersect, meaning that light incident from the prism can indeed excite SPPs at the metal-dielectric (air) interface.

In the scheme of Figure 1-3c, the necessary additional momentum is achieved by a grating that provides a reciprocal lattice vector $G = p\frac{2\pi}{\Lambda}$ (p is integer). When the sum of the tangential component k_{1x} of the wavevector of the excitation light and the reciprocal lattice vector matches the SPP wavevector (Figure 1-3d), SPPs at the metal-dielectric (air) interface can be excited.

The SPP dispersion shown in Figure 1-2 is an idealized one, as the permittivity of silver is taken to follow a simple Drude model. For the case where the dielectric is free space and the permittivity of metal is taken to follow the measured optical properties of silver reported in Ref. [57], the SPP dispersion relationship is as plotted in Figure 1-4.

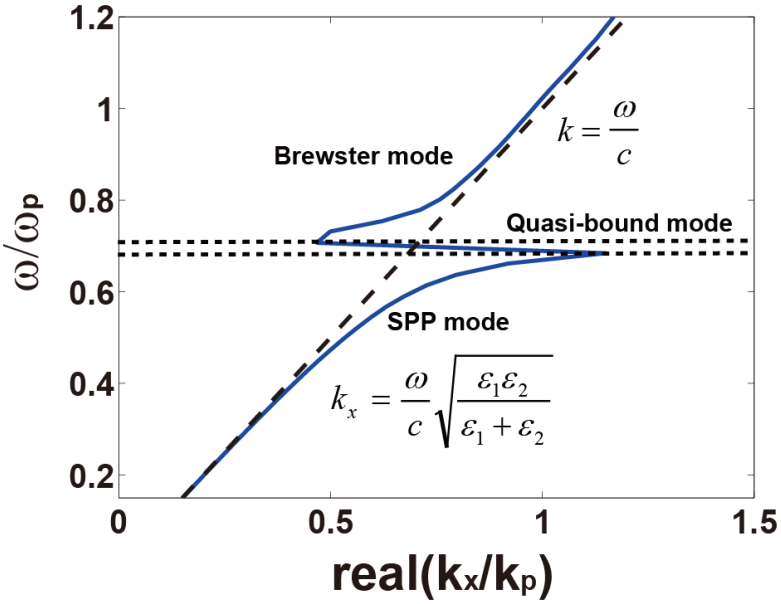

Figure 1-4. Dispersion relation for SPPs at interface between free space and silver (using measured optical properties of Ref. [57]).

From Figure 1-4, it can be seen that the dispersion curve predicted by Equation

(1.13) has three regions. The lower energy (low frequency) branch is the SPP mode that is similar to the mode shown in Figure 1-2. The high energy (high frequency) branch is termed the Brewster mode, and represents the case where the waves are no longer bound to the interface between free space and silver. This branch arises because, at these high frequencies, silver can be considered a lossy dielectric, with the real part of the permittivity being positive. There is a quasi-bound mode ("back bending" effect) connecting the high and low energy branches.

1.4 Localized surface plasmons

In last section, we considered surface plasmon polaritons propagating along, and confined to, the one-dimensional (1D) interface between a metal and a dielectric. It is natural to next consider what happens when this interface is "wrapped" to yield wires or particles that achieve two dimensional (2D) or three dimensional (3D) confinement of surface plasmons. Since these do not usually propagate, they are termed localized surface plasmons (LSPs).

When the dimensions of the wires and particles are much smaller than the excitation free space wavelength, one can use the quasi-static approximation [64] to obtain the field distributions in closed form. Because the contributions of this thesis, as outlined in the remaining chapters, are predominantly to do with nanoparticles (rather than nanowires), we next present the derivation for the surface plasmons on nanospheres. Because this thesis also makes use of nanoparticle arrays and nanoparticles separated by nanoscale gaps, we also present models for understanding the coupling between nanoparticles.

1.4.1 Scattering by nanospheres and ellipsoids

In this section, we consider the case of a nanosphere illuminated by a plane wave (Figure 1-5).

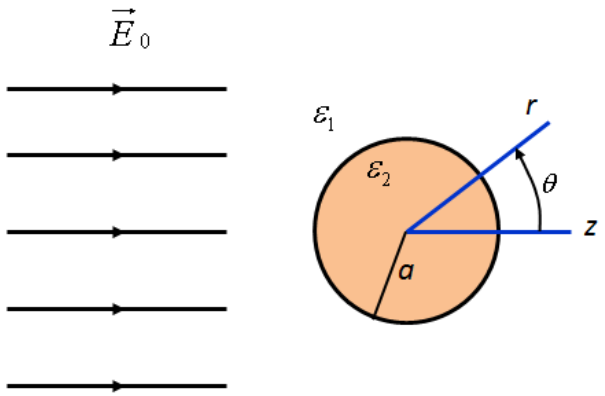

Figure 1-5. Nanosphere is illuminated by a plane wave. a is the radius of the sphere. ε_1 and ε_2 are the permittivities of the surrounding medium and sphere, respectively. r and θ specify the observation point. $\vec{E}_0$ denotes the incident plane wave, with $\vec{E}_0 = \hat{z}E_0$.

Suppose that k is the wavevector of the incident plane wave in the surrounding medium of Figure 1-5. The case where $ka << 1$ corresponds to the quasi-static limit [64]. In the static case, the Faraday's Law reduces to the Laplace equation for the electric potential.

$$\nabla^2 \phi_{1,2} = 0 \qquad (1.14)$$

where the subscripts 1 and 2 denote the outside and inside of the sphere, respectively. The electric fields can be calculated from the potentials as follows:

$$\vec{E}_{1,2} = -\nabla \phi_{1,2} \qquad (1.15)$$

Considering the azimuthal symmetry of the sphere shown in Figure 1-4, the general solution of the potential can be expressed as follows:

$$\phi = \sum (A_l r^l + B_l r^{-(l+1)}) P_l(\cos\theta) \qquad (1.16)$$

where $P_l(\cos\theta)$ is the l th order Legendre polynomial and θ is the angle between

observation direction and the z axis. Because the $r^{-(l+1)}$ terms blow up at the origin and result in non-physical solutions, they are removed from the expression for the potential inside the sphere. The potentials outside and inside the sphere are therefore given by:

$$\phi_1 = \sum (A_l r^l + B_l r^{-(l+1)}) P_l(\cos\theta) \qquad (1.17a)$$

$$\phi_2 = \sum C_l r^l P_l(\cos\theta) \qquad (1.17b)$$

To solve the coefficients in (1.17a) and (1.17b), the following boundary conditions are applied.

$$\lim_{r\to\infty} \phi_1 = -E_0 r\cos\theta \qquad (1.18a)$$

$$\phi_1 = \phi_2 \quad (r = a) \qquad (1.18b)$$

$$\varepsilon_1 \frac{\partial \phi_1}{\partial r} = \varepsilon_2 \frac{\partial \phi_2}{\partial r} \quad (r = a) \qquad (1.18c)$$

Using the above boundary conditions, we obtain the potentials outside and inside the sphere to be

$$\phi_1 = -E_0\, r\cos\theta + a^3\, E_0 \frac{\varepsilon_2 - \varepsilon_1}{\varepsilon_2 + 2\varepsilon_1} \frac{\cos\theta}{r^2} \qquad (1.19a)$$

$$\phi_2 = -\frac{3\varepsilon_1}{\varepsilon_2 + 2\varepsilon_1} E_0\, r\cos\theta \qquad (1.19c)$$

It is seen that the potential outside the sphere is the sum of the potential ($-E_0 r\cos\theta$) due to the incident wave and a potential generated by a dipole located at the origin with dipole moment given by:

$$\overline{p} = \hat{z}p = \hat{z}4\pi\varepsilon_2 \frac{\varepsilon_2 - \varepsilon_1}{\varepsilon_2 + 2\varepsilon_1} a^3\, E_0 = \varepsilon_2 \alpha \vec{E}_0 \qquad (1.20)$$

It can be seen that the dipole moment of the metallic sphere is induced by the incident wav, and is proportional to the incident field. In Equation (1.20), the ease with which the

sphere is polarized is specified by the polarizability α, which is defined by:

$$\alpha = 4\pi a^3 \frac{\varepsilon_2 - \varepsilon_1}{\varepsilon_2 + 2\varepsilon_1} \qquad (1.21)$$

The polarizability will become large when the denominator ($\varepsilon_2 + 2\varepsilon_1$) is small. If the metallic sphere is embedded in free space, the permittivity ε_1 of the outside dielectric is ε_0. For metals, the real part ε_{2r} of the permittivity ε_2 is negative for frequencies smaller than the plasma frequency. As ε_{2r} approaches $-2\varepsilon_0$, the polarizability of the sphere becomes large. The denominator will not be zero however, as the permittivity of the sphere will always have a finite imaginary component.

As shown in Ref. [65], the fields generated by the induced dipole of the nanosphere are given by:

$$E_s(\bar{r}) = \frac{1}{4\pi\varepsilon_1}\{-\frac{\bar{\boldsymbol{p}}}{r^3} + \frac{3\bar{\boldsymbol{r}}[\bar{\boldsymbol{r}}\cdot\bar{\boldsymbol{p}}]}{r^5} + \frac{ik\bar{\boldsymbol{p}}}{r^2} - \frac{3ik\,\bar{\boldsymbol{r}}[\bar{\boldsymbol{r}}\cdot\bar{\boldsymbol{p}}]}{r^4} - \frac{k^2}{r^3}\bar{\boldsymbol{r}}\times[\bar{\boldsymbol{r}}\times\bar{\boldsymbol{p}}]\}e^{i\bar{k}\cdot\bar{r}} \qquad (1.22a)$$

$$H_s(\bar{r}) = \frac{i\omega}{4\pi}\{\frac{1}{r^3} - \frac{ik}{r^2}\}\bar{\boldsymbol{r}}\times\bar{\boldsymbol{p}}\,e^{i\bar{k}\cdot\bar{r}} \qquad (1.22b)$$

In the near field region ($kr << 1$), several terms in Equations (1.22a) and (1.22b) can be dropped. The scattered fields are then given by:

$$E_s(\bar{r}) = \frac{1}{4\pi\varepsilon_1 r^3}\{\,3\hat{r}(\hat{r}\cdot\bar{p}) - \bar{p}\} \qquad (1.23a)$$

$$H_s(\bar{r}) = \frac{i\omega}{4\pi r^2}\{\hat{r}\times\bar{p}\} \qquad (1.23b)$$

In the near field, the ratio of the electric field to the magnetic field is inversely proportional to r. Therefore, near fields can therefore be thought of as predominantly electric in nature. Furthermore, from Equations (1.23a) and (1.23b), we find that the

nanosphere generates a large near field when $\bar{p}$ is on resonance (ε_{2r} approaches $-2\varepsilon_0$). Using finite element method (FEM), we simulate a case that a small sphere made of silver (optical properties as measured in Ref. [57]) in free space is illumated by a plane wave polarized along the *z* direction as shown in Figure 1-5. The simulation shows that the sphere is on resonance at a wavelength of λ=361 nm, at which ε_{2r} approaches $-2\varepsilon_0$. In Figure 1-6, we plot the normalized intensity of the electric fields around the nanosphere at a wavelength of λ=361 nm on the *xz* plane. It can be seen that the nanosphere generates large local fields when it is on resonance. As discussed later, such large local fields are favorable for SERS.

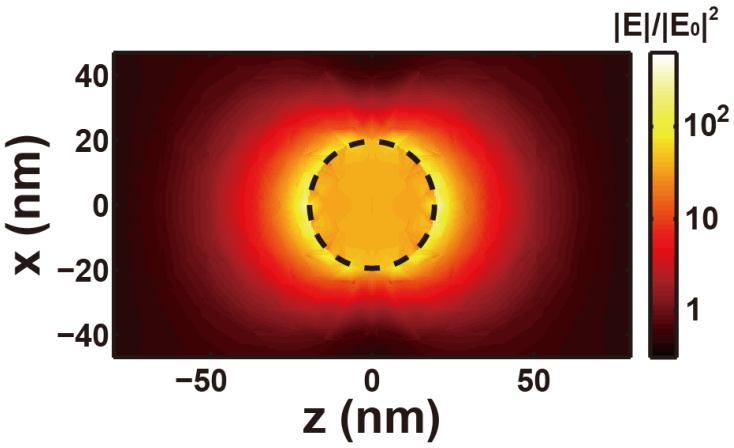

Figure 1-6. Normalized intensity of electric fields around a nanosphere illuminated by a plane wave polarized along *z* direction at a wavelength of λ=361 nm. The radius of the sphere is 20 nm and the center of the sphere is at the origin. The intensity of the electric fields around the nanosphere is normalized by the intensity $|E_0|^2$ of the incident wave. Dashed circle indicates the surface of the sphere.

Similar to the near field region case, in the far-field region ($kr >> 1$), several terms in Equations (1.22a) and (1.22b) can be dropped, yielding

$$E_s(\bar{r}) = \frac{1}{4\pi\varepsilon_1}\frac{1}{ikr}\{-ik^3\,\hat{r}\times(\hat{r}\times\bar{p})\}e^{i\bar{k}\cdot\bar{r}} \quad (1.24a)$$

$$H_s(\bar{r}) = \frac{i\omega}{4\pi}\frac{1}{r}\{-ik\}\,\hat{r}\times\bar{p}\,e^{i\bar{k}\cdot\bar{r}} \qquad (1.24b)$$

By integrating Poynting vectors associated with the scattered and total fields over a surface enclosing the sphere [64], we find the scattering cross section C_{sca} and absorption cross section C_{abs}, respectively. The extinction cross section C_{ext} is given by their sum. The results are as follows.

$$C_{sca} = \frac{k^4}{6\pi}|\alpha|^2 = \frac{8\pi}{3}k^4a^6\left|\frac{\varepsilon_2-\varepsilon_1}{\varepsilon_2+2\varepsilon_1}\right|^2 \qquad (1.25a)$$

$$C_{abs} = k\,\mathrm{Im}(\alpha) = 4\pi ka^3\,\mathrm{Im}\left(\frac{\varepsilon_2-\varepsilon_1}{\varepsilon_2+2\varepsilon_1}\right) \qquad (1.25b)$$

$$C_{ext} = C_{sca} + C_{abs} \qquad (1.25c)$$

It is seen that C_{ext} is dominated by C_{abs} at quasistatic limit ($ka << 1$), since C_{sca} and C_{abs} is propotional to a^6 and a^3, respectively.

As discussed, all the results presented thus far in this section are based on the quasi-static approximation, which requires that the particle is much smaller than the free space wavelength of the incident wave. For larger particles, with sizes comparable with the free space wavelength of the incident wave, the quasi-static approximation is no longer valid and the Mie solution [4] is needed to model the scattering rigorously. From the first order TM mode of the Mie theory, we find sphere polarizability to be given as follows [1]

$$\alpha = \frac{1-\frac{1}{10}(\varepsilon_1+\varepsilon_2)^2A^2+O(A^4)}{\left(\frac{1}{3}-\frac{\varepsilon_1}{\varepsilon_2-\varepsilon_1}\right)-\frac{1}{30}(\varepsilon_2+10\varepsilon_1)A^2-i\frac{4\pi\varepsilon_1^{3/2}}{3}\frac{V}{\lambda_0^3}+O(A^4)}V \qquad (1.26)$$

where λ_0 is the free space wavelength of the incident wave, $A = \frac{\pi a}{\lambda_0}$ is a measure of the sphere size and V is the sphere volume. In the quasi-static limit ($A << 1$), the polarizability as given in Equation (1.26) reduces to the form of Equation (1.21). The term in the numerator that is quadratic in A results from retardation of the incident wave within the sphere. The term in the denominator that is quadratic in A results in the polarizability becoming large at a wavelength that differs from that predicted by the quasi-static approximation. For the spheres made of a metal that can be modeled by a Drude response, the dipole resonance of the sphere red-shifts as A increases.

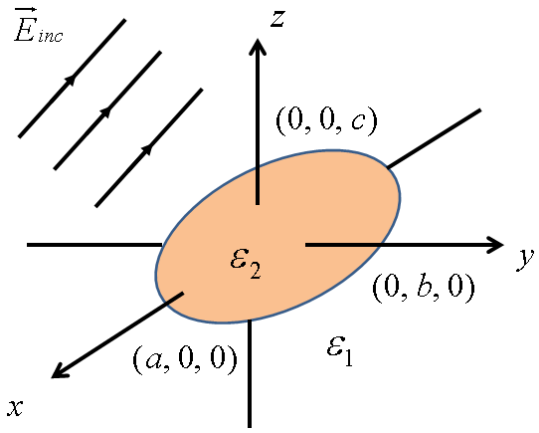

Figure 1-7. Ellipsoid is illuminated by a plane wave. The x, y, and z semi-axes of the ellipsoid are denoted a, b and c. ε_1 and ε_2 are the permittivities of the surrounding medium and of the ellipsoid. $\vec{E}_{inc}$ denotes the electric field of the incident plane wave, where $\vec{E}_{inc} = \hat{x}E_x + \hat{y}E_y + \hat{z}E_z$.

To model nanoparticles with even more general shapes, we next consider the case of an ellipsoid whose outer surface is defined by $\frac{x^2}{a^2} + \frac{y^2}{b^2} + \frac{z^2}{c^2} = 1$. As before, we consider the case of plane wave illumination (Figure 1-7), with the ellipsoid being much smaller than the wavelength of the incident illumination and the quasi-static approximation being therefore applicable. Using methods similar to that shown above for

the nanosphere, the polarizability of the ellipsoid is found to be given by:

$$\alpha = \hat{x}\hat{x}\alpha_x + \hat{y}\hat{y}\alpha_y + \hat{z}\hat{z}\alpha_z \qquad (1.27a)$$

$$\alpha_{x,y,z} = \frac{(\varepsilon_2 - \varepsilon_1)V}{\varepsilon_1 + (\varepsilon_2 - \varepsilon_1)L_{x,y,z}} \qquad (1.27b)$$

$$L_x = \frac{abc}{2}\int_{s=0}^{\infty}(s+a^2)^{-1}[(s+a^2)(s+b^2)(s+c^2)]^{-1/2}\,ds \qquad (1.27c)$$

$$L_y = \frac{abc}{2}\int_{s=0}^{\infty}(s+b^2)^{-1}[(s+a^2)(s+b^2)(s+c^2)]^{-1/2}\,ds \qquad (1.27d)$$

$$L_z = \frac{abc}{2}\int_{s=0}^{\infty}(s+c^2)^{-1}[(s+a^2)(s+b^2)(s+c^2)]^{-1/2}\,ds \qquad (1.27e)$$

where $V\,(=\frac{4\pi}{3}abc)$ is the volume of the ellipsoid. For $a=b=c$, the polarizability of the ellipsoid reduces to that of the sphere (Equation (1.21)).

1.4.2 Coupling between particles

In the last section, we studied the LSP resonances of single particles in homogeneous media, i.e. without any neighbors. It has been shown that the resonances of particles are shifted due to the coupling between particles and that the fields around the particles can be enhanced by the presence of neighboring particles [66-69]. In this section, we consider simple intuitive models for the coupling between particles.

Consider a one-dimensional chain of metallic spheres, equally spaced along the $\hat{x}$ direction with period d (Figure 1-8a)

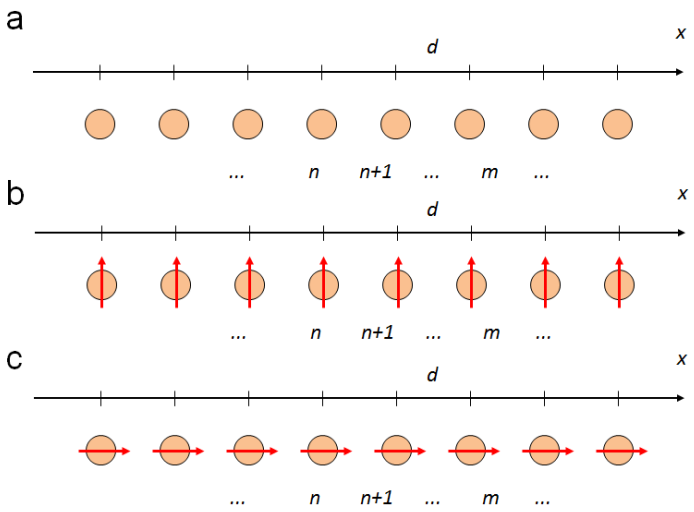

Figure 1-8. (a) Schematic of the array of metallic spheres with equal spacing. (b) Transverse mode of the metallic sphere array. Red arrows show the induced dipoles. (c) Longitudinal mode of the metallic sphere array. Red arrows show the induced dipoles.

As before, we consider the case in which the spheres are much smaller than the free space wavelength of the excitation, meaning that the quasi-static approximation can be applied. Each sphere can therefore be modeled by a dipole. If the spheres are not so close to each that gap modes are formed, the dipole model is to model the fields around the spheres. From Equation (1.22a), the electric field generated by each sphere in the array is given by:

$$E(\bar{\boldsymbol{p}},\bar{\boldsymbol{r}},\omega)=\frac{1}{4\pi\varepsilon_1}\left[(1-\frac{i\omega r}{v})\frac{3(\hat{\boldsymbol{r}}\cdot\bar{\boldsymbol{p}})\hat{\boldsymbol{r}}-\bar{\boldsymbol{p}}}{r^3}+\frac{\omega^2}{v^2}\frac{\bar{\boldsymbol{p}}-(\hat{\boldsymbol{r}}\cdot\bar{\boldsymbol{p}})\hat{\boldsymbol{r}}}{r}\right]e^{i(\omega r/v)} \quad (1.28)$$

where $\bar{\boldsymbol{r}}$ is the observation point, ε_1 is the permittivity of the surrounding medium, and v is the speed of light in the surrounding medium. The dipole moment $\bar{p}$ of the sphere is its polarizability $\alpha(\omega)$ multiplied by the driving field and ε_1. The driving field at each sphere is the sum of the incident wave and the fields generated by the other spheres. This results in the following expression for the dipole moment of the n th sphere:

$$\bar{\boldsymbol{p}}_n = \varepsilon_1 \alpha(\omega)\{\bar{E}_n^{inc} + \frac{1}{4\pi\varepsilon_1}\sum_{m\neq n}\{(1-\frac{i\omega|n-m|d}{v})\frac{3(\hat{\boldsymbol{r}}\cdot\bar{\boldsymbol{p}}_m)\hat{\boldsymbol{r}}-\bar{\boldsymbol{p}}_m}{|n-m|^3 d^3} + \frac{\omega^2}{v^2}\frac{\bar{\boldsymbol{p}}_m-(\hat{\boldsymbol{r}}\cdot\bar{\boldsymbol{p}}_m)\hat{\boldsymbol{r}}}{|n-m|d}e^{i\omega|n-m|d/v}\}\} \quad (1.29)$$

where $\bar{E}_n^{inc}$ is the field of incident wave at the position of the n th sphere.

Here we first consider a transverse mode $\hat{\boldsymbol{x}}\cdot\boldsymbol{p}_n = 0$ of the sphere chain as shown in Figure 1-8b. Furthermore, we assume that the incident wave is a plane wave. The induced dipole moments of the spheres are then given by

$$\bar{\boldsymbol{p}}_n = \bar{\boldsymbol{p}}_0 e^{ink_x d} \quad (1.30)$$

where k_x is the x component of the wave vector. By substituting Equation (1.30) into Equation (1.29), we find the transverse-mode dipole moment of the sphere (without the phase term) to be given by:

$$\bar{\boldsymbol{p}}_0 = \frac{\varepsilon_1 \alpha \bar{E}_n^{inc} e^{-ink_x d}}{\left\{1-\frac{\alpha(\omega)}{4\pi}\sum_{m\neq n}W_{mn}\right\}} \quad (1.31)$$

$$W_{mn} = (1-\frac{i\omega|n-m|d}{v})\frac{-1}{|n-m|^3 d^3} + \frac{\omega^2}{v^2}\frac{1}{|n-m|d}e^{i\omega|n-m|d/v}\}e^{i(m-n)k_x d} \quad (1.32)$$

The dispersion of the transverse mode is determined by the condition that the denominator of Equation (1.31) vanishes, yielding:

$$1+2\frac{\alpha(\omega)}{4\pi d^3}\sum_{j=1}^{\infty}\{(1-\frac{i\omega d}{v}j)\frac{1}{j^3}-\frac{\omega^2}{v^2}\frac{d^2}{j}\}\cos(jk_x d)e^{i\omega jd/v} = 0 \quad (1.33)$$

Following the approaches similar to those above, we find the dispersion of the longitudinal mode (Figure 1-8c) to be given by:

$$1-4\frac{\alpha(\omega)}{4\pi d^3}\sum_{j=1}^{\infty}\{(1-\frac{i\omega d}{v}j)\frac{1}{j^3}\}\cos(jk_x d)e^{i\omega jd/v} = 0 \quad (1.34)$$

For the polarizability $\alpha(\omega)$, we take the polarizability as given by Equation (1.21), but correct for radiation losses [70]. We denote the polarizability as given by Equation (1.21) as α_0. The radiation loss-corrected polarizability is then found from the following equation:

$$\frac{1}{\alpha} = \frac{1}{\alpha_0} - i\frac{2\omega^3}{3c^3} \quad (1.35)$$

The dispersion relations of the transverse and longitudinal modes can be found numerically after plugging Equation (1.35) into Equations (1.33) and (1.34), respectively. We term these the "fully retarded dispersion relations". We present the results of such a calculation. Before doing so however, we present the dispersion relations that result when several approximations are made [71]. As we discuss later, while the resultant dispersion relations differ from those found without making these approximations (i.e. the fully retarded dispersion relations), the results nonetheless provide helpful physical insight. We term these the "quasistatic dispersion relations", but note that several approximations are made (i.e. not just of quasistatic fields). These are discussed as follows. The first approximation is that the inter-particle distances are far smaller than the free space wavelength. A consequence of this assumption is that the near field term ($\frac{1}{r^3}$ term) of the dipole scattering dominates, and Equations (1.33) and (1.34) can be simplied as follows:

$$1 + 2\frac{\alpha(\omega)}{4\pi d^3}\sum_{j=1}^{\infty}\frac{1}{j^3}\cos(jk_x d) = 0 \quad (1.36a)$$

$$1 - 4\frac{\alpha(\omega)}{4\pi d^3}\sum_{j=1}^{\infty}\frac{1}{j^3}\cos(jk_x d) = 0 \quad (1.36b)$$

The spheres in Figure 1-8 are made of silver andthe surrounding medium is glass. We

make the assumption that the silver permittivity follows the Drude model of Equation (1.4), but that there is no damping ($\gamma = 0\ Hz$). We take the plasma frequency as $\omega_p = 8.04 \times 10^{15}\ rad/s$. The further assumption that the nanosphere polarizability need not include radiation loss is also made. Therefore, the sphere polarizability is given by:

$$\alpha = 4\pi a^3 \frac{\omega_0^2}{\omega_0^2 - \omega^2} \quad (1.37)$$

where a is the radius of the sphere and $\omega_0 = \omega_p / \sqrt{3}$. With the above assumptions, Equation (1.36a) and Equation (1.36b) can be simplied to be:

$$\frac{\omega^2}{\omega_0^2} = 1 + 2\frac{a^3}{d^3} \sum_{j=1}^{\infty} \frac{1}{j^3} \cos(jk_x d) \quad (1.38a)$$

$$\frac{\omega^2}{\omega_0^2} = 1 - 4\frac{a^3}{d^3} \sum_{j=1}^{\infty} \frac{1}{j^3} \cos(jk_x d) \quad (1.38b)$$

Equations (1.38a) and (1.38b) are the dispersion relations for the transverse and longitudinal modes of an array containing an infinite number of spheres. In Figure 1-9, these are plotted as the thin solid red curve and thin dashed green curve for the transverse and longitudinal modes, respectively. We take $a = 30\ nm$ and $d = 75\ nm$.

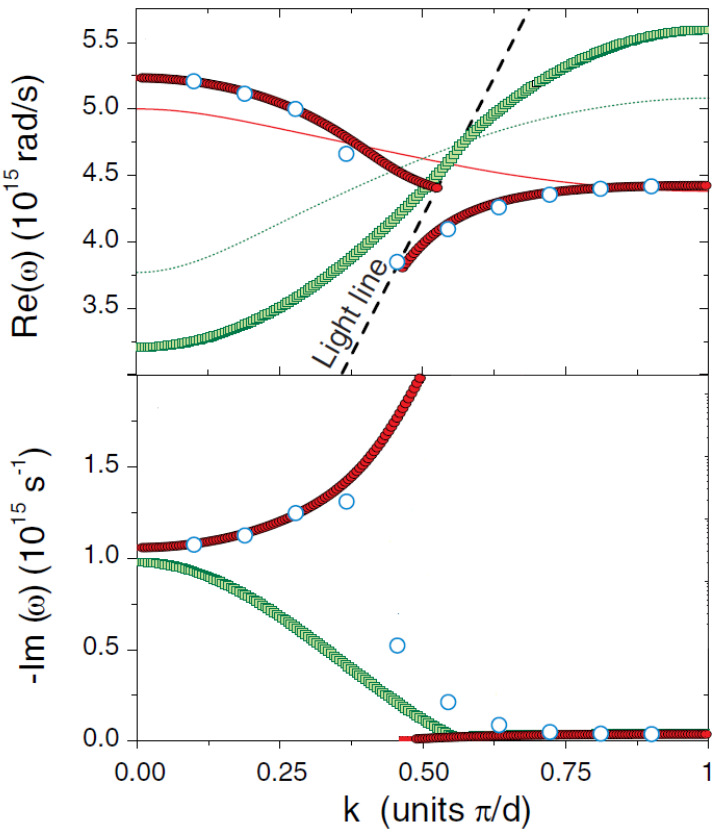

Figure 1-9. Dispersion relations of plasmonic mode for chain of metallic spheres (from Ref. [72]). Solid red curve and dashed green curve plot quasistatic dispersion relations of transverse and longtitudinal modes, respectively, according to model of Equations (1.38a) and (1.38b). Curves comprising red and green squares plot fully retarded dispersion relations of transverse and longitudinal modes, respectively, according to the model of Equations (1.33)-(1.35). Blue circles show the dispersion relation of transverse mode for an array of 10 particles.

In Figure 1-9, the fully retarded dispersion relations, found using Equations (1.33)-(1.35), are also plotted as red and green square symbols. These relations do not make the assumptions of the quastatic dispersion relations discussed in the preceding paragraphs, but rather take into account metal damping, radiation loss and the $1/r$ and $1/r^2$ terms in the electric field from a dipole (Equation 1.28). It can be seen that, despite the substantial approximations made in the quasistatic dispersion relation, there is reasonable qualitative agreement with the fully retarded dispersion relations for small values of k. At larger values, the deviations are pronounced, especially for the transverse mode, for which the

fully-retarded model exhibits two branches, while the quasistatic approximation only shows one. In Figure 1-9, the transverse mode dispersion relation for a chain of ten spheres is also plotted. As the number of spheres is increased, the dispersion relation approaches that of the infinite sphere array case.

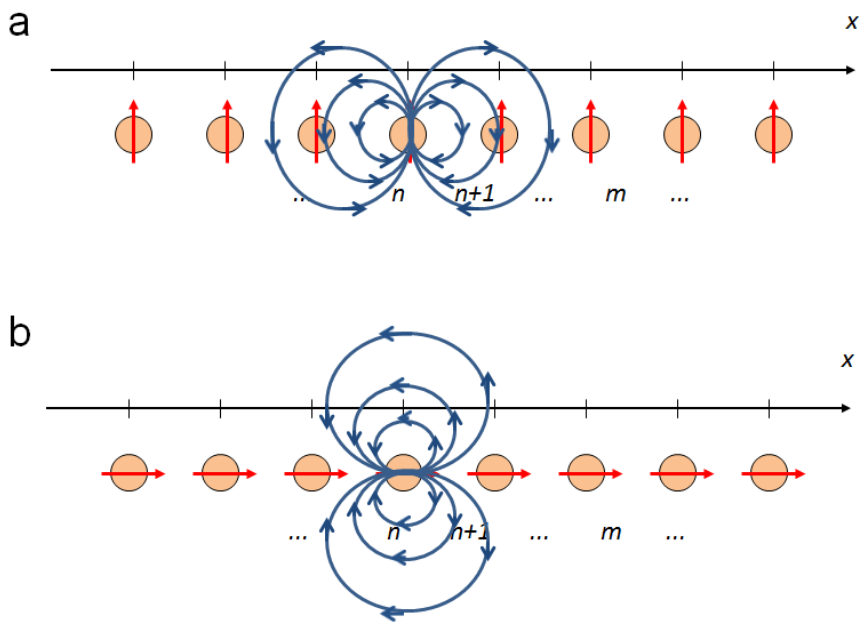

Figure 1-10. (a) Interpretation of transverse mode of chain metallic spheres. Red arrows depict dipole moments, while blue lines depict electric fields generated by sphere n. (b) Interpretation of longitudinal mode.

It is seen from Equation (1.37) that the resonant frequency of the sphere is $\omega_0 = 4.64 \times 10^{15}\ rad/s$, when the coupling between neighbors is not taken into account. Compared with the sphere without neighbors, we find that the resonant frequency of the array is blue-shifted for the transverse mode and red-shifted for the longitudinal mode at $k_x = 0$, which corresponds to the case where the dipole moments of the spheres in the chain are in phase. Our interpretation of this is as follows. It can be seen (Figure 1-10) that, for the transverse mode, the dipole moment of each sphere is out of phase (180 °) with the electric fields generated by its neighbors. It can be similarly seen that, for the

longitudinal mode, the dipole moment of each sphere is in phase with the electric fields generated by its neighbors. The effect of this upon the plasmon resonance frequency can be understood with a mass-and-spring model [73] of LSP on a metal nanoparticle. The equation motion of the electrons in the mass-and-spring model has a similar form to Equation (1.5), but replaces the effective mass m_l of electron in Equation (1.5) with the total mass M of electrons participating in the LSP. The spring in the mass-and-spring model [67] is considered to supply a restoring force to these electrons. For the transverse mode, the fields generated by neighoring spheres are out of phase with the dipole moment of the sphere, i.e. in the same direction as the restoring force from the spring. The restoring force is therefore increased, and the situation can be interpreted as being equivalent to the LSP on an isolated sphere, but with an increased spring constant K. As the resonance frequency is given by $\omega_0 = \sqrt{\frac{K}{M}}$, the transverse mode should have an increased resonance frequency (blue-shift). For the longitudinal mode, the fields generated by the neighbors are in phase of the dipole moment of the sphere, i.e. in the opposite direction to the restoring force from the spring. One can therefore interpret the situation as being equivalent to the LSP on an isolated sphere, but with reduced spring constant K. The resonance frequency of the longitudinal mode is therefore smaller (red-shift) than that of an isolated sphere.

1.4.3 Interaction between LSPRs of metal sphere dimer

In the last section, we studied an array of infinite numbers of nano particles. Here we focus on a simpler structure (Figure 1-11), a dimer composed of a pair of identical

metallic spheres separated by a gap. We study this simpler structure because dimers generate larger enhanced field than isolated particles, which is favorable for SERS [74].

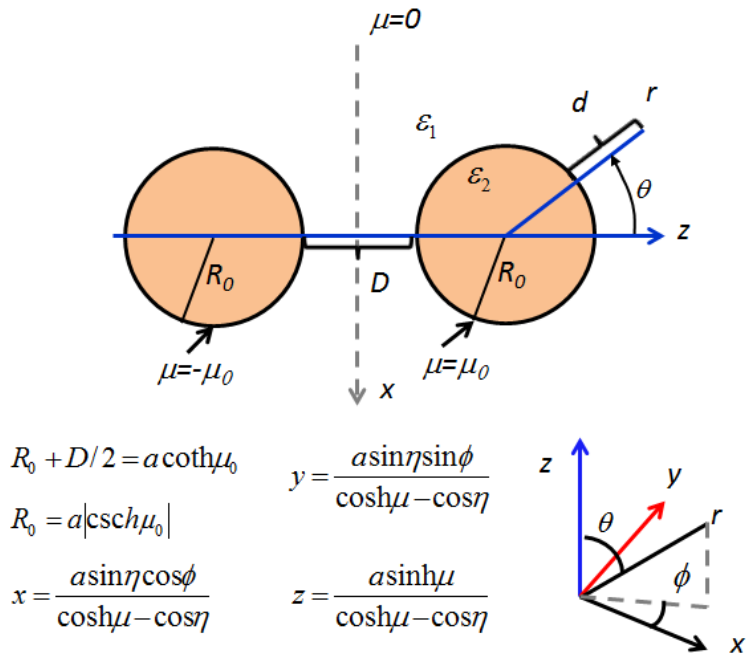

Figure 1-11. Schematic of metal sphere dimer and definition of the bispherical coordinate system (μ,η,ϕ). Note that μ does not refer to permeability. The dimer consist of two identical metallic spheres with radii of R_0 that are separated by a distance of D.

To compare the dimer with isolated particle, we use FEM method to simulate a dimer composed of two identical silver nanospheres with radii of 20 nm, separated by a nanogap of 4 nm. The dimer is illumated by a plane wave propagating along the *y*-direction and polarized along the *z*-direction. The simulations results show that the dimer has two resonances, at wavelengths of λ=397.4 nm (3.13 eV) and λ=359.3 nm (3.46 eV). The resonance at the wavelength of λ=359.3 nm is close to that of the isolated sphere at λ=361 nm (Figure 1-6). This double resonance phenomenon will be discussed later in this section. In Figure 1-12, the intensity enhancement around the dimer at the resonance wavelengths of λ =397.4 nm and λ =359.3 nm are plotted. The peak intensity

enhancements of the dimer are 2.17× 10^4 and 6.35 × 10^3 at λ=397.4 nm and λ=359.3 nm, respectively, which are both much larger than that of the isolated sphere (3.81 × 10^2, Figure 1-6). The simulation results verify that the dimer generates larger field enhancement than the isolated sphere.

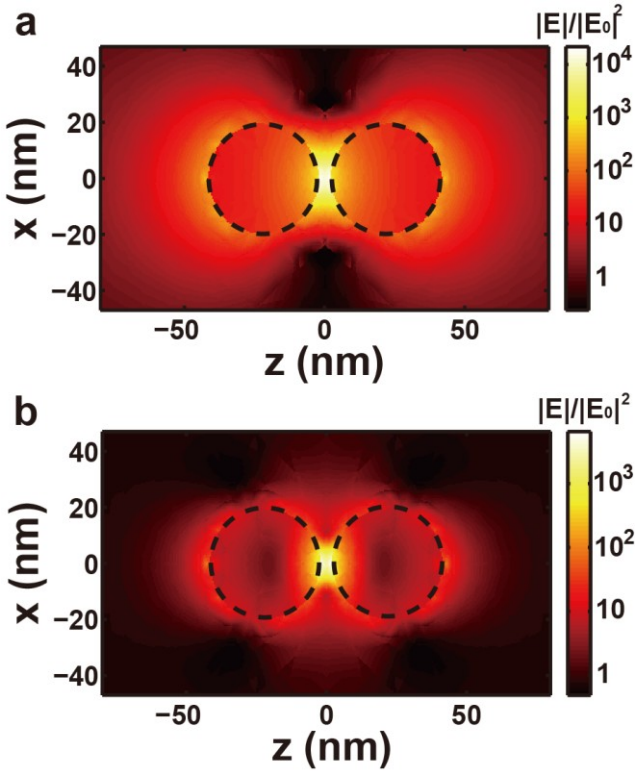

Figure 1-12. Normalized intensity of electric fields around a dimer illuminated by a plane wave polarized along *z* direction and propagating along the *y* direction. The intensity of the electric fields around the dimer is normalized by the intensity $|E_0|^2$ of the incident wave. Dashed circles indicate the surfaces of the spheres. (a) Normalized intensity of electric fields at an illumination wavelength of λ=397.4 nm (3.13 eV). (b) Normalized intensity of electric fields at an illumnation wavelength of λ=359.3 nm (3.46 eV).

To understand the double resonance phenomenon and the large local field enhancement achieved by the dimer, we follow the theorectical model of Ref. [75]. We assume that the silver sphere dimer (Figure 1-11) is illuminated by a plane wave $E_0 e^{-i\omega t}$ whose polarization vector is defined by polar angle $\theta = \theta_0$ and azimuthal angle $\phi = \phi_0$. We assume that the spheres are much smaller than the wavelength of the incident wave.

The quasi static approximation is therefore valid and the Maxwell equations reduce to the Laplace equation. We follow the bispherical coordinate system (μ,η,ϕ) employed in Ref. [75] and shown in Figure 1-11. In this system, the surfaces of the right and left sphere are defined as $\mu=\mu_0$ and $\mu=-\mu_0$, respectively, and the *xy* plane is defined as $\mu=0$. The potentials inside and outside the spheres are then obtained by solving Laplace equation under the bispherical corrdinate system, yielding:

$$\Phi_0=\Phi_{ext}+F\sum_{n\geq|m|}^{\infty}\sum_{m=-\infty}^{\infty}\left\{A_n^m\exp\left[\left(n+\frac{1}{2}\right)\mu\right]+B_n^m\exp\left[-\left(n+\frac{1}{2}\right)\mu\right]\right\}Y_n^m(\cos\eta,\phi) \quad (1.39a)$$

$$\Phi_2=F\sum_{n\geq|m|}^{\infty}\sum_{m=-\infty}^{\infty}C_n^m\exp\left[-\left(n+\frac{1}{2}\right)\mu\right]Y_n^m(\cos\eta,\phi) \quad (1.39b)$$

$$\Phi_1=F\sum_{n\geq|m|}^{\infty}\sum_{m=-\infty}^{\infty}D_n^m\exp\left[\left(n+\frac{1}{2}\right)\mu\right]Y_n^m(\cos\eta,\phi) \quad (1.39c)$$

Φ_0, Φ_1 and Φ_2 are the potentials of outside the spheres, within the left sphere and within the right sphere, repectively. $Y_n^m(\cos\eta,\phi)$ are the spherical harmonics as defined in Ref. [70] and $F=(\cosh\mu-\cos\eta)^{1/2}$. The external potential due to the incident wave is $\Phi_{ext}=-E_0(z\cos\theta_0+x\sin\theta_0\cos\phi_0+y\sin\theta_0\sin\phi_0)e^{-i\omega t}$. To calculate the coefficients A_n^m, B_n^m, C_n^m and D_n^m, the following boundary conditions are applied.

$$\Phi_0\,|_{\mu=\mu_0}=\Phi_2\,|_{\mu=\mu_0} \quad (1.40a)$$

$$\Phi_0\,|_{\mu=-\mu_0}=\Phi_1\,|_{\mu=-\mu_0} \quad (1.40b)$$

$$\varepsilon_1\frac{\partial\Phi_0}{\partial\mu}|_{\mu=\mu_0}=\varepsilon_2\frac{\partial\Phi_2}{\partial\mu}|_{\mu=\mu_0} \quad (1.40c)$$

$$\varepsilon_1\frac{\partial\Phi_0}{\partial\mu}|_{\mu=-\mu_0}=\varepsilon_2\frac{\partial\Phi_1}{\partial\mu}|_{\mu=-\mu_0} \quad (1.40d)$$

The electric field outside the spheres is calculated using

$$E_i = (1/h_i)\frac{\partial \Phi_0}{\partial i}, \quad i = \mu, \eta, \phi \qquad (1.41)$$

The h_i terms are the scale factors for the bisperical coordinate system. From the electric field, we obtain the normalized field intensity to be

$$\tilde{I} = \frac{E_\mu E_\mu^* + E_\eta E_\eta^* + E_\phi E_\phi^*}{E_0 E_0^*} \qquad (1.42)$$

We now show the intensity enhancement predicted by this model for the silver sphere dimer. In Figure 1-13, the normalized field intensities on the surface of the right sphere ($d = 0$) along the observation direction $\theta = 45^o$ and $\phi = 0^o$ are plotted for different values of λ, which here does not denote wavelength, but rather relative gap size.

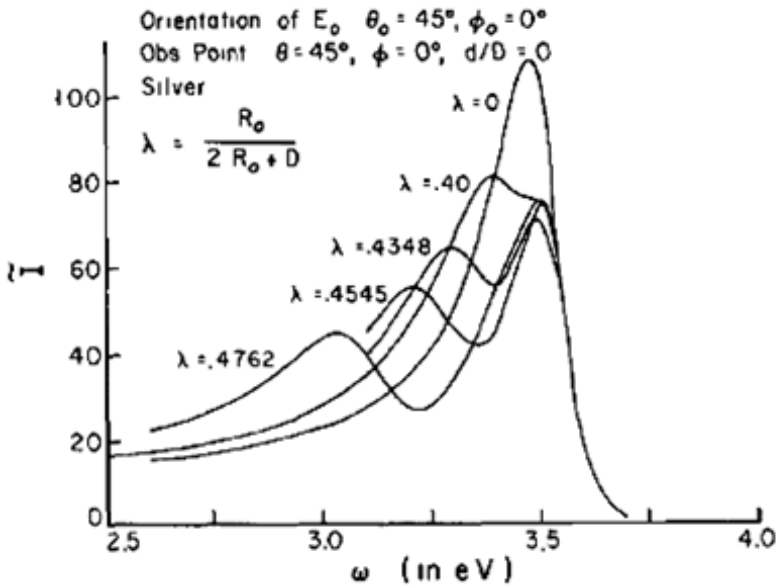

Figure 1-13. Intensity enhancement of silver nanosphere dimer for different scale factors λ (from Ref. [75]).

The case $\lambda = 0$ is for the situation that the spheres are infinitely far from one another, meaning that the spheres act as isolated particles. There is therefore only one LSPR peak ($\omega = 3.48$ eV). This in agreement with the prediction of Equation (1.21) and

of the FEM simulation of Figure 1-6, with only a small difference in predicted resonance frequency. The results of Figure 1-13 show that resonance peak of the isolated particle splits into two peaks as the gap size is decreased. Note that, for spheres with radii of 20 nm, values of λ of 0.4, 0.4348, 0.4545 and 0.4792 correspond to gap widths *D* of 10 nm, 6 nm, 4 nm, and 2 nm, respectively. As pointed out in Ref. [75], this splitting is due to the strong coupling between the two degenerate harmonic oscillators consisting of the left and right spheres. When the two oscillators are coupled to each other, the degenerate resonance modes are replaced by two modes with different frequencies. One is lower than the LSPR frequency of an isolated particle and the other one is close to it. As the distance between two spheres decreases, the coupling between these two spheres increases and the differences between the frequencies of the two new LSPR modes increases (Figure 1-13).

One may get the impression from Figure 1-13 that the peak local field enhancement around the dimer is smaller than of an isolated sphere. This is not the case, as Figure 1-13 plots the normalized field intensities on the surface of the right sphere ($d = 0$) along the observation direction $\theta = 45^o$ and $\phi = 0^o$, rather than peak intensity enhancement, which is in the gap. In Figure 1-14, the normalized field intensities along the *z* axis of the dimer, from one side of the gap to the other, are plotted for a silver sphere dimer with $\lambda = 0.4545$. For spheres with radii of 20 nm, the case of $\lambda = 0.4545$ corresponds to the gap between spheres being 4 nm. The normalized field intensities are also plotted with distance from the surface of an isolated sphere. It is seen that the dimer yields normalized field intensities $\tilde{I}$ that are one or two orders of magnitude larger than that of an isolated sphere at the resonance frequencies $\omega = 3.48\,\text{eV}$ and $\omega = 3.21\,\text{eV}$, respectively. As discussed in the following section, the larger field enhancement is favorable for SERS.

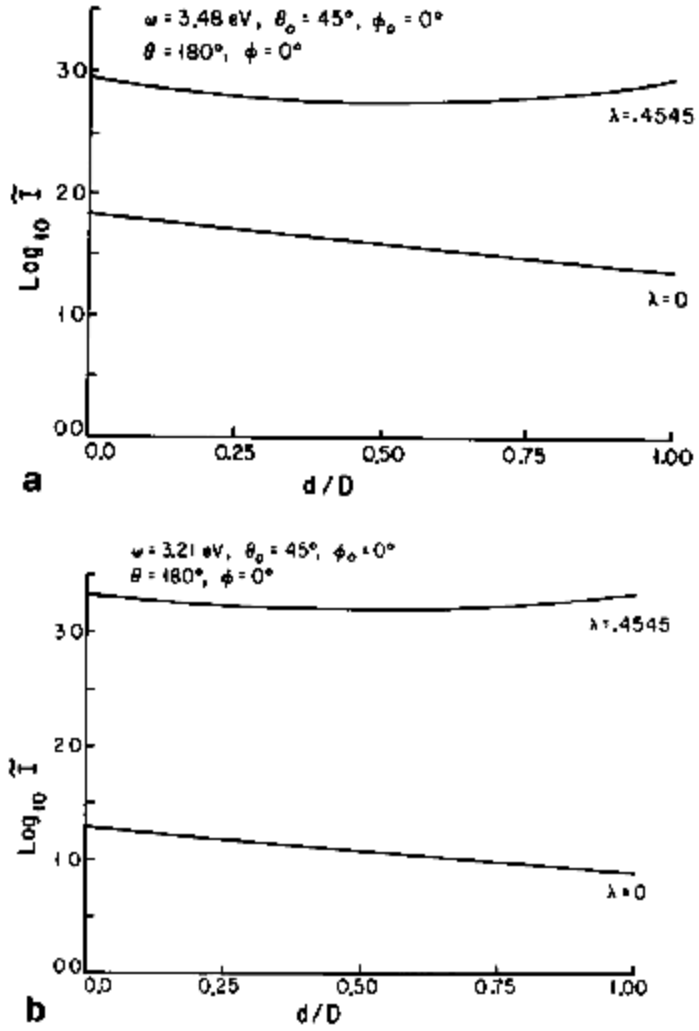

Figure 1-14. (a) Normalized field intensity along the z axis of the silver sphere dimer for $\lambda = 0.4545$ within the middle gap (upper curve) and along the z axis of isolated sphere (lower curve) at $\omega = 3.48$ eV. For the lower curve, the absicca should be $5d/R_0$, rather than d/D as shown. (b) Same as (a) but at $\omega = 3.21$ eV. (From Ref. [75]).

1.5 Raman Scattering and SERS

1.5.1 Raman Scattering

The scattering of photons by molecules is usually elastic, i.e. Rayleigh scattering [76], meaning that the scattered photons have the same energy as the incident photons. However, due to the vibrations of the molecules, a small fraction of the scattered photons can have different energy from the incident photons [77]. This phenomenon was first

theoretically predicted by Adolf Smekal in Ref. [78] and was experimentally observed by Chandrasekhara Venkata Rāman [79] and Leonid Mandelstam [80].

For a given molecule with N atoms, there are $3N$ degrees of freedom corresponding to the translations, rotations and vibrations of the molecule. The translational motion (i.e. moving in space) of a molecule has 3 degrees of freedom. There are 2 and 3 degrees of freedom for the rotation of a linear molecule and a non-linear molecule, respectively. There are therefore $3N-5$ and $3N-6$ remaining degrees of freedom for linear and non-linear molecules, respectively. These correspond to the vibrations (stretching and bending motions) of the molecule. The degrees of freedom of vibration allows a molecule to have a certain set of vibrational energies. The difference between the energies of the incident and scattered photons in Raman scattering corresponds to a vibrational energy of the molecule. Raman scattering spectra are therefore often thought of as "fingerprints" that allow molecules to be identified. It is for this reason that Raman spectroscopy is used for a variety of chemical detection applications, including food safety monitoring [81-83], explosive detection [84, 85], and pharmaceutical quality control [86, 87].

To facilitiate an intuitive understanding of Raman scattering, we now consider a classical model, as discussed in Ref [88]. We assume that the illuminating field is a plane wave, whose electric field is given by:

$$\overline{E}_{inc} = \overline{E}_0 e^{i\bar{k}\cdot\bar{r}} \quad (1.43)$$

Here, we employ phasor notation, i.e. the instantaneous electric field is given by:

$$\begin{aligned} \overline{E}_{inc}(t) &= \mathrm{Re}\{\overline{E}_0\, e^{i\bar{k}\cdot\bar{r}} e^{-i\omega_i t}\} \\ &= \overline{E}_0 \cos(\bar{k}\cdot\bar{r} - \omega_i t) \end{aligned} \quad (1.44)$$

Note that ω_i is the frequency of the incident wave. Since the molecule is much smaller than the incident wavelength, it is modeled as a dipole with dipole moment given by

$$\bar{p}(\bar{r}_0) = \bar{\bar{\alpha}} \cdot \bar{E}_{inc} = \bar{\bar{\alpha}} \cdot \bar{E}_0 \cos(\bar{k} \cdot \bar{r}_0 - \omega_i t) \quad (1.45)$$

where $\bar{\bar{\alpha}}$ is the polarizability of the molecule and $\bar{r}_0$ is the position of the molecule. Without loss of generality, $\bar{r}_0$ can be taken as the origin. The excitation of a molecular vibration modifies the polarizability. If the amplitude of the vibration is small, the polarizability $\bar{\bar{\alpha}}$ can be expanded around the equilibrium configuration of the molecule as follows:

$$\bar{\bar{\alpha}} = \bar{\bar{\alpha}}_0 + \frac{\partial \bar{\bar{\alpha}}}{\partial Q}|_e \, dQ + \cdots \quad (1.46a)$$

$$dQ = Q_0 \cos(\omega_v t) \quad (1.46b)$$

where Q denotes the normal mode coordinates and measures the amplitude of the movement of the atoms of the molecule as they oscillate in the vibrational mode under consideration. $\bar{\bar{\alpha}}_0$ is the polarizability of the molecule at the equilibrium position, $\frac{\partial \bar{\bar{\alpha}}}{\partial Q}|_e$ is the rate of change of the polarizability about the equilibrium positions of the atoms of the molecule, Q_0 is the maxium displacement from the equilibrium positions and ω_v is the vibration frequency of the molecule. By substituting Equation (1.46a) and (1.46b) into Equation (1.45), we obtain

$$\bar{p}(\bar{r}_0) = \bar{\bar{\alpha}}_0 \cdot \bar{E}_0 \cos(\omega_i t) + \frac{\partial \bar{\bar{\alpha}}}{\partial Q}|_e \, Q_0 \cos(\omega_v t) \cdot \bar{E}_0 \cos(\omega_i t) + \cdots \quad (1.47)$$

The first term of Equation (1.47) corresponds to Rayleigh scattering, with the frequency of the scattered field being the same as that of the incident wave. The second term

contains $\cos(\omega_v t)\cos(\omega_i t) = \frac{1}{2}\{\cos[(\omega_i + \omega_v)t] + \cos[(\omega_i - \omega_v)t]\}$. The $\cos[(\omega_i - \omega_v)t]$ and $\cos[(\omega_i + \omega_v)t]$ terms represent Stokes Raman scattering and anti-Stokes Raman scattering, respectively. From Equation (1.47), it can be seen that only those vibrations with $\frac{\partial \bar{\bar{\alpha}}}{\partial Q}|_e \neq 0$ participate in Raman scattering. The requirement that we have $\frac{\partial \bar{\bar{\alpha}}}{\partial Q}|_e \neq 0$ for Raman scattering as also called the Raman selection rule.

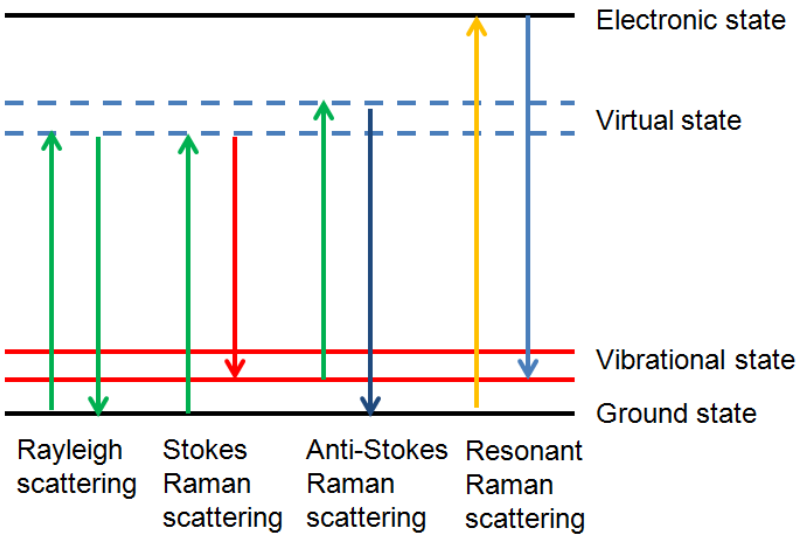

Figure 1-15. Energy diagram of Rayleigh scattering, Stokes Raman scattering, anti-Stokes Raman scattering and resonant Raman scattering.

The processes by which photons are scattered by molecules are depicted as an energy diagram in Figure 1-15. It can be seen that Rayleigh scattering involves the molecule being excited from the ground state to a virtual energy state by a photon, and then dropping back to the ground state. In Rayleigh scattering therefore, the scattered photon has same energy as the incident photon. In Stokes Raman scattering, the molecule is excited from the ground state to a virtual energy state and then drops to a vibrational state with an energy higher than the ground state. The energy of the scattered photon is therefore smaller than that of the incident photon. In anti-Stokes Raman scattering, a

molecule in a vibrational state is excited to a virtual state and then drops back to the ground state, meaning that the scattered photon has an energy that is greater than that of the incident photon. The Stokes Raman scattering produced by a given molecular vibration is stronger than anti-Stokes Raman scattering, unless techniques such as coherent anti-Stokes Raman scattering [89] are applied. This is due to the fact that the population of the molecules in the ground state is larger those in vibrational states. As shown in Figure 1-15, if the incident photon energy is close to the energy difference between the ground state and the one of the electronic states, the molecule is excited to an electronic state (electronic transition), rather than a virtual state, and drops to the ground state. The Raman scattering intensity associated with this transition is greatly increased due to the resonant excitation. This is termed resonant Raman scattering [90].

1.5.2 Surface enhanced Raman Scattering.

As discussed in the last section, Raman scattering is a powerful tool, enabling molcules to be identified by their vibrational spectra. The key challenge, however, is that Raman scattering is a weak effect, compared to other processes such as fluorescence. As an example, consider Rhodamine 6G, a popular dye employed in both fluorescence and SERS studies. The non-resonant Raman scattering cross section of a Rhodamine 6G molecule is $\sim 10^{-26}$ cm^2 [91, 92]. This is 10^{10} times smaller than its fluorescent cross section ($\sim 10^{-16}$ cm^2) [93]). To overcome this challenge, in this thesis, we focus on using surface enhanced Raman scattering (SERS) to boost Raman scattering.

SERS refers to the phenomenon whereby the Raman signals of molecules on the surfaces of metallic structures are dramatically enhanced. SERS was first experimentally

observed in 1974 when Martin Fleischman and coworkers studied the Raman scattering of pyridine adsorbed on rough silver surface [34]. The SERS effect can be sufficiently strong so that the SERS signals can be detected even from single molecules [37, 38]. SERS enhancement is attributed to two mechanisms: electromagnetic (EM) enhancement [35] and chemical enhancement [36] .

The EM enhancement mechanism has two parts: excitation enhancement and emission enhancement. The excitation enhancement is illustrated in Figure 1-16a. Suppose that a molecule with isotropic Raman polarizability α_R in free space is illuminated by the incident wave $\overline{E}_0(\omega_i)$. Raman scattering from the molecule can then be described by a dipole, whose dipole moment is given by

$$\overline{p}_{free} = \alpha_R \overline{E}_0(\omega_i) \quad (1.48)$$

When the molecule is in the vicinity of a nanostructure (Figure 1-16a) and the electric field $\overline{E}_t(\omega_i)$ experienced by the molecule is different from the incident field. It can be significantly larger if the nanostructure is on plasmon resonance. The Raman scattering from the molecule can again be modeled by a dipole. In this case, its dipole moment is given by:

$$\overline{p}_{SERS} = \alpha_R \overline{E}_t(\omega_i) \quad (1.49)$$

The excitation enhancement is then given by

$$EF_{excitation} = \left| \frac{\overline{p}_{SERS}}{\overline{p}_{free}} \right|^2 = \left| \frac{\overline{E}_t(\omega_i)}{\overline{E}_0(\omega_i)} \right|^2 \quad (1.50)$$

The second component to EM enhancement is that of emission enhancement (Figure 1-16b). Due to the existence of the nanostructure, spontaneous emission from the

molecule is modified and the radiated power of the molecule can be greatly enhanced [94]. One way of quantifying the effect would be place a dipole (modeling the molecule) in the vicinity of the nanostructure, then determine the radiated power analytically or numerically. It would be more convenient, however, to be able to quantify the effect via knowledge of the field enhancement resulting from plane wave illumination of the nanostructure. As noted in Ref. [95], the reciprocity theorem means that this is indeed possible. In Ref. [95], it is shown that the calculation of the emission enhancement of the Raman scattering from a molecule close to a nanostructure can be determined from the results of calculations of the local field enhancement for two incident plane waves with different polarizations. These plane waves are illustrated in Figure 1-16b. $\overline{E}_\theta(\omega_R)$ and $\overline{E}_\phi(\omega_R)$ denote the electric field vectors of the θ polarized and ϕ polarized plane waves, respectively. Both propagate along the $-\hat{r}$ direction, i.e. in the direction opposite to that for which the emission enhanced is being determined. As shown in Ref. [95], compared with the Raman scattering ($\overline{E}_{Raman}(\omega_R)$) generated by the dipole (modeling the molecule) in the absence of the nanostructure, the Raman scattering generated by a dipole with the same dipole moment close to the nanostructure is enhanced by

$$EF_{emission} = \left| \frac{\overline{E}_{SERS}(\omega_R)}{\overline{E}_{Raman}(\omega_R)} \right|^2 = \left| \frac{\hat{e}_d \cdot \overline{E}_\phi^{enhanced}(\omega_R)}{E_R(\omega_R)} \right|^2 + \left| \frac{\hat{e}_d \cdot \overline{E}_\theta^{enhanced}(\omega_R)}{E_R(\omega_R)} \right|^2 \quad (1.51)$$

Where $\overline{E}_{SERS}(\omega_R)$ is the enhanced Raman scattering field that occurs in the presence of the nanostructure. $\overline{E}_\phi^{enhanced}(\omega_R)$ and $\overline{E}_\theta^{enhanced}(\omega_R)$ are the local fields at the position of the molecule for the θ-polarized ($\overline{E}_\theta(\omega_R)$ electric field vector) and ϕ-polarized ($\overline{E}_\phi(\omega_R)$

electric field vector) incident waves, respectively. $\hat{e}_d$ is the direction of the dipole moment of the molecule.

Putting Equation (1.50) and (1.51) together, we obtain the following expression for the EM enhancement:

$$EF = EF_{excitation} \times EF_{emission} \quad (1.52)$$

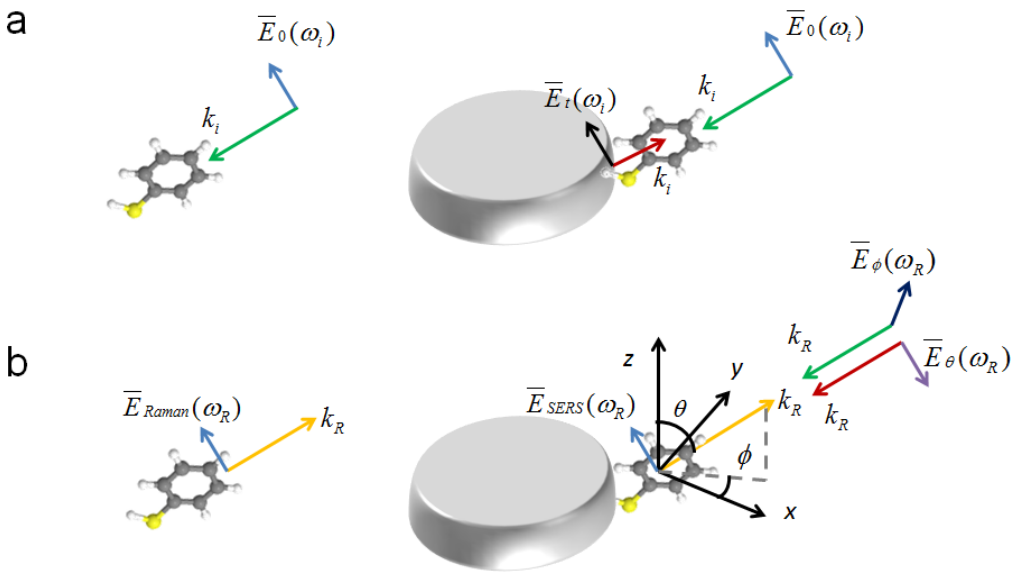

Figure 1-16. (a) Schematic of the excitation enhancement of the molecule in the vicinity of the nanostructure. ω_i is the frequency of the incident wave. k_i is wavevector of incident wave. (b) Schematic of emission enhancement of molecule in vicinity of nanostructure. ω_R is frequency of Raman scattered wave. k_R is wavevector of Raman scattered wave.

As discussed above, the SERS enhancement has two components: electromagnetic enhancement and chemical enhancement. Debate continues regarding the origin of chemical enhancement, but is often attributed to the formation of a complex between the molecule and the metal surface, and the charge transfer that can then occur. We discuss this mechanism below.

In Figure 1-17, the energy diagram of a hypothetical molecule-metal system is

illustrated. I and K are energy levels of the molecule, and there is an allowed transition between them. Without loss of generality, I and K can be regarded as the ground state and a vibronic excited state of the molecule, respectively. The left part of Figure 1-17a shows the energy levels of the conduction band (between ω_A and ω_B) and Fermi level (ω_F) of the metal. The conduction band of the metal is assumed to have a constant density of states ρ_0. For such a system, as shown in Ref. [96], two possible charge transfer mechanisms contribute to the chemical enhancement. The first one is shown in Figure 1-17b. A molecule-to-metal charge transfer occurs from the ground state of the molecule to one of the unfilled metal levels via the transition moment M_{IM}. The coupling matrix element h_{MK} allows the transfered charge to transfer from the metal state to the vibronic excited state K of the molecule. When the energy of the incident photons matches the energy difference between the ground state of the molecule and the unfilled metal level, the molecule-to-metal charge transfer is on resonance, and the SERS signal is therefore further enhanced. Figure 1-17c shows the second type of charge transfer, known as metal-to-molecule charge transfer. In this mechanism, charge is transfered from a filled metal level to the vibronic excited state of the molecule via the transition moment M_{MK}. The charge at the ground state of the molecule couples to the previously filled metal level through coupling matrix element h_{IM}. If the energy of the incident photons matches the energy difference between the filled metal level and the vibronic excited state of the molecule, the metal-to-molecule charge transfer is on resonance, and the SERS signal is therefore further enhanced.

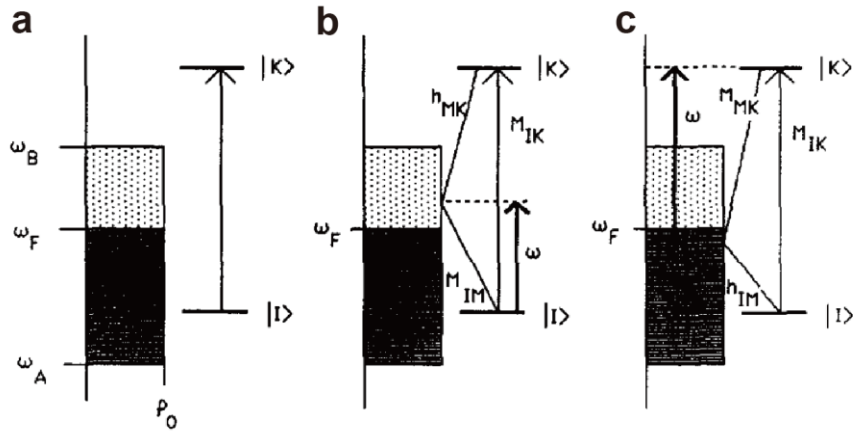

Figure 1-17. (a) Energy diagram for molecule-metal system. (b) Schematic illustration of molecule-to-metal charge transfer transitions between molecule's ground state and unfilled metal levels. (c) Schematic illustration of metal-to-molecule charge transfer transitions between filled metal levels and molecule's vibronic excited state. From Ref. [96].

The chemical enhancement mechanism is generally considered to be a small effect in comparison to EM enhancement. Chemical enhancements are generally reported to be smaller than $\sim 10^3$ [97]. It is for this reason that the remainder of this thesis concerns approaches by which EM enhancement can be strengthened.

1.6 References

[1]. S. A. Maier, *Plasmonics: Fundamentals and Applications* (Springer Science+Business Media, LLC, 2007).
[2]. H. A. Atwater, "The Promise of PLASMONICS," Scientific American **296**, 56-63 (2007).
[3]. A. Sommerfeld, "The propagation of light in dispersing media," Annalen der Physik **44**, 177-202 (1914).
[4]. G. Mie, "Beiträge zur Optik trüber Medien, speziell kolloidaler Metallösungen," Annalen der Physik **330**, 377-445 (1908).
[5]. R. H. Ritchie, "Plasma Losses by Fast Electrons in Thin Films," Physical Review **106**, 874-881 (1957).
[6]. K. A. Willets, and R. P. Van Duyne, "Localized Surface Plasmon Resonance Spectroscopy and Sensing," Annual Review of Physical Chemistry **58**, 267-297 (2007).
[7]. A. J. Haes, S. Zou, G. C. Schatz, and R. P. Van Duyne, "A Nanoscale Optical Biosensor: The Long Range Distance Dependence of the Localized Surface Plasmon Resonance of Noble Metal Nanoparticles," The Journal of Physical Chemistry B **108**, 109-116 (2003).

[8]. P. K. Jain, X. Huang, I. H. El-Sayed, and M. A. El-Sayed, "Noble metals on the nanoscale: optical and photothermal properties and some applications in imaging, sensing, biology, and medicine," Accounts of chemical research **41**, 1578-1586 (2008).
[9]. A. G. Brolo, "Plasmonics for future biosensors," Nat Photon **6**, 709-713 (2012).
[10]. S. A. Maier, P. G. Kik, H. A. Atwater, S. Meltzer, E. Harel, B. E. Koel, and A. A. G. Requicha, "Local detection of electromagnetic energy transport below the diffraction limit in metal nanoparticle plasmon waveguides," Nat Mater **2**, 229-232 (2003).
[11]. T. Onuki, Y. Watanabe, K. Nishio, T. Tsuchiya, T. Tani, and T. Tokizaki, "Propagation of surface plasmon polariton in nanometre-sized metal-clad optical waveguides," Journal of microscopy **210**, 284-287 (2003).
[12]. E. Verhagen, A. Polman, and L. Kuipers, "Nanofocusing in laterally tapered plasmonic waveguides," Opt. Express **16**, 45-57 (2008).
[13]. R. F. Oulton, V. J. Sorger, D. A. Genov, D. F. P. Pile, and X. Zhang, "A hybrid plasmonic waveguide for subwavelength confinement and long-range propagation," Nat Photon **2**, 496-500 (2008).
[14]. D. K. Gramotnev, and S. I. Bozhevolnyi, "Plasmonics beyond the diffraction limit," Nat Photon **4**, 83-91 (2010).
[15]. R. A. Shelby, D. R. Smith, and S. Schultz, "Experimental Verification of a Negative Index of Refraction," Science **292**, 77-79 (2001).
[16]. H. J. Lezec, J. A. Dionne, and H. A. Atwater, "Negative Refraction at Visible Frequencies," Science **316**, 430-432 (2007).
[17]. V. M. Shalaev, "Optical negative-index metamaterials," Nat Photon **1**, 41-48 (2007).
[18]. J. Valentine, S. Zhang, T. Zentgraf, E. Ulin-Avila, D. A. Genov, G. Bartal, and X. Zhang, "Three-dimensional optical metamaterial with a negative refractive index," Nature **455**, 376-379 (2008).
[19]. S. Pillai, K. R. Catchpole, T. Trupke, and M. A. Green, "Surface plasmon enhanced silicon solar cells," Journal of Applied Physics **101**, 093105-093108 (2007).
[20]. A. J. Morfa, K. L. Rowlen, T. H. Reilly, Iii, M. J. Romero, and J. van de Lagemaat, "Plasmon-enhanced solar energy conversion in organic bulk heterojunction photovoltaics," Applied Physics Letters **92**, 013504-013503 (2008).
[21]. Y. A. Akimov, W. S. Koh, and K. Ostrikov, "Enhancement of optical absorption in thin-film solar cells through the excitation of higher-order nanoparticle plasmon modes," Opt. Express **17**, 10195-10205 (2009).
[22]. H. A. Atwater, and A. Polman, "Plasmonics for improved photovoltaic devices," Nat Mater **9**, 205-213 (2010).
[23]. A. Hartschuh, E. J. Sánchez, X. S. Xie, and L. Novotny, "High-Resolution Near-Field Raman Microscopy of Single-Walled Carbon Nanotubes," Physical Review Letters **90**, 095503 (2003).
[24]. T. Ichimura, N. Hayazawa, M. Hashimoto, Y. Inouye, and S. Kawata, "Tip-Enhanced Coherent Anti-Stokes Raman Scattering for Vibrational Nanoimaging," Physical Review Letters **92**, 220801 (2004).
[25]. J. M. Gerton, L. A. Wade, G. A. Lessard, Z. Ma, and S. R. Quake, "Tip-Enhanced Fluorescence Microscopy at 10 Nanometer Resolution," Physical Review Letters **93**, 180801 (2004).
[26]. F. M. Huang, F. Festy, and D. Richards, "Tip-enhanced fluorescence imaging of

quantum dots," Applied Physics Letters **87**, 183101-183103 (2005).
[27]. S. Kawata, Y. Inouye, and P. Verma, "Plasmonics for near-field nano-imaging and superlensing," Nat Photon **3**, 388-394 (2009).
[28]. J. Hashizume, and F. Koyama, "Plasmon-enhancement of optical near-field of metal nanoaperture surface-emitting laser," Applied Physics Letters **84**, 3226-3228 (2004).
[29]. Z. Rao, J. A. Matteo, L. Hesselink, and J. S. Harris, "High-intensity C-shaped nanoaperture vertical-cavity surface-emitting laser with controlled polarization," Applied Physics Letters **90**, 191110-191113 (2007).
[30]. P. Zijlstra, J. W. M. Chon, and M. Gu, "Five-dimensional optical recording mediated by surface plasmons in gold nanorods," Nature **459**, 410-413 (2009).
[31]. I. Romero, J. Aizpurua, G. W. Bryant, and F. J. García De Abajo, "Plasmons in nearly touching metallic nanoparticles: singular response in the limit of touching dimers," Opt. Express **14**, 9988-9999 (2006).
[32]. R. Esteban, A. G. Borisov, P. Nordlander, and J. Aizpurua, "Bridging quantum and classical plasmonics with a quantum-corrected model," Nat Commun **3**, 825 (2012).
[33]. K. J. Savage, M. M. Hawkeye, R. Esteban, A. G. Borisov, J. Aizpurua, and J. J. Baumberg, "Revealing the quantum regime in tunnelling plasmonics," Nature **491**, 574-577 (2012).
[34]. M. Fleischmann, P. J. Hendra, and A. J. McQuillan, "Raman spectra of pyridine adsorbed at a silver electrode," Chemical Physics Letters **26**, 163-166 (1974).
[35]. D. L. Jeanmaire, and R. P. Van Duyne, "Surface raman spectroelectrochemistry: Part I. Heterocyclic, aromatic, and aliphatic amines adsorbed on the anodized silver electrode," Journal of Electroanalytical Chemistry and Interfacial Electrochemistry **84**, 1-20 (1977).
[36]. M. G. Albrecht, and J. A. Creighton, "Anomalously intense Raman spectra of pyridine at a silver electrode," Journal of the American Chemical Society **99**, 5215-5217 (1977).
[37]. S. Nie, and S. R. Emory, "Probing Single Molecules and Single Nanoparticles by Surface-Enhanced Raman Scattering," Science **275**, 1102-1106 (1997).
[38]. K. Kneipp, Y. Wang, H. Kneipp, L. T. Perelman, I. Itzkan, R. R. Dasari, and M. S. Feld, "Single Molecule Detection Using Surface-Enhanced Raman Scattering (SERS)," Physical Review Letters **78**, 1667-1670 (1997).
[39]. K. Kneipp, M. Moskovits, and H. Kneipp, *Surface-enhanced Raman Scattering: Physics and Applications* (Springer-Verlag Berlin Heidelberg, 2006).
[40]. J. P. Schmidt, S. E. Cross, and S. K. Buratto, "Surface-enhanced Raman scattering from ordered Ag nanocluster arrays," The Journal of Chemical Physics **121**, 10657-10659 (2004).
[41]. N. Felidj, S. L. Truong, J. Aubard, G. Levi, J. R. Krenn, A. Hohenau, A. Leitner, and F. R. Aussenegg, "Gold particle interaction in regular arrays probed by surface enhanced Raman scattering," The Journal of Chemical Physics **120**, 7141-7146 (2004).
[42]. A. D. McFarland, M. A. Young, J. A. Dieringer, and R. P. Van Duyne, "Wavelength-Scanned Surface-Enhanced Raman Excitation Spectroscopy," The Journal of Physical Chemistry B **109**, 11279-11285 (2005).
[43]. S. J. Oldenburg, S. L. Westcott, R. D. Averitt, and N. J. Halas, "Surface enhanced Raman scattering in the near infrared using metal nanoshell substrates," The Journal of

Chemical Physics **111**, 4729-4735 (1999).
[44]. J. Grand, M. L. de la Chapelle, J. L. Bijeon, P. M. Adam, A. Vial, and P. Royer, "Role of localized surface plasmons in surface-enhanced Raman scattering of shape-controlled metallic particles in regular arrays," Physical Review B **72**, 033407 (2005).
[45]. J. Aizpurua, P. Hanarp, D. S. Sutherland, M. Käll, G. W. Bryant, and F. J. García de Abajo, "Optical Properties of Gold Nanorings," Physical Review Letters **90**, 057401 (2003).
[46]. M. G. Banaee, and K. B. Crozier, "Gold nanorings as substrates for surface-enhanced Raman scattering," Opt. Lett. **35**, 760-762 (2010).
[47]. Y. Chu, M. G. Banaee, and K. B. Crozier, "Double-Resonance Plasmon Substrates for Surface-Enhanced Raman Scattering with Enhancement at Excitation and Stokes Frequencies," ACS Nano **4**, 2804-2810 (2010).
[48]. H. R. Stuart, and D. G. Hall, "Enhanced Dipole-Dipole Interaction between Elementary Radiators Near a Surface," Physical Review Letters **80**, 5663-5666 (1998).
[49]. S. Zou, and G. C. Schatz, "Silver nanoparticle array structures that produce giant enhancements in electromagnetic fields," Chemical Physics Letters **403**, 62-67 (2005).
[50]. N. Papanikolaou, "Optical properties of metallic nanoparticle arrays on a thin metallic film," Physical Review B **75**, 235426 (2007).
[51]. M. K. Kinnan, and G. Chumanov, "Surface Enhanced Raman Scattering from Silver Nanoparticle Arrays on Silver Mirror Films: Plasmon-Induced Electronic Coupling as the Enhancement Mechanism," The Journal of Physical Chemistry C **111**, 18010-18017 (2007).
[52]. G. Gantzounis, N. Stefanou, and N. Papanikolaou, "Optical properties of periodic structures of metallic nanodisks," Physical Review B **77**, 035101 (2008).
[53]. T. J. Seok, A. Jamshidi, M. Kim, S. Dhuey, A. Lakhani, H. Choo, P. J. Schuck, S. Cabrini, A. M. Schwartzberg, J. Bokor, E. Yablonovitch, and M. C. Wu, "Radiation Engineering of Optical Antennas for Maximum Field Enhancement," Nano Letters **11**, 2606-2610 (2011).
[54]. P. Drude, "Zur Elektronentheorie der Metalle," Annalen der Physik **306**, 566-613 (1900).
[55]. P. Drude, "Zur Elektronentheorie der Metalle; II. Teil. Galvanomagnetische und thermomagnetische Effecte," Annalen der Physik **308**, 369-402 (1900).
[56]. N. W. Ashcroft, and N. D. Mermin, *Solid state physics* (Saunders College, 1976).
[57]. P. B. Johnson, and R. W. Christy, "Optical Constants of the Noble Metals," Physical Review B **6**, 4370-4379 (1972).
[58]. H. A. Lorentz, *The Theory of Electrons and Its Applications to the Phenomena of Light and Radiant Heat* (Cosimo, Incorporated, 2007).
[59]. R. D. L. Kronig, "ON THE THEORY OF DISPERSION OF X-RAYS," J. Opt. Soc. Am. **12**, 547-556 (1926).
[60]. L. Novotny, and B. Hecht, *Principles of Nano-Optics* (Cambridge University Press, 2006).
[61]. W. L. Barnes, A. Dereux, and T. W. Ebbesen, "Surface plasmon subwavelength optics," Nature **424**, 824-830 (2003).
[62]. E. Ozbay, "Plasmonics: Merging Photonics and Electronics at Nanoscale Dimensions," Science **311**, 189-193 (2006).
[63]. O. Benson, "Assembly of hybrid photonic architectures from nanophotonic

constituents," Nature **480**, 193-199 (2011).
[64]. C. F. Bohren, and D. R. Huffman, *Absorption and Scattering of Light by Small Particles* (Wiley, 2008).
[65]. J. A. Kong, *Electromagnetic Wave Theory* (EMW, Cambridge, 2005).
[66]. J. R. Krenn, A. Dereux, J. C. Weeber, E. Bourillot, Y. Lacroute, J. P. Goudonnet, G. Schider, W. Gotschy, A. Leitner, F. R. Aussenegg, and C. Girard, "Squeezing the Optical Near-Field Zone by Plasmon Coupling of Metallic Nanoparticles," Physical Review Letters **82**, 2590-2593 (1999).
[67]. W. Rechberger, A. Hohenau, A. Leitner, J. R. Krenn, B. Lamprecht, and F. R. Aussenegg, "Optical properties of two interacting gold nanoparticles," Optics Communications **220**, 137-141 (2003).
[68]. T. Atay, J.-H. Song, and A. V. Nurmikko, "Strongly Interacting Plasmon Nanoparticle Pairs: From Dipole−Dipole Interaction to Conductively Coupled Regime," Nano Letters **4**, 1627-1631 (2004).
[69]. P. K. Jain, S. Eustis, and M. A. El-Sayed, "Plasmon Coupling in Nanorod Assemblies: Optical Absorption, Discrete Dipole Approximation Simulation, and Exciton-Coupling Model," The Journal of Physical Chemistry B **110**, 18243-18253 (2006).
[70]. J. D. Jackson, *Classical Electrodynamics* (Wiley, 1998).
[71]. M. L. Brongersma, J. W. Hartman, and H. A. Atwater, "Electromagnetic energy transfer and switching in nanoparticle chain arrays below the diffraction limit," Physical Review B **62**, R16356-R16359 (2000).
[72]. A. F. Koenderink, and A. Polman, "Complex response and polariton-like dispersion splitting in periodic metal nanoparticle chains," Physical Review B **74**, 033402 (2006).
[73]. S. Karumuri, *Hybrid Surface Plasmon Damping Chemical Sensor* (Oklahoma State University, 2008).
[74]. C. E. Talley, J. B. Jackson, C. Oubre, N. K. Grady, C. W. Hollars, S. M. Lane, T. R. Huser, P. Nordlander, and N. J. Halas, "Surface-Enhanced Raman Scattering from Individual Au Nanoparticles and Nanoparticle Dimer Substrates," Nano Letters **5**, 1569-1574 (2005).
[75]. P. K. Aravind, A. Nitzan, and H. Metiu, "The interaction between electromagnetic resonances and its role in spectroscopic studies of molecules adsorbed on colloidal particles or metal spheres," Surface Science **110**, 189-204 (1981).
[76]. J. W. Strutt, "LVIII. On the scattering of light by small particles," Philosophical Magazine Series 4 **41**, 447-454 (1871).
[77]. D. C. Harris, and M. D. Bertolucci, *Symmetry and Spectroscopy: An Introduction to Vibrational and Electronic Spectrosocpy* (DOVER PUBN Incorporated, 1978).
[78]. A. Smekal, "Zur Quantentheorie der Dispersion," Naturwissenschaften **11**, 873-875 (1923).
[79]. C. Raman, "A new radiation," Indian Journal of physics **2**, 387-398 (1928).
[80]. G. Landsberg, and L. I. Mandelstam, "Eine neue Erscheinung bei der Lichtzerstreuung in Krystallen," Naturwissenschaften **16**, 557-558 (1928).
[81]. Y. Liu, K. Chao, M. S. Kim, D. Tuschel, O. Olkhovyk, and R. J. Priore, "Potential of Raman Spectroscopy and Imaging Methods for Rapid and Routine Screening of the Presence of Melamine in Animal Feed and Foods," Appl. Spectrosc. **63**, 477-480 (2009).

[82]. L. He, *Application of Surface Enhanced Raman Spectroscopy to Food Safety Issues* (BiblioBazaar, 2012).
[83]. J. Qin, K. Chao, and M. Kim, "Raman chemical imaging system for food safety and quality inspection," Transactions of the ASABE **53**, 1873-1882 (2010).
[84]. C. Cheng Cheng Cheng, Z. Li Zhenyu Li, W. Liu Weihao Liu, and J. Wu Jing Wu, "Stand-Off Explosives Detection Based on Raman Spectroscopy," CORD Conference Proceedings, 1-4 (2010).
[85]. E. L. Izake, "Forensic and homeland security applications of modern portable Raman spectroscopy," Forensic science international **202**, 1-8 (2010).
[86]. T. Vankeirsbilck, A. Vercauteren, W. Baeyens, G. Van der Weken, F. Verpoort, G. Vergote, and J. P. Remon, "Applications of Raman spectroscopy in pharmaceutical analysis," TrAC Trends in Analytical Chemistry **21**, 869-877 (2002).
[87]. S. Wartewig, and R. H. Neubert, "Pharmaceutical applications of Mid-IR and Raman spectroscopy," Advanced drug delivery reviews **57**, 1144-1170 (2005).
[88]. J. R. Ferraro, K. Nakamoto, and C. W. Brown, *Introductory Raman spectroscopy [electronic resource]* (Academic Press, 2003).
[89]. J.-X. Cheng, and X. S. Xie, "Coherent anti-Stokes Raman scattering microscopy: instrumentation, theory, and applications," The Journal of Physical Chemistry B **108**, 827-840 (2004).
[90]. R. S. Chao, R. K. Khanna, and E. R. Lippincott, "Theoretical and experimental resonance Raman intensities for the manganate ion," Journal of Raman Spectroscopy **3**, 121-131 (1975).
[91]. J. A. Dieringer, K. L. Wustholz, D. J. Masiello, J. P. Camden, S. L. Kleinman, G. C. Schatz, and R. P. Van Duyne, "Surface-Enhanced Raman Excitation Spectroscopy of a Single Rhodamine 6G Molecule," Journal of the American Chemical Society **131**, 849-854 (2008).
[92]. E. C. Le Ru, E. Blackie, M. Meyer, and P. G. Etchegoin, "Surface Enhanced Raman Scattering Enhancement Factors: A Comprehensive Study," The Journal of Physical Chemistry C **111**, 13794-13803 (2007).
[93]. T. Grossmann, S. Schleede, M. Hauser, M. B. Christiansen, C. Vannahme, C. Eschenbaum, S. Klinkhammer, T. Beck, J. Fuchs, G. U. Nienhaus, U. Lemmer, A. Kristensen, T. Mappes, and H. Kalt, "Low-threshold conical microcavity dye lasers," Applied Physics Letters **97**, 063304 (2010).
[94]. L. A. Blanco, and F. J. García de Abajo, "Spontaneous light emission in complex nanostructures," Physical Review B **69**, 205414 (2004).
[95]. E. C. Le Ru, and P. G. Etchegoin, "Rigorous justification of the |E|4 enhancement factor in Surface Enhanced Raman Spectroscopy," Chemical Physics Letters **423**, 63-66 (2006).
[96]. J. R. Lombardi, R. L. Birke, T. Lu, and J. Xu, "Charge-transfer theory of surface enhanced Raman spectroscopy: Herzberg--Teller contributions," The Journal of Chemical Physics **84**, 4174-4180 (1986).
[97]. Zhao, L. Jensen, and G. C. Schatz, "Pyridine−Ag20 Cluster: A Model System for Studying Surface-Enhanced Raman Scattering," Journal of the American Chemical Society **128**, 2911-2919 (2006).

2 Charge and current reservoirs for electric and magnetic field enhancement

2.1 Introduction

The extension of antenna concepts from radio frequencies to the visible and infrared portions of the electromagnetic spectrum has been recently explored. Using optical antennas with different designs, localized field enhancement can be conveniently realized over a range of wavelengths [1-9]. As described in the remainder of this thesis, the optical antenna concept is useful for applications such as surface enhanced Raman spectroscopy (SERS) [10] and optical metamaterials [11-15].

Traditionally, research has focused on electric-type optical antennas, among which, the rod antenna [2, 3] and the bowtie antenna [4] have been widely investigated, because of favorable properties that include large field enhancement and subwavelength field confinement. As shown in [4], the rod antenna has a higher field enhancement factor in its center gap than the bowtie shaped antenna does, but the contrast between the enhanced fields in the center gap and the outer edge of the rod antenna is smaller than that of the bowtie antenna. In this Chapter, a fan-rod antenna design with charge reservoirs is proposed to realize high field enhancement in its gap and low enhancement at its outer edge simultaneously. This work provides insight into the field enhancement mechanisms of different electric-type antenna structures and outlines methods to achieve high localized field enhancement. In addition to the fan-rod electric antenna design, a loop shaped magnetic-type optical antenna design with current reservoirs for realizing large

magnetic field enhancement is also proposed in this chapter. Compared with the magnetic resonant structures proposed in Ref. [13] and [14], the loop shaped magnetic antenna with current reservoirs has higher magnetic field enhancement. The flared part of the electric antenna and the offset part of the magnetic antenna supply additional charges and currents for electric and magnetic resonances, respectively, and are therefore termed "reservoirs". The concepts of charge and current reservoirs contribute to high electric and magnetic field enhancement in both optical antenna designs.

2.2 Electric antenna with charge reservoirs

In [4], it was pointed out that the bowtie antenna has lower field enhancement than the rod antenna. The advantage of the rod antenna is its good confinement of charges at its apex, but the rod structure does not have the flared sections of the bowtie structure that work as charge reservoirs and are capable of supplying large amounts of charge. Our fan-rod electric antenna structure is shown in Figure 2-1a, and combines the advantages of both to achieve the highest enhancement among the three structures. Simulation results in the next section prove that this is the case.

The fan-rod antenna design can be divided into two parts: the rod part (gray section in Figure 2-1a) and the flared sections (charge reservoirs). These help confine fields in the gap and reduce the accumulated charge densities at the outer edges, respectively. The fan-rod antenna design has strong electric response when it is illuminated by the incident wave with electric field polarized in the x direction and magnetic field polarized in the y direction. For comparison, simulations of a rod antenna and a bowtie antenna (as shown in Figure 2-1b and Figure 2-1c, respectively) are also conducted, and are described in the

later part of this section.

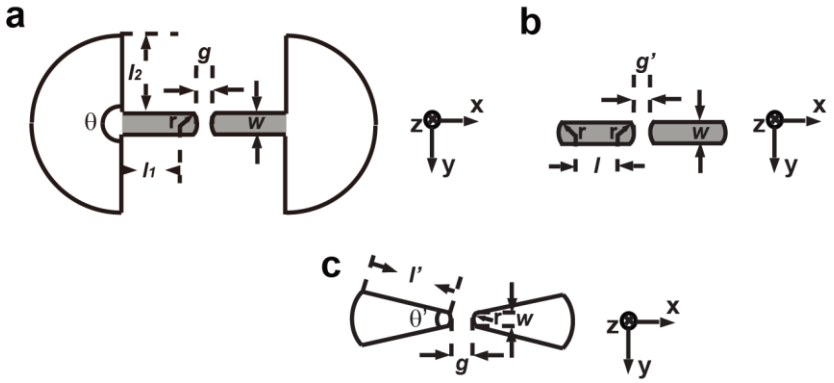

Figure 2-1. (a) Fan-rod electric antenna design. (b) Rod antenna. (c) Bowtie antenna. For all of these antennas, the thickness in the *z* direction is 40 nm.

In all simulations related to electric antennas, gold is used as the antenna material. We fit a Drude model (plasma frequency is 1.146×10^{16} rad/s and collision frequency is 1.569×10^{14} rad/s) to the optical properties of gold taken from Ref. [16]. The antennas are situated in free space. The incident wave consists of a plane wave with electric field polarized in the *x* direction and magnetic field polarized in the *y* direction. The incident wave is chosen to excite the resonances of the antennas.

In experiments, electric optical antennas are often fabricated by e-beam lithography. In our experience, gaps of ~20 nm can be readily achieved, while gaps below 10 nm are challenging unless special techniques, such as those described in Chapters 4 and 5, are employed. We therefore choose an antenna gap *g* of 20 nm in our simulations. According to simulation results (not shown here), higher field enhancement in the center gap is achieved for rod antenna designs with thinner widths *w*. We believe this is due to higher charge density at the apexes. Because of the larger enhancement, the width *w* of the fan-rod antenna (Fig. 1(a)) is set to be 20 nm. Note that *r* and antenna gap are fixed, and only the lengths (l_1, l_2, l and l') are adjusted to make the fan-rod antenna, rod antenna and bowtie antenna all resonant at a wavelength of λ=1 μm. In simulations (not shown here),

we find that the field enhancement of fan-rod antenna increases when θ increases and other parameters are fixed. This is expected because larger θ indicates larger flared sections, resulting in more charges being supplied to the rod part, thereby increasing the field enhancement. We therefore choose $\theta=\pi$ to maximize the field enhancement. On the other hand, the field enhancement of the bowtie antenna decreases when θ' increases and other parameters are fixed. This is also expected because larger θ' indicates larger antenna area and higher loss as pointed out in Ref [4]. We therefore simulate bowtie antennas with $\theta'=\pi/6$, thereby achieving high field enhancement while retaining the bowtie shape.

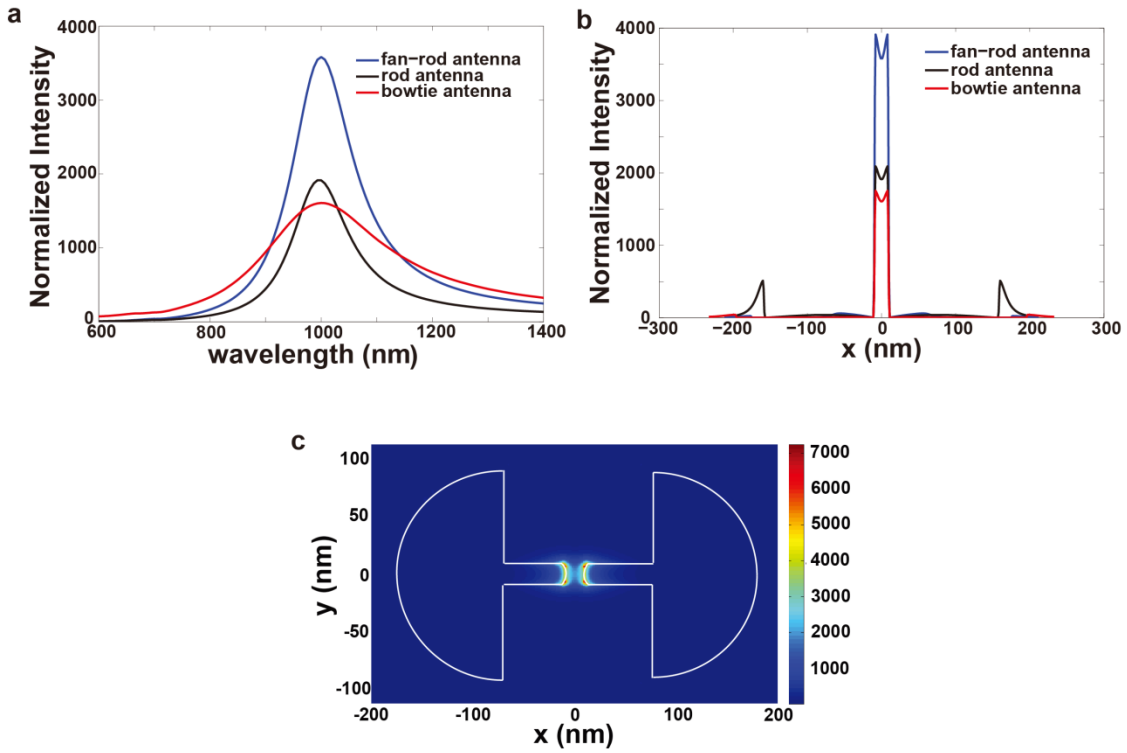

Figure 2-2. (a) Normalized electric field intensity (E^2) for fan-rod antenna, rod antenna and bowtie antenna. (b) Normalized electric field intensity (E^2) profiles along antenna axes for fan-rod, rod and bowtie antennas at a wavelength of λ=1 μm. (c) Normalized electric field intensity (E^2) distribution on a plane 2 nm above the top surface of the fan-rod antenna. White curves show the fan-rod antenna outline.

The electric field intensity at the gap center is given in Figure 2-2a, for the fan-rod

antenna (r=30 nm, l_1=25 nm, l_2=80 nm, θ=π, w=20 nm and g= 20nm), rod antenna (r=30 nm, l=88 nm, w= 20 nm and g' =20 nm), and bowtie antenna (r=30 nm, l'=183 nm, θ'=π/6, w=20 nm and g= 20nm). Here, we define the "center" of the antenna to be situated at the midpoint of the antenna gap, and 20 nm above the bottom of the antenna in the -z direction. The intensity plotted is normalized to the electric field intensity of the incident wave. The geometric parameters of the three different types of antennas are chosen so that all of them are resonant at a wavelength of λ=1 μm.

As shown in Figure 2-2, the bowtie antenna has smaller field enhancement than the rod antenna, which is in agreement with Ref. [4]. The fan-rod design has the largest field enhancement. This arises because it combines rod sections, which can confine the accumulation of charges to their apexes, with flared sections (charge reservoirs), which can supply additional charges to the apexes of the rod sections. The flared sections of fan-rod antenna are similar to the bulk metal part of the H-shaped aperture of Ref. [9]. The bulk metal part of H-shaped aperture can also supply additional charges to the strip parts of the aperture, thereby achieving field enhancement. In Figure 2-2b, the field intensities along the axes of three types of antennas are shown. We define the antenna axis as being the x axis, with the center of the antenna gap being the origin (Figure 2-1). The axes of the antennas are 20 nm above the bottom of the antennas in the -z direction. It can be seen that field enhancement at the outer edges of the fan-rod design is much smaller than that of the rod antenna, which is reasonable because the flared sections reduce the charge densities at the outer edges, which naturally leads to smaller field intensity. In Fig. 3 (c), the intensity distribution is shown on a plane 2 nm above the top surface of the fan-rod antenna. We find that the electric field is strongly enhanced over the antenna gap and the

ratio of field intensity in the center to that at the outer edges is high. The simulation results of Figure 2-2 verify that the fan-rod antenna design can simultaneously realize large field enhancement and high ratio of field intensity in the center to that at the outer edges. The large field enhancement induced by the charge reservoirs (the flared sections) suggests that fan-rod antennas could be useful for SERS.

2.3 Magnetic antenna with current reservoirs

As a dual counterpart of the electric antenna, a small current loop with subwavelength size can be regarded as a magnetic dipole antenna. Such antennas are often used at microwave frequencies. Here, this concept is used at optical frequencies. The unit cell of our magnetic antenna design is illustrated in Figure 2-3a.

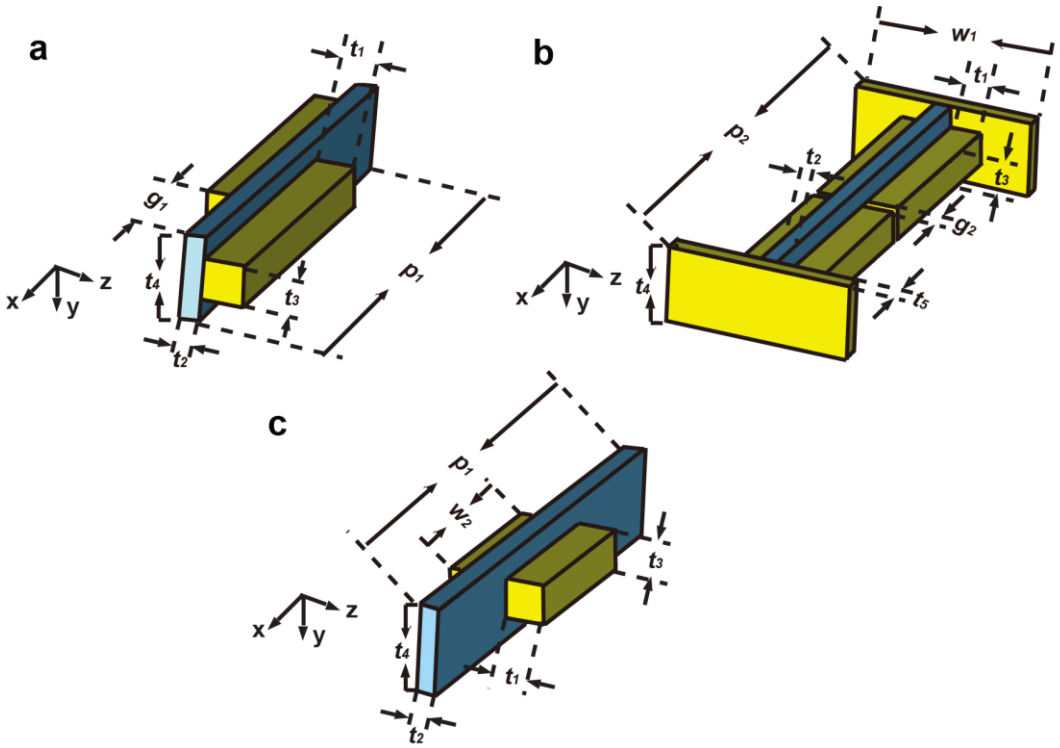

Figure 2-3. (a) Unit cell of loop shaped magnetic antenna with offsets. (b) Unit cell of loop shaped magnetic antenna with slits. (c) Unit cell of loop shaped magnetic antenna without offsets. Blue parts represent free space, and are shown to aid visualization of the structures.

For the unit cell of magnetic antenna, two metallic strips (the yellow parts of Figure 2-3a) are separated by a gap in the z direction, and offset from one another in the x direction. The metallic strips form an effective current loop enabling a magnetic resonance to be achieved. This permits the design to function as a magnetic antenna at optical frequencies. Our magnetic antenna design has strong magnetic response when it is illuminated by an incident wave with electric field polarized in the x direction and magnetic field polarized in the y direction. The offset parts of the metallic strips work as current reservoirs that supply additional currents to the loop part of the magnetic antenna when the whole structure is resonant. This property helps realize confined high magnetic field enhancement in the center of the magnetic antenna. For comparison, we also simulated the loop shaped structure with slits proposed in Ref. [13] and the loop shaped structure without offsets proposed in Ref. [14] in section 4. The geometries of the unit cells of the structures proposed in Ref. [13] and [14] are shown in Figure 2-3b and Figure 2-3c, respectively. In the simulations, the structures of Figure 2-3 are repeated along the x direction with periodicity p_1 or p_2 and along the y direction with periodicity t_4, respectively.

As shown in Ref. [17-19], magnetic resonators such as split ring resonators (SRR), double side omega-shaped resonators and coplanar S-shaped resonators can be realized in the microwave frequency band where metals such as gold or copper can be regarded as perfect electric conductors (PEC). They therefore can provide surface currents to form resonant current loops. Such magnetic resonators usually have highly dispersive magnetic properties which make them useful for realizing metamaterials. In Ref. [20], the authors used high permittivity nonconductive BST material to build magnetic resonators based on

displacement currents at microwave frequencies. Our magnetic antenna design combines both conduction and displacement currents to form a resonant current loop. The conduction currents along the metallic strips and the displacement currents between the gaps form a current loop, as shown in Figure 2-4a. The gaps between the metallic strips introduce capacitance and the current loop introduces inductance. The unit cell of magnetic antenna can therefore be modeled by the equivalent circuit shown in Figure 2-4b. Such a design makes it feasible to tune the magnetic resonance by changing the size of the current loop and the distance between metallic strips.

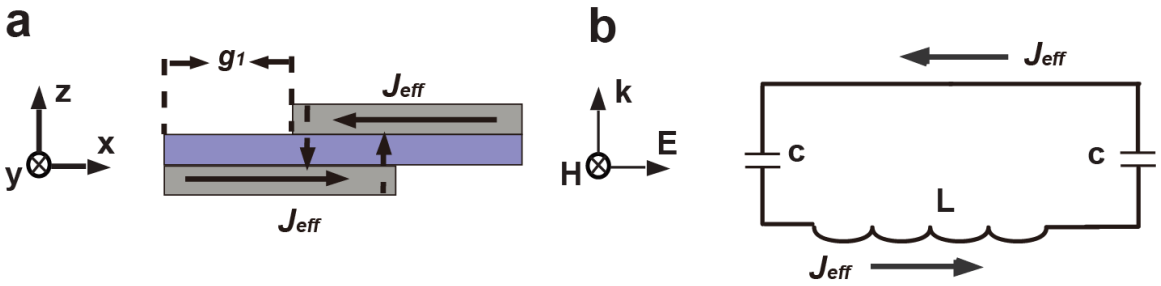

Figure 2-4. (a) Current loop for the unit cell of loop shaped antenna with offsets. (b) Equivalent circuit.

For the simulations related to magnetic antennas, gold is chosen as the antenna material with the same optical properties as those of last section. The antennas are situated in free space. The unit cells of magnetic antennas are repeated along the *x* and y directions. This is realized in the simulations using periodic boundaries at the *x* and y direction boundaries. The incident wave is a plane wave with its electric field polarized in the *x* direction and its magnetic field polarized in the *y* direction. The incident wave is chosen to induce current in the loops of the magnetic antennas.

In simulations (not shown here), we find that magnetic field enhancement increases as t_2 decreases. We believe this is due to the magnetic field generated by conduction currents and displacement currents being stronger closer to the metallic strips. For high

magnetic field enhancement, therefore, t_2 is chosen to be 20 nm for all magnetic antennas considered. To enable comparison between designs, the y direction periodicity is chosen to be the same for all magnetic antennas. In order to make all the antennas resonant at the same wavelength, we adjust the value of g_1, p_2 and w_2 for loop shaped antenna with offsets, loop shaped antenna with slits and loop shaped antenna without offsets, respectively. As shown in Fig. 4, both the size of the current loop and the inductance in the equivalent circuit decrease when g_1 increases. By changing g_1, the magnetic resonance of loop shaped antenna with offsets is tuned. As shown in Ref. [13] and [14], the structures of Figure 2-3b and Figure 2-3c form current loops. Similar to a loop shaped antenna with offsets, the equivalent inductance of a loop shaped antenna with slits and a loop shaped antenna without offsets increase as p_2 and w_2 increase. Therefore, the magnetic resonances of the loop shaped antenna with slits and the loop shaped antenna are tuned by changing p_2 and w_2, respectively. The geometric parameters of the three different types of magnetic antennas are chosen so that all of them are resonant at a wavelength of λ=1 μm.

The magnetic field intensities at the center point of the unit cells of magnetic antennas are given in Figure 2-5a, for the loop shaped antenna with offsets (p_1=500 nm, g_1= 142 nm, t_1= 40 nm, t_2= 20 nm and t_4=90 nm), loop shaped antenna with slits (p_2=552 nm, g_2= 10 nm, t_1= 40 nm, t_2= 20 nm, t_3= 20 nm, t_4=90 nm and w_1= 220 nm), and loop shaped antenna without offsets (p_1=500 nm, w_2= 175 nm, t_1= 40 nm, t_2= 20 nm, and t_4=90 nm). The intensity plotted is normalized to the magnetic field intensity of the incident wave. The simulation results of Figure 2-5a show that our loop shaped antenna with offsets has higher magnetic enhancement than the other two antennas at the resonant

wavelength of λ=1 μm. For our magnetic antenna design, we intentionally make the metallic strips have offsets. The function of the offsets is similar to that of the flared parts of the fan-rod antenna. The incident electric fields induce currents on the offsets and the offsets work as current reservoirs to inject additional currents into the loop part of the magnetic antenna. The additional currents increase the magnetic field enhancement within the current loops. To demonstrate that our magnetic antenna is a counterpart of the electric optical antenna, the distribution of the normalized magnetic field intensity for the unit cell of our magnetic antenna at the resonant wavelength of λ=1 μm is shown in Figure 2-5b. The magnetic field is tightly confined in a hot spot with subwavelength size. The full width at half maximum size of the hot spot of our magnetic antenna design is 20 nm in the z direction and 150 nm in the x direction, which is much smaller than the wavelength (λ=1 μm).

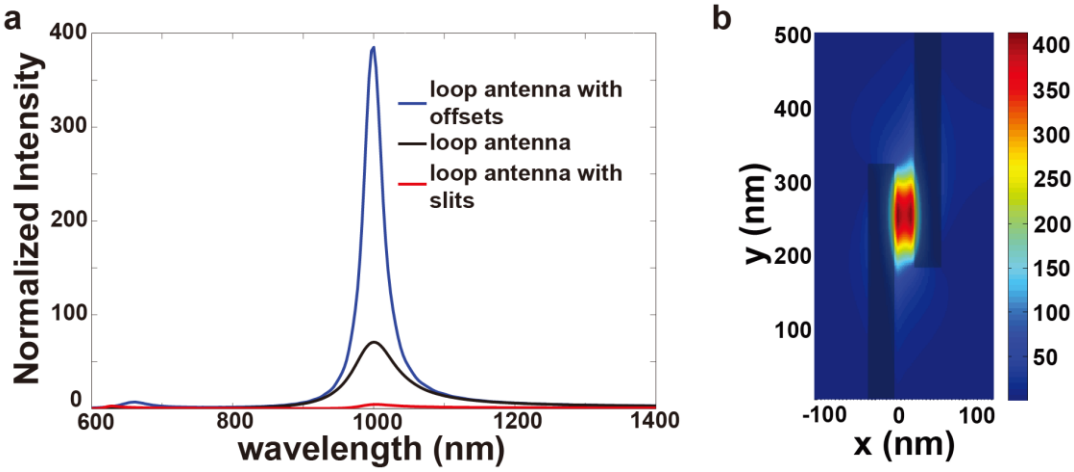

Figure 2-5. (a) Normalized magnetic field intensities (H^2) for loop shaped magnetic antenna with offsets, loop shaped magnetic antenna without offsets and loop shaped magnetic antenna with slits. (b) Distribution of normalized magnetic field intensity (H^2) at a wavelength of λ=1 μm for the loop shaped magnetic antenna with offsets. The dark parts are metallic strips.

Though the hot spots of enhanced magnetic field of our magnetic antenna cannot

trap non-magnetic particles and natural magnetic particles are not available at optical frequencies, the magnetic antenna design proposed here could be adjusted for trapping magnetic particles at frequencies, such as microwave frequencies, where magnetic particles are used. The high magnetic field enhancement indicates that our magnetic antenna has strong magnetic response.

2.4 Conclusions

We proposed two optical antennas with charge and current reservoirs: the fan-rod electric antenna and the loop shaped magnetic antenna with offsets. The charge reservoirs enable the fan-rod electric antenna to combine the advantages of the rod antenna and the bowtie antenna. A high electric field enhancement and a high ratio of field intensity in the center to that at the outer edges are simultaneously realized by our electric antenna design. By adding the current reservoirs, the loop-shaped magnetic antenna with offsets has stronger magnetic enhancement than it otherwise would. The high electric and magnetic field enhancement induced by charge and current reservoirs make our electric antenna and magnetic antenna useful for SERS, electromagnetic trapping and metamaterials. We believe the results of these designs provide insight into both electric and magnetic resonance mechanisms at optical frequencies, and will therefore enable the design of optical antennas with improved performance in the future.

2.5 References

[1]. K. B. Crozier, A. Sundaramurthy, G. S. Kino, and C. F. Quate, "Optical antennas: Resonators for local field enhancement," Journal of Applied Physics **94**, 4632-4642 (2003).
[2]. E. Cubukcu, E. A. Kort, K. B. Crozier, and F. Capasso, "Plasmonic laser

antenna," Applied Physics Letters **89**, 093120-093123 (2006).
[3]. N. Yu, E. Cubukcu, L. Diehl, M. A. Belkin, K. B. Crozier, F. Capasso, D. Bour, S. Corzine, and G. Hofler, "Plasmonic quantum cascade laser antenna," Applied Physics Letters **91**, 173113-173113 (2007).
[4]. N. Yu, E. Cubukcu, L. Diehl, D. Bour, S. Corzine, J. Zhu, G. Höfler, K. B. Crozier, and F. Capasso, "Bowtie plasmonic quantum cascade laser antenna," Opt. Express **15**, 13272-13281 (2007).
[5]. P. J. Schuck, D. P. Fromm, A. Sundaramurthy, G. S. Kino, and W. E. Moerner, "Improving the Mismatch between Light and Nanoscale Objects with Gold Bowtie Nanoantennas," Physical Review Letters **94**, 017402 (2005).
[6]. P. Mühlschlegel, H.-J. Eisler, O. J. F. Martin, B. Hecht, and D. W. Pohl, "Resonant Optical Antennas," Science **308**, 1607-1609 (2005).
[7]. J. Aizpurua, G. W. Bryant, L. J. Richter, F. J. García de Abajo, B. K. Kelley, and T. Mallouk, "Optical properties of coupled metallic nanorods for field-enhanced spectroscopy," Physical Review B **71**, 235420 (2005).
[8]. E. K. Payne, K. L. Shuford, S. Park, G. C. Schatz, and C. A. Mirkin, "Multipole Plasmon Resonances in Gold Nanorods," The Journal of Physical Chemistry B **110**, 2150-2154 (2006).
[9]. E. X. Jin, and X. Xu, "Radiation transfer through nanoscale apertures," Journal of Quantitative Spectroscopy and Radiative Transfer **93**, 163-173 (2005).
[10]. S. Nie, and S. R. Emory, "Probing Single Molecules and Single Nanoparticles by Surface-Enhanced Raman Scattering," Science **275**, 1102-1106 (1997).
[11]. J. Valentine, S. Zhang, T. Zentgraf, E. Ulin-Avila, D. A. Genov, G. Bartal, and X. Zhang, "Three-dimensional optical metamaterial with a negative refractive index," Nature **455**, 376-379 (2008).
[12]. C. Yan, Y. Cui, Q. Wang, and S. Zhuo, "Negative refractive indices of a confined discrete fishnet metamaterial at visible wavelengths," J. Opt. Soc. Am. B **25**, 1815-1819 (2008).
[13]. C. Yan, Y. Cui, Q. Wang, S. Zhuo, and J. Li, "Negative refraction with high transmission at visible and near-infrared wavelengths," Applied Physics Letters **92**, 241108-241103 (2008).
[14]. S. Gennady, and A. U. Yaroslav, "Negative index meta-materials based on two-dimensional metallic structures," Journal of Optics A: Pure and Applied Optics **8**, S122 (2006).
[15]. V. M. Shalaev, W. Cai, U. K. Chettiar, H.-K. Yuan, A. K. Sarychev, V. P. Drachev, and A. V. Kildishev, "Negative index of refraction in optical metamaterials," Opt. Lett. **30**, 3356-3358 (2005).
[16]. A. D. Rakic, A. B. Djuri?ic, J. M. Elazar, and M. L. Majewski, "Optical Properties of Metallic Films for Vertical-Cavity Optoelectronic Devices," Appl. Opt. **37**, 5271-5283 (1998).
[17]. J. B. Pendry, A. J. Holden, D. J. Robbins, and W. J. Stewart, "Magnetism from conductors and enhanced nonlinear phenomena," Microwave Theory and Techniques, IEEE Transactions on **47**, 2075-2084 (1999).
[18]. L. Ran, J. Huangfu, H. Chen, Y. Li, X. Zhang, K. Chen, and J. A. Kong, "Microwave solid-state left-handed material with a broad bandwidth and an ultralow loss," Physical Review B **70**, 073102 (2004).

[19]. D. Wang, L. Ran, H. Chen, M. Mu, J. A. Kong, and B.-I. Wu, "Experimental validation of negative refraction of metamaterial composed of single side paired S-ring resonators," Applied Physics Letters **90**, 254103-254103 (2007).
[20]. L. Peng, L. Ran, H. Chen, H. Zhang, J. A. Kong, and T. M. Grzegorczyk, "Experimental Observation of Left-Handed Behavior in an Array of Standard Dielectric Resonators," Physical Review Letters **98**, 157403 (2007).

3 Optical antennas integrated with concentric ring gratings: electric field enhancement and directional radiation

3.1 Introduction

Highly localized and enhanced electromagnetic fields are desirable for surface enhanced Raman scattering (SERS) [1]. One means for achieving this in a reproducible manner is using optical antennas [2-5]. However, optical antennas are usually much smaller than the focal spots of microscope objectives, especially those with low to moderate numerical apertures (NAs), leaving much of the illumination power not focused onto the optical antenna. In this Chapter, we propose a structure, consisting of an optical antenna integrated with a concentric ring grating that provides a highly enhanced field. The ring grating not only concentrates the illumination at its center, but also collimates the radiation of a dipole located there [6-8]. Ring gratings have been studied for beam shaping [7, 8], near field imaging [9, 10], and localized Raman enhancement [11]. In this Chapter, we conduct a comprehensive study of the field enhancement and dipole radiation properties of the antenna-integrated-with-ring-grating structure, including the effects of the NA of the lens used to focus light onto, and collect light from, the structure. We consider its application in enhanced Raman scattering.

3.2 Concentric ring grating concentrator

The concentric ring grating considered in this paper is illustrated in Figure 3-1. It

contains five concentric silver rings on top of a silver plate that contains a hole in the center. The medium surrounding the structure is taken to be free space. The geometric parameters are chosen to be: grating period p_1=530 nm, p_2=265 nm, h_1=h_2=40 nm, d=597.5 nm, and radius of center hole r=200 nm. These parameters are used in all simulations of this chapter

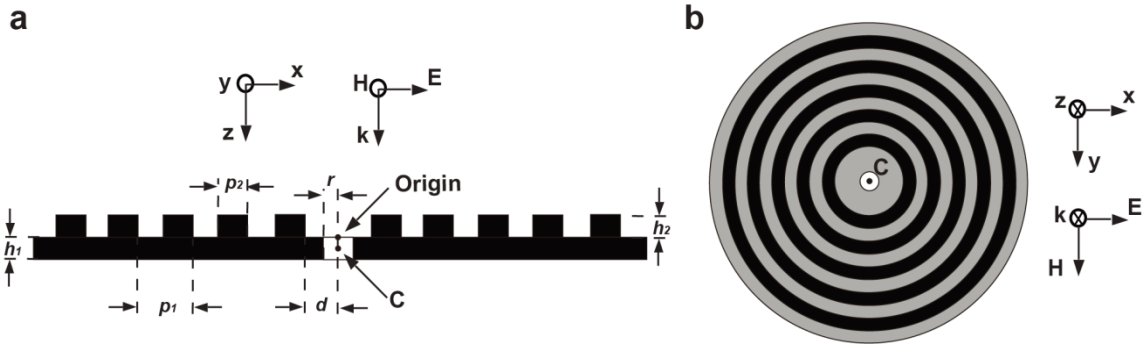

Figure 3-1. (a) Cross section of a concentric ring grating concentrator. (b) Top view of the concentric ring grating concentrator. Black circles are raised Ag rings.

The concentric ring grating is designed to concentrate the incident illumination of a plane wave propagating along the +z direction, with its electric and magnetic fields polarized in the xy plane. The optical properties of silver follow a Drude model (plasma frequency is 1.163×10^{16} rad/s and collision frequency is 1.435×10^{15} rad/s) in the calculations, which have been fitted to the data in Ref. [12].

As reviewed in Ref [13], the dispersion relation of the surface plasmon at the interface between metal and dielectric half-spaces is given by Equation (3.1).

$$k_\rho = k_0\sqrt{\frac{\varepsilon_d\varepsilon_m(\omega)}{\varepsilon_d+\varepsilon_m(\omega)}} \qquad (3.1)$$

In Equation (3.1), k_0 is the wave vector in air, ε_d is the relative permittivity of the dielectric and $\varepsilon_m(\omega)$ is the dispersive relative permittivity of the metal. As shown in Chapter 1, for the case of a plane wave normally incident on a flat air-metal boundary,

the incident wave has no wavevector component parallel to the boundary, and surface plasmons are not excited. On the other hand, the inclusion of a concentric ring grating with a period of p_1 on the boundary adds a wave vector component $k_\rho=2\pi/p_1$, enabling surface plasmon excitation. For p_1=530 nm, taking the optical properties of silver used here, Equation (3.1) predicts the excitation of the surface plasmon wave for illumination at λ=570 nm. To study the field enhancement properties, we perform a numerical simulation of the ring grating using the finite difference time domain (FDTD) method. The simulated structure is situated in free space. This is realized by using perfectly matched layers at the *x*, *y* and *z* boundaries. The mesh size is 4 nm for the concentric ring gratings. The incident wave propagates along the +*z* direction, with the electric field polarized in the *x* direction and magnetic field polarized in the *y* direction. The amplitude of the *x* component of the electric field, normalized to the incident field, at the center of the ring grating is shown in Figure 3-2a. In the discussion that follows, the "center" of the ring grating or the antenna is point *C* of Figure 3-1a. This is at the midpoint, in the *xy* plane, of the circular rings or the antenna gap, and 20 nm from the origin (see Figure 3-1a) in the *z*-direction. The amplitude peaks for a free space wavelength of λ= 585 nm, where the best concentration is achieved. This deviates slightly from the wavelength predicted by Equation (3.1) (λ=570 nm). Such a deviation is not unexpected, since the grating is placed on a silver plate of a finite thickness (h_2=40 nm). In addition to the five ring grating, we also simulate the four ring and the three ring cases. The peak values of the normalized amplitude of the *x* component of the electric field at the center of the four ring grating and the three ring grating are 5.53 and 4.65, respectively. Both of them are smaller than the peak value of 6.47 achieved by the five ring grating. This indicates that

the propagation loss is small enough for the surface plasmon waves excited at the outer rim of the five ring grating to propagate to the center. We will consider the five ring grating in the remainder of this chapter.

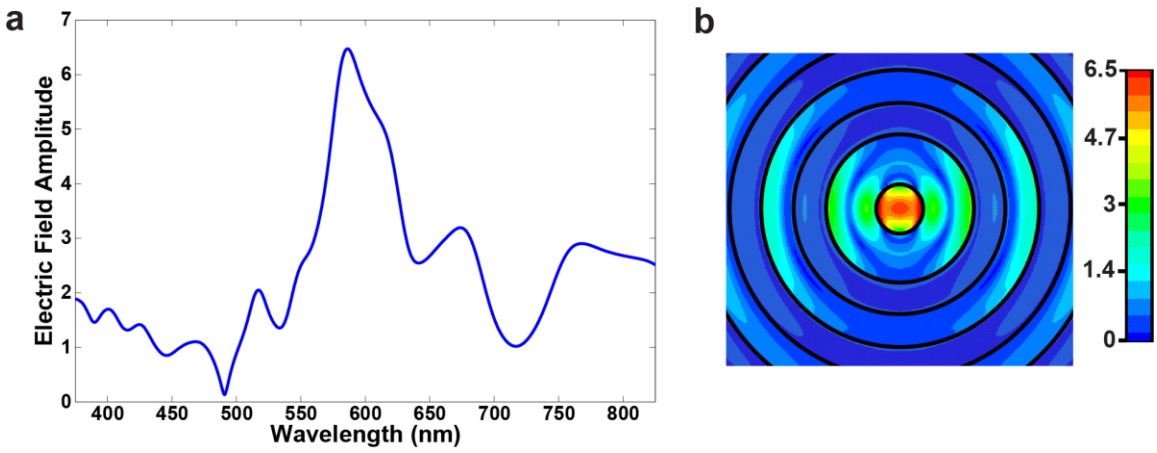

Figure 3-2. (a) Normalized x component of electric field at the center of the concentric ring grating concentrator. (b) Field distribution of central portion of concentric ring grating concentrator. Plot of the amplitude of x component of normalized electric field on top surface of the grating, for excitation at λ=585 nm.

In Figure 3-2b, the amplitude of the x component of the electric field profile on the top surface of the five ring grating is shown. The field amplitude plotted in Figure 3-2b has been normalized to the incident field. At the center of the concentric ring grating concentrator, the y and z components of the electric field are far smaller than the x component, and are therefore not plotted. The results indicate that the field is focused into a spot with a full width at half maximum (FWHM) of the intensity (proportional to E^2) of ~250 nm along y direction. This is smaller than half of the free space wavelength $\lambda/2$=292.5 nm. Three peaks are seen in the field intensity along x direction at the center hole, however. We believe that the two peaks at the edge of center hole are mainly due to the accumulation of charges at the edges of center hole and that the peak at the center is mainly due to the surface plasmon wave concentration. To study the concentration effect,

we conducted a FDTD simulation in which the concentric ring gratings are removed and only bare silver plate with center hole is considered. In the simulation for the bare silver plate with center hole, the excitation, mesh sizes and boundary conditions are same as those used in the simulation for concentric ring grating concentrator. The results for the bare silver plate with center hole (not shown here) show a similar field distribution as Figure 3-2b, but the field intensity at the center of the hole and its edges are weaker than those when concentric rings are included. The edges of the center hole in bare silver plate excite surface plasmon waves that interfere with each other, forming field distributions similar to those that result when concentric ring gratings are included. The inclusion of concentric ring gratings yields stronger excitation of surface plasmon waves, which results in larger field enhancement. The simulation results of the bare silver plate with center hole and the results in Figure 3-2 show that the field intensity of concentric ring grating at the center is 6 times larger than the one of bare silver plate with center hole. This indicates that the concentration effect is enhanced by concentric ring gratings. The simulation results show that the concentric ring grating concentrates the electric field with considerable field intensity enhancement at its center.

3.3 Integration of an optical antenna on the concentric ring grating

As shown in Figure 3-3, we now consider a fan-rod optical antenna, which will be integrated with the concentric ring grating later in this paper. Each half of the antenna consists of a rod and a flared semicircular part. As shown in Chapter 2, the rod is intended to provide a good confinement of charges at its apex, and the flared section to act as a reservoir of charges. This element combines the advantages of rod and bowtie

antennas [3, 5].

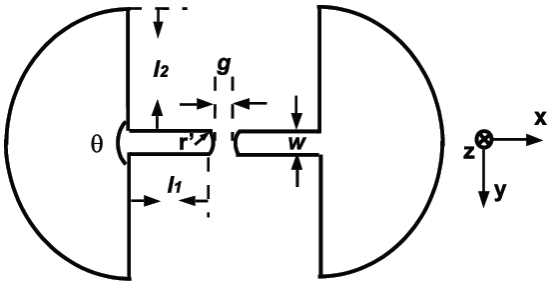

Figure 3-3. Fan-rod optical antenna.

In our FDTD simulation, the following geometric parameters are chosen for a silver antenna, to make the antenna resonant at λ=585 nm, the same wavelength at which the ring grating of Section 2 achieved peak enhancement. g=10 nm, r'=30 nm, w=20 nm, l_1=17 nm, l_2=33 nm, and $\theta=\pi$. The antenna thickness along the z direction is 40 nm. In all our simulations of the fan-rod antenna, the mesh around the fan-rod antenna including its gap is 2 nm and the mesh is 4 nm in the regions away from the antenna.

As shown in the inset of Figure 3-4a, the fan-rod antenna is positioned in the center hole of the ring grating. In the simulation, the incident wave propagates along the z direction with the electric field polarized in the x direction and the magnetic field polarized in the y direction. The normalized intensities of the x component of the electric field (E_x^2) at the center of the structures are shown in Figure 3-4a, for a single antenna and for an antenna integrated with a ring grating. The field intensity at the center of the optical antenna is enhanced 1.19×10^3 times by a single antenna, and is enhanced 4.46×10^4 times by an antenna integrated with a ring grating, at the resonant wavelength of λ=585 nm. This is due to the plane wave illumination being concentrated by the ring grating to its center hole, where the antenna is located. A plot of the instantaneous x component of the normalized electric field E_x on the antenna surface for illumination at

λ=585 nm is shown in Figure 3-4b. The field intensity is highly localized in the antenna gap and greatly enhanced, which is favorable for SERS.

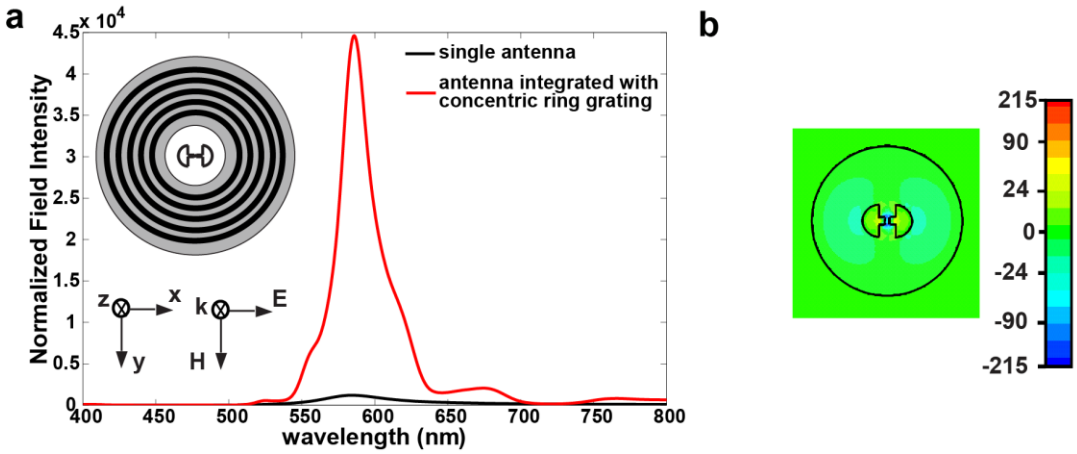

Figure 3-4. (a) E_x^2 at the center of a fan-rod antenna normalized to the incident wave, for a single antenna and an antenna integrated with a concentric ring grating. Inset: schematic of simulated structure. (b) Plot of instantaneous value of x component of normalized electric field, for excitation at λ=585 nm.

In the above analysis, we have calculated field enhancement under plane wave illumination, an assumption employed almost universally in optical antenna analysis (e.g. [2-5]), with a few exceptions [14-16]. Typically, however, an aplanatic lens, such as a microscope objective, would be used to focus light onto the antenna. An interesting question is therefore the effect of focused illumination on the field enhancement achieved both in the single, isolated antenna case, as well as the antenna integrated with the grating. This is considered in section 3.5.

3.4 Directionality enhancement

In order to collect the Raman scattering signals efficiently it is favorable to collimate the Raman scattering into a small solid angle. In this section, we show that the Raman scattering from molecules on an antenna integrated with a concentric ring is well collimated, which improves the effective Raman scattering enhancement factor. For

simplicity, we consider the molecules to be placed in the gap of the optical antenna.

A point dipole is used in our simulations to model the Raman scattering molecule. We have conducted simulations for the case of a point dipole at the center of a fan-rod antenna, and for the case of a point dipole at the center of a fan-rod antenna integrated with a concentric ring grating. The point dipole is polarized along the *x* direction and has the same dipole moment in both simulation cases. The far field radiation patterns in the *yz* plane and the *xz* plane are shown in Figure 3-5 for a dipole whose free space wavelength is λ=585 nm.

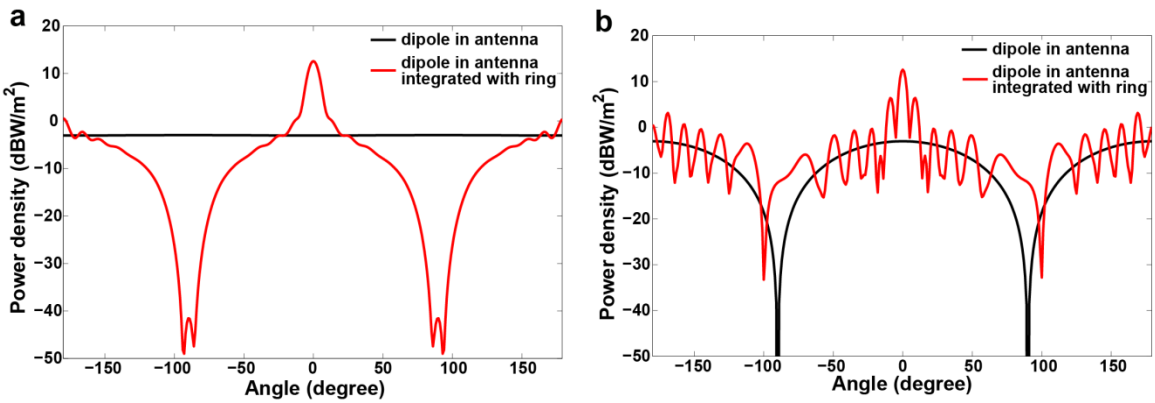

Figure 3-5. Far field radiation patterns of a point dipole at the center of a fan-rod antenna, and a point dipole at the center of a fan-rod antenna integrated with a concentric ring grating. The angles in the plots are the angles between the observation directions and the *-z* direction. The unit dBW/m^2 is defined as 10×log(power density). (a) *yz* plane. (b) *xz* plane.

Figure 3-5 shows that the radiation from a point dipole located at the center of the fan-rod antenna is more collimated into the *-z* direction when the antenna is integrated with a concentric ring grating. This is a reciprocal process to the ring grating's concentration of plane wave illumination into a small spot. It is interesting to notice that the radiation into the *–z* direction from the antenna-integrated-with-ring-grating structure is much stronger than into the *+z* direction. The rings function as an array of scatterers that collimate the radiation from the point dipole. The collimated radiation has a 3dB

angle-width of 8.5° in the *yz* plane and 4.5° in the *xz* plane, while without the ring grating the radiation is spread into a wider range of angles. Without the ring grating, the power density varies by less than 3dB for observation points in the yz plane (Figure 3-5a), and a 3dB angle-width of 87° in the xz plane is predicted (Figure 3-5b). In order to understand the effect of the radiation pattern upon the collection efficiency achieved in an experiment, it is necessary to consider the NA of the collection lens. The collection efficiency in this paper is defined as the power collected by the objective divided by the total power radiating from the structure. The power radiated by the dipole but absorbed by metal is not included in the total radiation power for the determination of collection efficiency. If we use a microscope objective of NA = 0.7 to collect the radiation, the collection efficiency is 69.7% for a dipole located at the center of the fan-rod antenna integrated with a ring grating, while the collection efficiency is only 29.8% without the ring grating. The latter is very close to the expected collection efficiency for a point dipole radiating into free space. In Table 1, the collection efficiencies for a dipole located at the center of the fan-rod antenna integrated with and without the concentric ring grating with collection lenses of different NAs are listed. As will be discussed further below, however, integration of the antenna with the ring grating increases the collected power more than the ratio of the collection efficiencies of Table 3-1. This is because the total radiated power is increased by the integration of the antenna with the ring grating.

Table 3-1. Collection efficiencies for a dipole located at the center of the fan-rod antenna integrated with and without the concentric ring grating for lenses with different NAs

NA	With grating	Without grating
0.1	46.9%	4.47%
0.4	64.5%	17.4%
0.7	69.7%	29.8%

From Table 3-1, it can be seen for low, medium and high NAs, collection efficiencies are improved by the concentric ring grating. Indeed, the collection efficiency with the grating structure using a low NA lens (0.1) is superior to that without the grating with a high NA lens (0.7).

A dipole with a given dipole moment can radiate more power when placed in an antenna's vicinity, a phenomenon known as the Purcell effect [17]. The power intensity radiating into the $-z$ direction, i.e. into a direction opposite to that of the illumination, is enhanced 1.19×10^3 times for the fan-rod antenna compared to the radiation from the same dipole in free space. Similarly, for a fan-rod antenna integrated with the ring grating, the enhancement is 4.37×10^4 times. These enhancement factors are in good agreement with the field intensity enhancement factors simulated in 3.3 for the case of incident waves in the $+z$ direction. This is expected from the reciprocity theorem [18], because the dipole couples to the external optical mode with the same strength as the external optical mode excites the dipole. The total radiation power from the antenna-only structure is enhanced 1.19×10^3 times. That this is the same factor as the $-z$ direction intensity enhancement is due to its radiation pattern being very close to that of a point dipole in free space. The total radiation power from the antenna-grating structure is enhanced 2.03×10^3 times, compared to a dipole in free space. That this is smaller than its $-z$ direction intensity enhancement is due to its radiation into wider angles being weak. As noted above, the improvement that comes through the integration of the antenna with the ring is not the ratio of the collection efficiencies of Table 3-1. Rather, one needs to take into account the fact that the total radiation power is ~1.7 times larger for the antenna-ring structure than the antenna-only structure. In addition to predicting performance, the

calculations permit us to interpret the role of the grating. The intensity at the center of the antenna under external illumination at normal incidence is ~38 times larger for the antenna-ring structure than the antenna-only structure. That this is much larger than the increase in radiation power indicates that the ring grating is more of a concentrator than a resonator.

3.5 Raman scattering enhancement

We now calculate the enhancement in the collected SERS signals that should result from use of the antenna-only and antenna-ring structures. We consider Raman scattering from a molecule at the center point of the structure, i.e in the antenna gap. For simplicity, we assume both the illumination and the Raman scattering are at the resonant wavelength of 585 nm, i.e. that the Stokes shift is zero. The enhancement factors we calculate are comparisons between the collected SERS signals from a molecule in the antenna-only or antenna-ring structures to those from a molecule in free space, with illumination and collection optics unchanged. A common approach for calculating SERS electromagnetic enhancement factor is to take it as the fourth power of the electric field enhancement under plane wave illumination. This assumes plane wave illumination and collection, i.e. that the NA of illumination and collection optics approach zero. Rather than using this approach, we instead calculate SERS electromagnetic enhancement factor using the following equation which accounts for the NA of illumination and collection optics:

$$EF = \left(\frac{E^2|_{withantenna}}{E^2|_{freespace}}\right)\left(\frac{P_{rad}|_{withantenna}}{P_{rad}|_{freespace}}\right)\left(\frac{\eta_{collection}|_{withantenna}}{\eta_{collection}|_{freespace}}\right) \quad (3.2)$$

The first term in parentheses is the ratio of the intensity (square of electric field) of illumination at the dipole position in an antenna-only or antenna-ring structure to the intensity of illumination at the dipole position in free space. For calculating each of these

intensities, focused illumination with a given NA is employed, as described below. The second term in parentheses is the ratio of the power radiated by a dipole with a given dipole moment in an antenna-only or antenna-ring structure to that radiated when the dipole is in free space. The third term in parentheses is the ratio of the collection efficiencies at a given NA for a dipole in an antenna-only or antenna-ring structure to that for a dipole in free space.

To calculate the first term in parentheses of (3.2), we employ the vector diffraction theory of Richards and Wolf [19] that describes a method by which the fields at the focus of a lens illuminated by a plane wave can be found. Because we consider a dipole oriented in the *x* direction, we only consider the *x* component of the electric field. From Ref [19], the *x* component of the electric field at the focus of a lens with $NA=\sin\theta_{max}$ is given by:

$$E_x\,|_{free\ space} = \frac{ikfe^{-ikf}}{2\pi}\int_0^{\theta_{\max}}\int_0^{2\pi} E_\infty(\theta,\phi)\sin\theta\ d\phi\, d\theta \qquad (3.3a)$$

$$E_\infty(\theta,\phi) = E_0\frac{1}{2}\left[(1+\cos\theta)-(1-\cos\theta)\cos 2\phi\right](\cos\theta)^{1/2} \qquad (3.3b)$$

In Equation (3.3a) and (3.3b), *k* is the wavevector in free space, *f* is the focal length of the objective and E_0 is the amplitude of the electric field of the plane wave.

In Equation (3.3), the *x* component of the electric field at the focus is found by integration of the plane waves converging to the focus over possible angles of incidence. To modify this expression for the case of focused illumination incident on an antenna-only structure or antenna-ring structure, each of the plane wave components must be multiplied by a prefactor. The prefactor is equal to the electric field enhancement occurring for plane wave illumination of the antenna-only structure or antenna-ring

structure at the angle of incidence. To determine the prefactor, one could perform a series of simulations of the field resulting from plane wave illumination of the antenna-only structure or antenna-ring structure at different angles of incidence. However, it is also possible to determine the prefactor from a single simulation, in which a dipole is placed at the center of the antenna-only or antenna-ring structure, and the far-field radiated at different angles is found. Because of the reciprocity theorem, this single simulation yields the required information. In Ref. [18], reciprocity theorem is used to find the relationship between radiated far-fields and local fields. In Ref. [18], two dipoles, and the fields that they create, are considered. A dipole $\vec{d}_0$ is placed in the vicinity of arbitrary nanostructures, and generates an electric field $\vec{E}_{far}$ at some position in the far-field. A dipole $\vec{d}_{far}$ is placed at the same far-field position, and generates field $\vec{E}_{loc}$ at the position of dipole $\vec{d}_0$. These dipole moments and fields are related by:

$$\vec{d}_0 \cdot \vec{E}_{loc} = \vec{d}_{far} \cdot \vec{E}_{far} \quad (3.4)$$

Following this approach, we place a dipole with dipole moment $\vec{d}_{far}$ oriented perpendicular to the radial direction $\hat{r}$ far from the antenna-only or antenna-grating structure. Because the distance from the antenna-only or antenna-grating structure to the dipole $\vec{d}_{far}$ is much greater than the wavelength, the field generated by the dipole $\vec{d}_{far}$ that illuminates the antenna-only or antenna-grating structure can be regarded as plane wave. If the orientation $\hat{e}_p(\theta,\phi)$ of the dipole $\vec{d}_{far}$ is along the polarization direction of the field generated by the objective lens and the magnitude d_{far} of the dipole moment $\vec{d}_{far}$ is chosen appropriately, the fields generated by the dipole $\vec{d}_{far}$ that illuminate the antenna-only or

antenna-grating structure are same as those that would be generated by the objective lens. Following Equation (3.4), we obtain:

$$d_0\hat{x}\cdot\vec{E}\,|_{with\ antenna}(\theta,\phi)=d_{far}\hat{e}_p(\theta,\phi)\cdot\vec{E}\,|_{far\ with\ antenna}(\theta,\phi) \quad (3.5)$$

where $d_0\hat{x}$ is the dipole moment of the dipole used to model the Raman scattering molecule, $\vec{E}\,|_{with\ antenna}(\theta,\phi)$ is the enhanced electric field at the center of the antenna-only or antenna-grating structure, and the direction $\hat{e}_p(\theta,\phi)$ of $\vec{d}_{far}$ is the polarization direction of the wave generated by the objective lens as given in Ref. [19]. $\vec{E}\,|_{far\ with\ antenna}(\theta,\phi)$ is the far-field at the position at which the dipole $\vec{d}_{far}$ is placed, generated by the dipole $d_0\hat{x}$. Similarly, when the antenna-only or antenna-grating structure is removed, the reciprocity theorem [18] yields the following:

$$d_0\hat{x}\cdot\vec{E}\,|_{with\ antennaremoved}(\theta,\phi)=d_{far}\hat{e}_p(\theta,\phi)\cdot\vec{E}\,|_{far\ free\ space}(\theta,\phi) \quad (3.6)$$

where $\vec{E}\,|_{far\ free\ space}(\theta,\phi)$ is the far field generated by dipole $d_0\hat{x}$ in the absence of the antenna-only or antenna-grating structure and $\vec{E}\,|_{with\ antennaremoved}(\theta,\phi)$ is the field generated by $\vec{d}_{far}$ at the place where $d_0\hat{x}$ is placed in the absence of the antenna-only or antenna-grating structure. Comparing Equations (3.5) and (3.6) yields the field enhancement prefactor:

$$W(\theta,\phi)=\frac{E_x\,|_{with\ antenna}(\theta,\phi)}{E_x\,|_{with\ antennaremoved}(\theta,\phi)}=\frac{\hat{e}_p(\theta,\phi)\cdot\vec{E}\,|_{far\ with\ antenna}(\theta,\phi)}{\hat{e}_p(\theta,\phi)\cdot\vec{E}\,|_{far\ free\ space}(\theta,\phi)} \quad (3.7)$$

As indicated by the subscript *x*, this represents the field enhancement of the *x* component of the electric field. Using Equations (3.5), (3.6) and (3.7), the *x* component of the electric field at the center of the antenna-only or antenna-grating structure is given by:

$$E_x\,|_{with\ antenna} = \frac{ikfe^{-ikf}}{2\pi}\int_0^{\theta_{\max}}\int_0^{2\pi} W(\theta,\phi)E_\infty(\theta,\phi)\sin\theta\ d\phi\, d\theta \quad (3.8)$$

Using Equations (3.3) and (3.8), the first term of Equation (3.2) is found for both the antenna-only and antenna-ring structures. The second term of Equation (3.2) is 1.19×10^3 times for the antenna-only structure, and 2.03×10^3 times for the antenna-grating structure, as described in section 3.4. The third term of Equation (3.2) is very close to unity for the antenna-only structure, as its radiation pattern is almost identical to that of a point dipole. For the antenna-grating structure, this term is equal to the ratio of collection efficiencies of the with- and without-grating structures of Table 3-1. The third term of Eq. (2) is therefore equal to 10.49, 3.71 and 2.34 for NAs of 0.1, 0.4 and 0.7, respectively.

Using Equations (3.2)-(3.8), the SERS electromagnetic enhancement factors of the antenna-grating and antenna-only structures are calculated in Table 2 for different NAs of the lens used to focus light onto, and collect light from, the device. In Table 3-2, we assume equal NA values of illumination and collection optics. In experiments, if the collimated excitation laser beam does not fill the whole aperture of the focusing lens, the illumination optics will have a smaller NA, and the ring grating will contribute to a larger enhancement factor than in Table 3-2 by its additional concentration of illumination.

Table 3-2. SERS electromagnetic enhancement factors of antenna-grating and antenna-only structures calculated for different NAs of illumination/collection optics

NA	Antenna-grating structure	Antenna-only structure
0.1	2.23×10^8	1.35×10^6
0.4	1.01×10^7	1.35×10^6
0.7	4.27×10^6	1.35×10^6

From Table 3-2, it can be seen that the antenna-grating structure is predicted to achieve higher values of SERS enhancement factors than the antenna-only structure. The

improvement is particularly dramatic when the NA is low (0.1), achieving a value of ~165 times. At medium (0.4) and high (0.7) values of NA, the improvement factors are ~7.5 and ~3.2 times, respectively. That the improvement arising from the use of the grating is greatest at low NA is due to the fact that the additional focusing it provides is most advantageous when the illumination is weakly focused and the collection angle is small. It is interesting to note that the enhancement factor for the antenna-only structure is not affected by the NA. This is due to the fact that, like the molecule being modeled, the far-field radiation pattern of the antenna is almost identical to that of a point dipole. The first term in parentheses of Equation (3.2) is therefore not affected by the NA. The second term does not depend on the NA. The third term is close to unity because of the fact that the radiation patterns of the dipole in free space, and the dipole in the antenna are almost identical.

As described above, the integration of the antenna with the grating improves performance by concentrating the input illumination to improve excitation, and collimating the Raman scattering to improve collection efficiency. Despite minor improvements with high NA lenses, gratings are more versatile and less expensive than high NA glass lenses. Thus far, we have considered an antenna with its dipole moment in the plane of the substrate. Another interesting possibility is discussed in the following paragraph.

The field intensity and the Purcell effect, and consequently the Raman enhancement factor of the antenna, increases significantly with shortening the gap. While a 10 nm gap is about the limit of planar lithographic techniques, such as electron beam lithography and focused ion beam modification, it is easy to achieve a distance of less

than 1 nm in the vertical direction between the tip of an atomic force microscope and a planar surface. It is interesting to consider whether one could perform tip-enhanced Raman scattering (TERS) with molecules at this position [20]. In TERS experiments, it is necessary to ensure that there be an appreciate component of the electric field along the tip axis for field enhancement. A spiral ring device could offer a means for optimizing this. Using spiral rings, as distinct from the concentric rings considered in this paper thus far, an electric field polarization vertical to the substrate can be achieved at the center of the pattern [21].

3.6 Conclusions

In this Chapter, we have conducted a theoretical study on the use of concentric ring gratings to improve the performance of optical antennas for SERS. Improvements to the excitation intensity, radiated power and collection efficiency were considered for different values of NA. The results revealed that the grating is predicted to improve the SERS enhancement factor by close to two orders of magnitude at low NA (0.1), close to an order of magnitude at moderate NA (0.4), and by several times at high NA (0.7). We anticipate that both the results and calculation methodology we introduce here could serve as a powerful approach toward the design of structures for improving the SERS performance of optical antennas.

3.7 References

[1]. D. A. Long, *Raman spectroscopy* (McGraw-Hill International Book Company, 1977).
[2]. K. B. Crozier, A. Sundaramurthy, G. S. Kino, and C. F. Quate, "Optical antennas: Resonators for local field enhancement," Journal of Applied Physics **94**, 4632-4642

(2003).
[3]. E. Cubukcu, E. A. Kort, K. B. Crozier, and F. Capasso, "Plasmonic laser antenna," Applied Physics Letters **89**, 093120-093123 (2006).
[4]. N. Yu, E. Cubukcu, L. Diehl, M. A. Belkin, K. B. Crozier, F. Capasso, D. Bour, S. Corzine, and G. Hofler, "Plasmonic quantum cascade laser antenna," Applied Physics Letters **91**, 173113-173113 (2007).
[5]. P. J. Schuck, D. P. Fromm, A. Sundaramurthy, G. S. Kino, and W. E. Moerner, "Improving the Mismatch between Light and Nanoscale Objects with Gold Bowtie Nanoantennas," Physical Review Letters **94**, 017402 (2005).
[6]. H. J. Lezec, A. Degiron, E. Devaux, R. A. Linke, L. Martin-Moreno, F. J. Garcia-Vidal, and T. W. Ebbesen, "Beaming Light from a Subwavelength Aperture," Science **297**, 820-822 (2002).
[7]. L. Martín-Moreno, F. J. García-Vidal, H. J. Lezec, A. Degiron, and T. W. Ebbesen, "Theory of Highly Directional Emission from a Single Subwavelength Aperture Surrounded by Surface Corrugations," Physical Review Letters **90**, 167401 (2003).
[8]. M. Beruete, I. Campillo, J. S. Dolado, J. E. Rodriguez-Seco, E. Perea, F. Falcone, and M. Sorolla, "Very low-profile "Bull's Eye" feeder antenna," Antennas and Wireless Propagation Letters, IEEE **4**, 365-368 (2005).
[9]. K. Ishihara, T. Ikari, H. Minamide, J.-i. Shikata, K. Ohashi, H. Yokoyama, and H. Ito, "Terahertz Near-Field Imaging Using Enhanced Transmission through a Single Subwavelength Aperture," Japanese Journal of Applied Physics **44**, L929 (2005).
[10]. K. Ishihara, K. Ohashi, T. Ikari, H. Minamide, H. Yokoyama, J.-i. Shikata, and H. Ito, "Terahertz-wave near-field imaging with subwavelength resolution using surface-wave-assisted bow-tie aperture," Applied Physics Letters **89**, 201120-201123 (2006).
[11]. Q. Min, M. J. L. Santos, E. M. Girotto, A. G. Brolo, and R. Gordon, "Localized Raman Enhancement from a Double-Hole Nanostructure in a Metal Film," The Journal of Physical Chemistry C **112**, 15098-15101 (2008).
[12]. A. D. Rakic, A. B. Djuri?ic, J. M. Elazar, and M. L. Majewski, "Optical Properties of Metallic Films for Vertical-Cavity Optoelectronic Devices," Appl. Opt. **37**, 5271-5283 (1998).
[13]. W. L. Barnes, A. Dereux, and T. W. Ebbesen, "Surface plasmon subwavelength optics," Nature **424**, 824-830 (2003).
[14]. K. Sendur, W. Challener, and O. Mryasov, "Interaction of spherical nanoparticles with a highly focused beam of light," Opt. Express **16**, 2874-2886 (2008).
[15]. K. Sendur, "An integral equation based numerical solutionfor nanoparticles illuminated with collimatedand focused light," Opt. Express **17**, 7419-7430 (2009).
[16]. K. Sendur, and A. Sahinöz, "Interaction of radially polarized focusedlight with a prolate spheroidalnanoparticle," Opt. Express **17**, 10910-10925 (2009).
[17]. E. M. Purcell, "Spontaneous Emission Probabilities at Radio Frequencies " Physical Review **69**, 681 (1946).
[18]. E. C. Le Ru, and P. G. Etchegoin, "Rigorous justification of the |E|4 enhancement factor in Surface Enhanced Raman Spectroscopy," Chemical Physics Letters **423**, 63-66 (2006).
[19]. B. Richards, and E. Wolf, "Electromagnetic Diffraction in Optical Systems. II. Structure of the Image Field in an Aplanatic System," Proceedings of the Royal Society of London. Series A. Mathematical and Physical Sciences **253**, 358-379 (1959).

[20]. E. Bailo, and V. Deckert, "Tip-enhanced Raman scattering," Chemical Society Reviews **37**, 921-930 (2008).
[21]. Y. Gorodetski, A. Niv, V. Kleiner, and E. Hasman, "Observation of the Spin-Based Plasmonic Effect in Nanoscale Structures," Physical Review Letters **101**, 043903 (2008).

4 High directivity optical antenna substrates for surface enhanced Raman scattering

4.1 Introduction

In early SERS work, SERS substrates were often rough metallic surfaces [1] and aggregates [2, 3] made by bottom-up methods. More recent studies have centered on highly controllable and reproducible SERS substrates [4-6] fabricated by top-down methods. It has been known for some time [7] that these structures can be thought of as antennas. Efforts have been made recently on engineering these optical antennas (OAs), to maximize the local field enhancement and confinement [8-12]. In most previous work, OAs were formed on dielectric substrates [8-12]. In their basic configuration of two antenna arms separated by a gap, relatively few design options exist for improving the field enhancement. Indeed, the predominant approach involves modifying the lengths of different parts of the antenna (e.g. gap width [8]), though optimized shapes for the antenna arms have also been considered [13]. Furthermore, emission of the Raman signal from these basic designs occurs into a wide range of angles, which makes the collection of the SERS signal inefficient.

To improve the performance of OAs for SERS applications, a variety of methods have been proposed. These include reducing the width of the gaps between arms of the OA [8], OAs with double resonances [14-16], integrating OAs with dielectric and metallic photonic crystals and related structures [17, 18], and engineering the OA

emission patterns [19-21]. These methods have been generally pursued with the goal of either improving the local field enhancement or making the collection of the SERS signal more efficient. In this chapter, we integrate OAs with surrounding nanostructures (gold strips and gold reflector) that simultaneously improve the local field enhancement and SERS collection efficiency. Average SERS enhancement factors up to 1.2×10^{10} are experimentally demonstrated with the OA design we introduce.

4.2 Design and numerical characterization

4.2.1 Design of high directivity optical antenna substrates

The SERS substrate we introduce in this work is illustrated as Figure 4-1. It is a four-layer structure consisting of a silicon substrate, a gold mirror, an SiO_2 spacer and gold strips and OAs. This design yields larger local field enhancement than OAs on dielectric substrates by offering two additional field enhancement channels. First, the gold mirror introduces images which couple with the OAs to generate larger local fields. Second, the strips excite surface plasmon polaritons (SPPs) on the gold film, yielding enhanced fields at the midpoints between them, at which the OAs are located. The OAs therefore experience stronger excitation. These two enhancement channels are verified numerically in the following two sections.

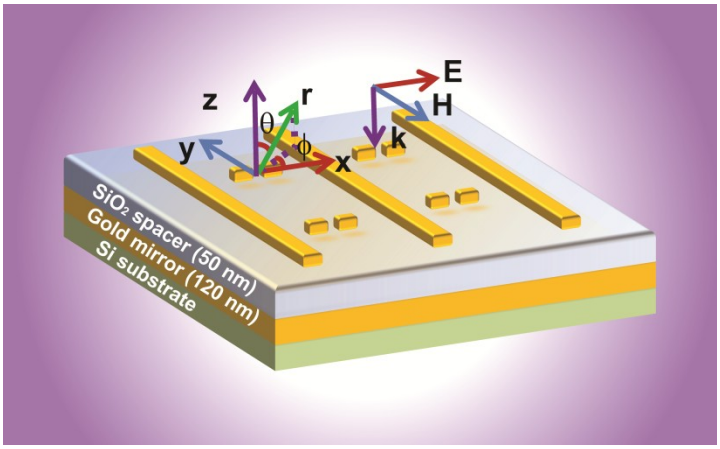

Figure 4-1. Schematic of SERS substrate introduced in this chapter, consisting of OAs integrated with gold strips and gold mirror. The OAs and gold strips are 30 nm thick. The gold strips are 110 nm wide. The OAs consist of pairs of gold rods with rounded outer ends. Each rod is 85 nm long. The outer ends have radii of curvature of 30 nm, while the inner ends are flat. The width of the rods in the *y* direction is 60 nm. The inner ends of the rods are separated by gaps of 5 nm. The *x*- and *y*-periods of the structure are both 730 nm.

4.2.2 Local field enhancement

We use the finite difference time domain (FDTD) method to evaluate the local field enhancement of the proposed design. In Figure 4-2**,** we plot the simulated intensity enhancements (the ratio between local field intensity and incident intensity) that result from three different configurations. The first (Figure 4-2a) consists of a two dimensional array (730 nm period) of OAs on an SiO_2 substrate (i.e. without strips and mirror). The second (Figure 4-2b) consists of a two dimensional array (730 nm period) of OAs formed above a gold mirror with an SiO_2 spacer layer. The third configuration (Figure 4-2c) is the same as that illustrated as Figure 4-1. In all three cases, normally-incident plane wave illumination with polarization as shown in Figure 4-1 is employed. The dimensions of the OAs, the dimensions of the gold strips, and the thicknesses of SiO_2 layer and gold mirror are the same as those indicated in Figure 4-1. The simulations are performed at an illumination wavelength of λ=785 nm.

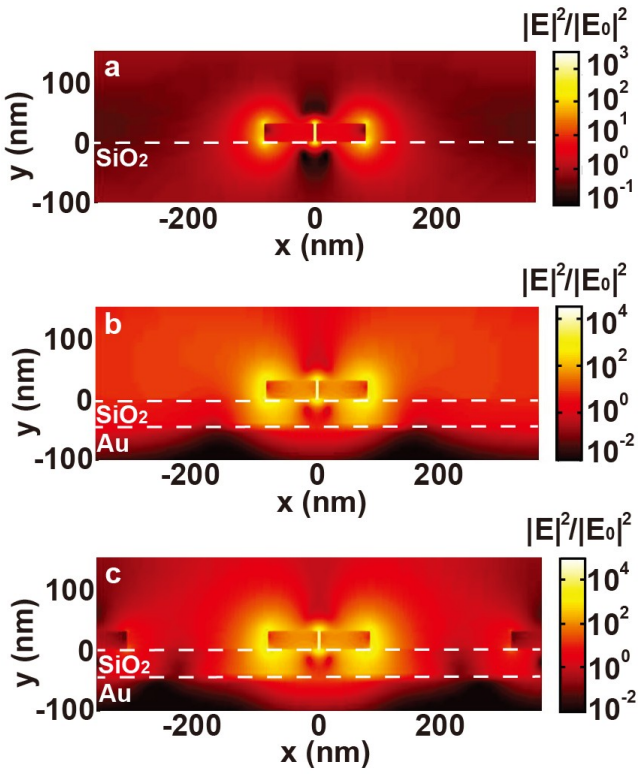

Figure 4-2. (a) Calculated intensity enhancement (ratio between intensity $|E|^2$ of enhanced local field and intensity $|E_0|^2$ of incident wave) in *xz* plane resulting from array of OAs on SiO_2 substrate. (b) Calculated intensity enhancement in *xz* plane resulting from array of OAs above gold mirror with SiO_2 spacer. (c) Calculated intensity enhancement in *xz* plane resulting from array of OAs integrated with gold strips, SiO_2 spacer and gold mirror.

The simulation results shown in Figure 4-2a and Figure 4-2b reveal that the intensity enhancement in the gap midpoint (15 nm above top surface of SiO_2 layer) for an array of OAs above a gold mirror is ~6.2 times larger than that for an array of OAs on a SiO_2 substrate (Figure 4-2a). This improvement is the result of the coupling between the OAs and gold mirror. It can be seen that the intensity enhancement in the midpoint of the OAs above the gold mirror (Figure 4-2b) is improved by an additional ~3.3 times when gold strips are added to the device (Figure 4-2c). This is because the gold strips generate SPPs that interfere constructively at the midpoints between the strips, resulting in enhanced fields that in turn excite the OAs more strongly. These two effects - the

coupling supported by gold mirror and larger excitation generated by the strips - result in the intensity enhancement being ~20 times larger for the device we introduce (Figure 4-2c) than that of OAs on an SiO_2 substrate Figure 4-2a). These simulations demonstrate that the gold film and gold strips provide a means for increasing the field enhancement available with OAs, which is advantageous for SERS.

4.2.3 Emission Enhancement

SERS is a technique that enhances the Raman signals by two processes: excitation enhancement and emission enhancement. The excitation process is as discussed in last section: the large local fields achieved by our designs enhance the Raman dipole moments of molecules in the vicinity of the OAs. The emission enhancement is further divided into two parts. The first part is the enhancement of total Raman emission power generated by molecules. This is the reverse process of local field enhancement. According to the reciprocity theorem [22], the large local field enhancement achieved by our design indicates strong enhancement of the total emission power of the molecules in the vicinity of OAs. The second part is the enhancement of collection efficiency (the ratio between Raman signals collected and total emitted signals). To obtain large collection efficiency, engineering of the Raman emission pattern is necessary. In the design we introduce, the strips act as secondary scatters, collimating the emission pattern into the $+z$ direction, which is quite favorable for the back scattering configuration, a Raman microscope, that we employ in the experiments. To understand the collimation phenomenon, the emission patterns of OAs in the three configurations of Figure 4-2 are simulated using a method [23] based on the reciprocity theorem [22]. In summary, this

involves performing simulations that calculate the local electric fields at the OA midpoints (middle of gap) when the structures are illuminated by plane waves propagating along the (θ,ϕ) direction (θ and ϕ are defined in Figure 4-1). For each (θ,ϕ) direction, two simulations are performed. In one, the plane wave is polarized along the θ direction. In the other, the polarization is along the ϕ direction. Due to the fact that the axis of each OA is along the *x* direction, the electric field at the OA midpoint is mostly along the *x* direction. From the reciprocity theorem [22], we know that the ratio between the intensity of the *x* component of the electric field calculated in this way and the intensity of the incident plane wave corresponds to the ratio between the intensity ($|E(\theta,\phi)|^2$) of the electric fields radiated in the (θ,ϕ) direction by a dipole (modeling the molecule) oriented along the *x* direction, placed at OA midpoint, and the intensity ($|E_{free}|^2$) of the fields radiated in $+z$ direction by the same dipole placed in free space. These simulations are conducted for different observation directions (θ,ϕ). The calculated intensity ratios found in this way are illustrated in Figure 4-3. These ratios represent the intensities of the power radiated into different directions by an *x*-directed dipole placed at the OA midpoint normalized to the power intensity radiated into the $+z$ direction by the same dipole placed in free space. These calculations are performed at a free space wavelength of λ=857.1 nm, which corresponds to the 1072 cm^{-1} Raman line when an excitation wavelength of λ=785 nm is used. This is chosen because it corresponds to one of the lines of Benzenethiol Phenyl mercaptan Thiophenol (benzenethiol), the molecule that is used in the Raman experiments described later.

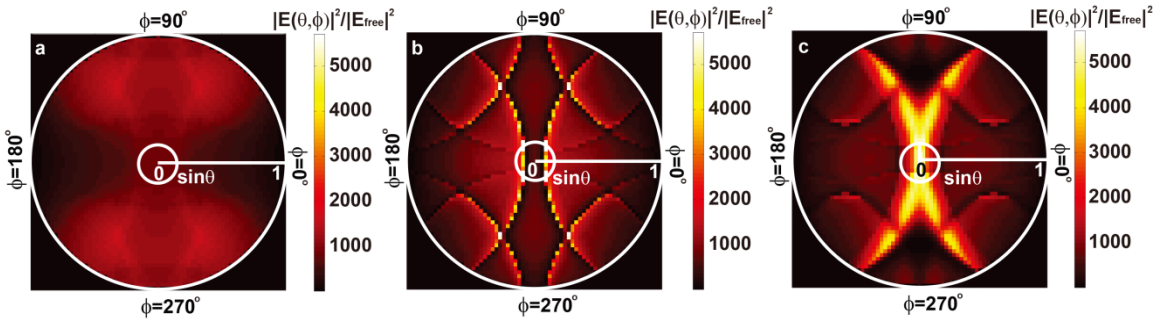

Figure 4-3. Simulated emission patterns of Raman dipole oriented in *x* direction and placed within gap of OA in three different configurations. Free space wavelength of λ=857.1 nm is employed, corresponding to 1072 cm^{-1} Raman line with λ=785 nm excitation. In all cases, periodicities in the *x* and *y* directions are both 730 nm. (a) Array of OAs on an SiO_2 substrate. (b) Array of OAs above gold mirror with SiO_2 spacer. (c) Array of OAs above gold mirror with gold strips. All the emission patterns are for the upper half space. Inner and outer circles represent angles θ such that sinθ takes values of 0.15 and 1.0, respectively.

The results in Figure 4-3 show that our design not only generates strong signals but also collimates Raman emission in the +*z* direction (sinθ=0). Compared with a dipole placed in free space, our design improves the total power radiated into the upper half space by three orders of magnitude (~1600). This is because the Purcell factor [24] experienced by Raman molecule is improved by the OAs, mirror and gratings. Additionally, the results in Figure 4-3c reveal that the full widths at half radiation power of our design are 6 degrees and 40 degrees in the *xz* and *yz* planes, respectively. This indicates that the majority of the Raman emission occurs into a small range of angles about the +*z* direction. It can be seen from Figure 4-3 that the confinement that occurs with this structure is considerably better than that occurring with the OAs on SiO_2 or OAs above mirror with SiO_2 spacer (but no strips). The collimation property of our design improves the collection efficiency of the Raman emission. If an objective lens with a numerical aperture (NA) of 0.15 is employed to collect the Raman emission, only that within the range of directions indicated by the inner circle of each part of Figure 4-3 is

collected. The total collected Raman emission, assuming NA=0.15, is found for each configuration by integration over each inner circle. Performing this integration shows that in the design we introduce (Figure 4-3c), the collected power is ~3.6 times that occurring for the OAs above the gold mirror (Figure 4-3b), and ~6 times that of the OAs on the SiO_2 substrate (Figure 4-3a). This affirms the ability of the device we introduce to achieve emission enhancement via increasing the total emitted power, as well as improving its directionality.

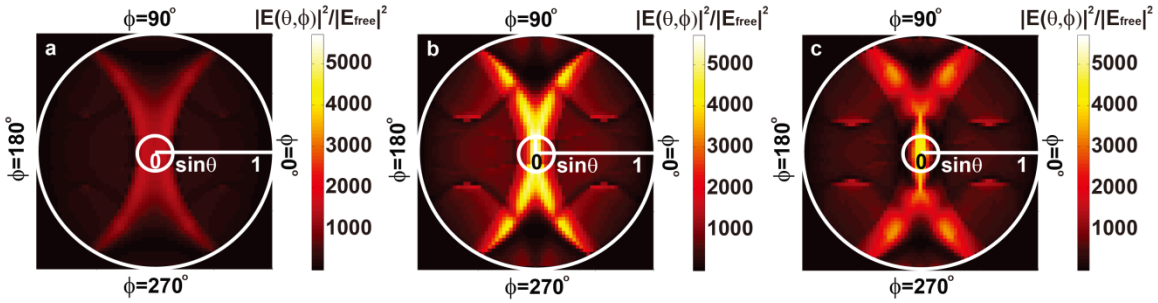

Figure 4-4. Simulated emission patterns of Raman dipole oriented in *x* direction and placed within gap of OA in three different configurations. Free space wavelength of λ=857.1 nm is employed, corresponding to 1072 cm^{-1} Raman line with λ=785 nm excitation. In all cases, periodicities in the *x* and *y* directions are both 730 nm. (a) Array of OAs above gold mirror with gold strips and 30 nm thick SiO_2 spacer. (b) Array of OAs above gold mirror with gold strips and 50 nm thick SiO_2 spacer. (c) Array of OAs above gold mirror with gold strips and 70 nm thick SiO_2 spacer. All the emission patterns are for the upper half space. Inner and outer circles represent angles θ such that sinθ takes values of 0.15 and 1.0, respectively

The parameters such as periodicities and SiO_2 spacer thickness of our design are optimized such that good balance between total emitted power and directionality is achieved. As shown in Figure 4-4, the shapes of emission patterns for OAs integated with gold mirror and strips are similar to one another, but have different intensities. The similar shapes of emission pattern result from the fixed periodicities (fixed grating effect). All the emissions are collimated. The varied intensities are due to different thickness of SiO_2 spacer layer (varied impedance matching conditions) [18]. It is seen that the

emission (Figure 4-4b) of the design with parameters shown in Figure 4-1 is the strongest among the three patterns. It can be seen in Figure 4-5 that some of the emission patterns (Figure 4-5a and Figure 4-5c) for OAs integated with gold mirror and strips are not collimated. This is due to the fact that these have non-optimal periodicities, compared to the design we introduce (Figure 4-1). The emission pattern (Figure 4-5b) of the design with parameters shown in Figure 4-1 is the strongest and most collimated of the three patterns.

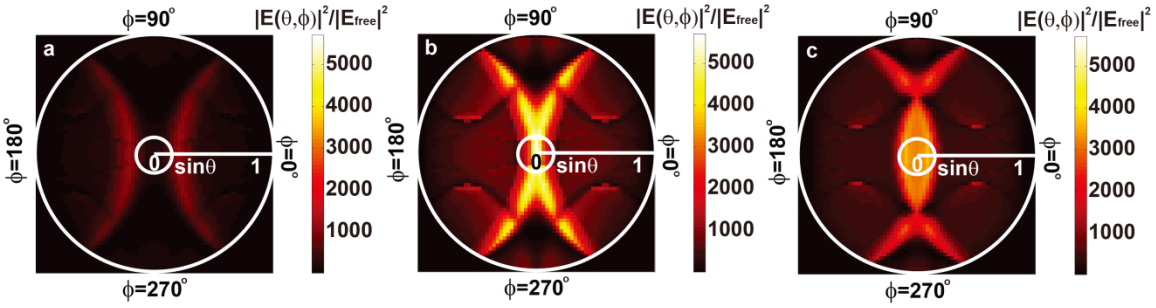

Figure 4-5. Simulated emission patterns of Raman dipole oriented in *x* direction and placed within gap of OA in three different configurations. Free space wavelength of λ=857.1 nm is employed, corresponding to 1072 cm^{-1} Raman line with λ=785 nm excitation. In all cases, the thicknesses of SiO_2 spacer are all 50 nm. (a) Array of OAs above gold mirror with gold strips. The periodicities in the *x* and *y* directions are both 630 nm. (b) Array of OAs above gold mirror with gold strips. The periodicities in the *x* and *y* directions are both 730 nm. (c) Array of OAs above gold mirror with gold strips. The periodicities in the *x* and *y* directions are both 830 nm. All the emission patterns are for the upper half space. Inner and outer circles represent angles θ such that sinθ takes values of 0.15 and 1.0, respectively.

It is seen from Figure 4-4 and Figure 4-5 that far-field emissions are either not as strong as that of the optimized structure and/or not as collimated when parameters different from those shown in Figure 4-1 are applied. The far-field emission pattern for 416 cm^{-1} Raman line is also simulated. In Figure 4-6**,** the emission patterns of 416 cm^{-1} Raman line for OAs on SiO_2, OAs above gold mirror and OAs integrated with gold mirror and strips are shown. The total collected Raman emission, assuming objective lens NA=0.15, is found for each configuration by integration over each inner circle. The

integration shows that in the design we introduce (Figure 4-6c), the collected power is ~5.4 times that occurring for the OAs above the gold mirror (Figure 4-6b), and ~5.8 times that of the OAs on the SiO_2 substrate (Figure 4-6c).The results confirm that our design realizes strong Raman emission in a directional manner for multiple Raman lines.

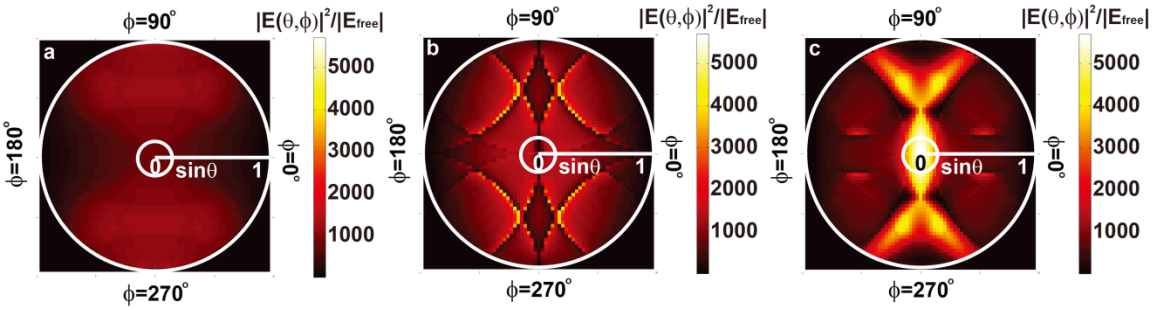

Figure 4-6. Simulated emission patterns of Raman dipole oriented in *x* direction and placed within gap of OA in three different configurations. Free space wavelength of λ=811.8 nm is employed, corresponding to 416 cm^{-1} Raman line with λ=785 nm excitation. In all cases, periodicities in the *x* and *y* directions are both 730 nm. (a) Array of OAs on an SiO_2 substrate. (b) Array of OAs above gold mirror with SiO_2 spacer. (c) Array of OAs above gold mirror with gold strips. All the emission patterns are for the upper half space. Inner and outer circles represent angles θ such that sinθ takes values of 0.15 and 1.0, respectively.

The emission patterns of Raman molecules at positions away from the center of the OAs are also shown in Figure 4-7. It can be seen that weaker emission occurs than when the molecule is in the OA center. This can be understood by considering that the emission process is reciprocal to the excitation process. In the excitation process, smaller field enhancement occurs at positions that are away from the center of OAs. In the emission process, weaker emission also occurs at these positions. In the Figure 4-7, it is seen that the emission patterns of molecules away from the center are similar to the emission pattern occurring with a molecule in the OA center. This verifies that our design collimates the Raman emission of molecules at different positions.

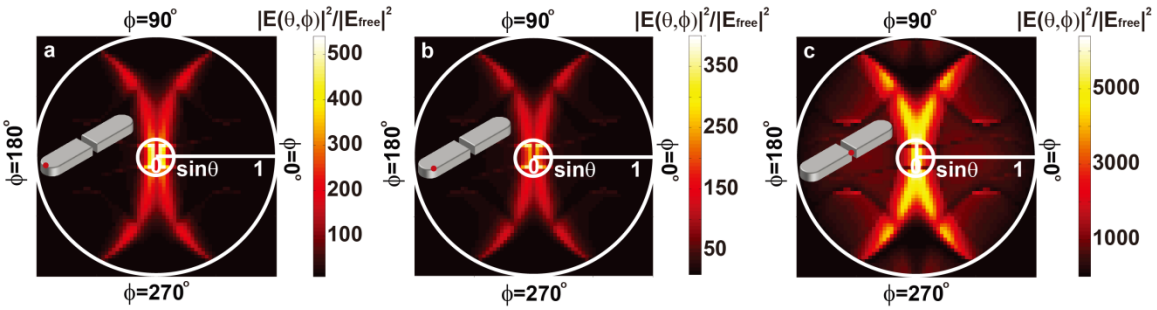

Figure 4-7. Simulated emission patterns of Raman dipole oriented in *x* direction and placed at different positions of OA integated with gold mirror and strips. Red dots indicate the postions of Raman dipole. Free space wavelength of λ=857.1 nm is employed, corresponding to 1072 cm^{-1} Raman line with λ=785 nm excitation. In all cases, periodicies in the *x* and *y* directions are both 730 nm. (a) Raman dipole is 30 nm above the top surface of SiO_2 and 85 nm away from the gold rod's flat edge along the antenna axis. (b) Raman dipole is 30 nm above the top surface of SiO_2, 55 nm away from the flat edge in the *x* direction and 30 nm away from the antenna axis in the *y* direction. (c) Raman dipole is on the flat edge and 30 nm above the top surface of SiO_2. It is 30 nm away from the antenna axis along the *y* direction. All the emission patterns are for the upper half space. Inner and outer circles represent angles θ such that sinθ takes values of 0.15 and 1.0, respectively.

Taking the enhancement of the excitation, the emitted power, and the directionality of the emission into account, we expect that the design we introduce (Figure 4-1) should produce SERS enhancement factors approximately two orders of magnitude larger than those of OAs on an SiO_2 substrate (without the gold strips and gold mirror, Figure 4-2a). Compared to OAs above a gold mirror (Figure 4-2b), the SERS enhancement factors of our design should be approximately one order of magnitude larger. We next describe experiments to measure these enhancement factors experimentally.

4.3 SERS measurements

The OAs integrated with mirror and strips, OAs above mirror and OA on SiO_2 are fabricated using e-beam lithography, metal evaporation and SiO_2 deposition. The fabrication process for the device shown starts with evaporation (e-beam evaporator, Sharon Vacuum Co.) of gold onto a silicon substrate to a thickness of 120 nm with a

deposition rate of 1Å/s. The SiO_2 spacer layer is then deposited to a thickness of 50 nm by atomic layer deposition (Savannah atomic layer deposition system, Cambridge NanoTech Inc.) with a deposition rate of 1 nm/cycle. Polymethylmethacrylate (PMMA) 495A2 and 950A2 resists (MicroChem Corp.) are spun on sequentially (40 nm thick PMMA 950A2 on top of 60 nm thick PMMA 495A2) and exposed with a pattern consisting of the one dimensional array of strips (110 nm wide). The sample is developed in PMMA developer (methyl isobutyl ketone (MIBK): Isopropyl alcohol (IPA) 1:3, MicroChem Corp.) for 90 seconds and washed in IPA for 30 seconds. Next gold is evaporated (30 nm thick, E-beam evaporator, Sharon Vacuum Co.), with a titanium layer for adhesion (1 nm thick). Both metals are evaporated with a deposition rate of 1Å/s. The PMMA layers are then removed by soaking in acetone (Honeywell Burdick and Jackson). SiO_2 is then deposited by atomic layer deposition (Savannah atomic layer deposition system, Cambridge NanoTech Inc.) to a thickness of 2 nm with a deposition rate of 1 nm/cycle. This ensures that, in the SERS measurements, the benzenethiol molecules do not adsorb to the gold strips. This is advantageous because it means that the SERS signals we measure originate from the molecules on the OAs, and not from molecules on the strips. We next use a chromium spacer layer oxidation method [8] to produce OAs with gaps of ~5 nm. This method involves two electron beam lithography and liftoff steps, where each step defines one of the nanoparticles in each OA dimer. The lateral expansion of a sacrificial chromium layer enables a gap of ~5nm to be produced between nanoparticles in each OA. Further details can be found in the Ref. [8]. The overall extent of each fabricated OA array is ~100 μm × 100 μm. A zoom-in of a portion of a typical device is shown as the scanning electron microscope (SEM) image of Figure 4-8. It can

be seen that the fabrication processes yields excellent control over the size and shape of the OAs. The dimensions of the fabricated devices are close to those shown in Figure 4-1.

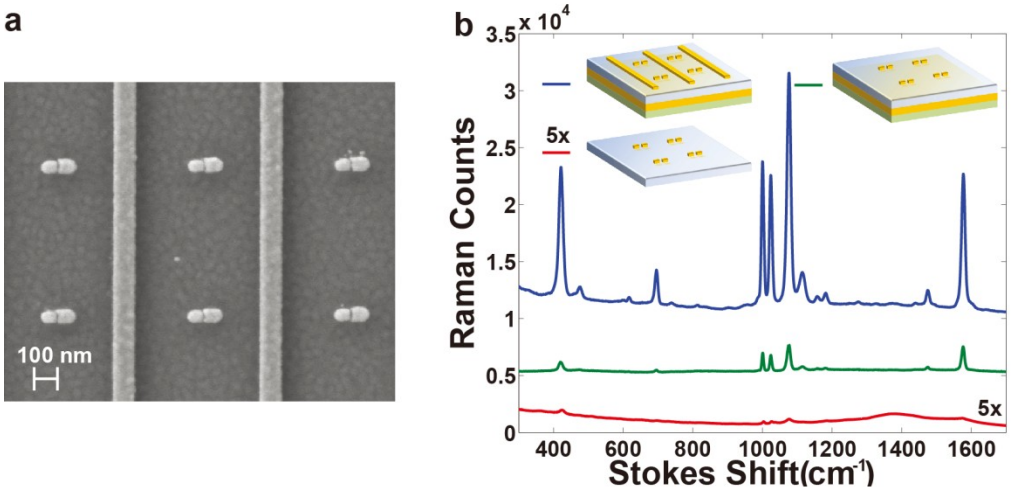

Figure 4-8. (a) SEM image of OA array with gold strips, above a gold film, with SiO_2 used as spacer layer. (b) SERS spectra measured from benzenethiol monolayers formed on OAs in three configurations: OAs on SiO_2 substrate (red curve, signals are enlarged by 5 times), OAs above gold mirror (green curve), OAs integrated with strips and mirror (blue curve). Blue and green curves are vertically offset by 10000 and 5000 counts, respectively, for display purposes.

To obtain the SERS signals, we dip the samples (OAs on SiO_2 substrate, OAs above gold mirror and OAs integrated with strips and mirror) in a solution of benzenethiol in ethanol (3×10^{-3} mol/L) for 1 hour. This results in a self-assembled monolayer of benzenethiol on the gold OA surfaces. It should also be noted that benzenethiol does not bind to silicon dioxide. After removal from the benzenethiol solution, the samples are rinsed in ethanol and blown dry with nitrogen. The benzenethiol and ethanol are used as bought from Sigma-Aldrich Co. LLC. SERS measurements are made with a Raman microscope equipped with a spectrometer and a thermoelectrically-cooled charge coupled device (CCD) detector (LabRAM, Horiba Jobin-Yvon). The excitation laser wavelength is λ=785 nm, and the power is 0.65 mW. An objective lens (NA=0.15, magnification 5×) is used to focus the excitation laser on the samples and

collect the emitted Raman signals. The signal accumulation time for the CCD detector is 5 seconds. The results of SERS measurement are shown in Figure 4-8b.

To quantify the differences between the performances of these devices, we analyze the Raman lines at 416 cm^{-1}, 1072 cm^{-1} and 1586 cm^{-1}. It can be seen that OAs integrated with strips and mirror yield largest signals among the three samples. To determine the SERS enhancement factors, measurements are made of Raman scattering from neat benzenethiol liquid sandwiched between a microscope slide and a coverslip. The benzenthiol thickness (500 μm) is defined using a spacer to separate the slide and coverslip. These measurements are performed using the same experimental parameters as the SERS measurements. The SERS enhancement factor is then given by $EF = \frac{I_{SERS} / N_{SERS}}{I_{REF} / N_{REF}}$, where I_{SERS} and I_{REF} are the signal intensities measured in the SERS and Raman experiments, respectively. These intensities are the heights of the Raman lines in the spectra with the background subtracted. N_{SERS} and N_{REF} are the numbers of molecules in the SERS and Raman experiments, respectively. N_{SERS} is given by the area of the exposed gold surfaces of the OAs multiplied by the packing density of benzenethiol (6.8×10^{14} cm^{-2} [25]). N_{REF} is given by the confocal collection volume of the microscope multiplied by the density of neat benzenethiol (9.6 mol/L). The collection volume is found by measuring the Raman signal from a silicon wafer as a function of its position along the optical axis [14]. The enhancement factor calculated here is the average factor by which the Raman signals from the molecules on the OAs are increased, compared to the molecules in pure benzenethiol. It should be noted that substantially larger enhancement factor values would result, were we to make the assumption that is

sometimes made that the SERS signal originates from only those molecules within the hot spot in the gap, since the assumed number of molecules contributing to SERS signals would be far smaller [26].

The average experimentally-determined SERS enhancement factors of 416 cm^{-1}, 1072 cm^{-1} and 1586 cm^{-1} Raman lines for the device we introduce (blue curve, Figure 4-8b) are 1.1×10^{10}, 8.5×10^{9}, and 1.2×10^{10}, respectively. By contrast, for the same Raman lines, the OAs above the mirror (green curve, Figure 4-8b) exhibit measured average enhancement factors of 6×10^{8}, 7.1×10^{8} and 1.5×10^{9}. The device we introduce (blue curve, Figure 4-8b), therefore, has enhancement factors that are 19, 12, and 8 times larger than that for OAs above mirror (green curve, Figure 4-8b) for those Raman lines. For the OAs on the SiO_2 substrate (red curve, Figure 4-8b), the measured enhancement factors are 9.5×10^{7}, $5.4\times10^{7}$and 6×10^{7} for those Raman lines. Adding the gold mirror and gold strips to an OA array, therefore, improves the enhancement factors of the 416 cm^{-1}, 1072 cm^{-1} and 1586 cm^{-1} Raman lines by 120, 156 and 200 times, respectively. The two orders of magnitude boost in enhancement factor results from the improvements in local field enhancement, total emission enhancement and Raman collection efficiency enhancement that result from adding the strips and mirror to the OAs. As shown in the literature [27], the peak value of the SERS enhancement factor in the hot spots can be two orders of magnitude larger than the average value. This suggests that the peak SERS enhancement factor for our design could be as high as 1×10^{12}. Experiments would be necessary to validate this, but it nonetheless suggests that our device could be a platform for highly reproducible single molecule detection.

4.4 Conclusions

In this Chapter, we have shown that adding gold strips and a gold mirror to an OA array results in a substantial boost, of two orders in magnitude, to the SERS enhancement factor, yielding values up to 1.2×10^{10}. These represent average values of enhancement; the peak values experienced by molecules in the hot spots are likely to be substantially higher. Electromagnetics simulations revealed the importance of both local field enhancement and directivity enhancement in achieving this level of performance. We anticipate that explicit consideration of both phenomena will be a fruitful path in the design of SERS substrates.

4.5 References

[1]. M. Fleischmann, P. J. Hendra, and A. J. McQuillan, "Raman spectra of pyridine adsorbed at a silver electrode," Chemical Physics Letters **26**, 163-166 (1974).
[2]. S. Nie, and S. R. Emory, "Probing Single Molecules and Single Nanoparticles by Surface-Enhanced Raman Scattering," Science **275**, 1102-1106 (1997).
[3]. K. Kneipp, Y. Wang, H. Kneipp, L. T. Perelman, I. Itzkan, R. R. Dasari, and M. S. Feld, "Single Molecule Detection Using Surface-Enhanced Raman Scattering (SERS)," Physical Review Letters **78**, 1667-1670 (1997).
[4]. C. L. Haynes, A. D. McFarland, L. Zhao, R. P. Van Duyne, G. C. Schatz, L. Gunnarsson, J. Prikulis, B. Kasemo, and M. Käll, "Nanoparticle Optics: The Importance of Radiative Dipole Coupling in Two-Dimensional Nanoparticle Arrays†," The Journal of Physical Chemistry B **107**, 7337-7342 (2003).
[5]. K. A. Willets, and R. P. Van Duyne, "Localized Surface Plasmon Resonance Spectroscopy and Sensing," Annual Review of Physical Chemistry **58**, 267-297 (2007).
[6]. K. Li, L. Clime, L. Tay, B. Cui, M. Geissler, and T. Veres, "Multiple Surface Plasmon Resonances and Near-Infrared Field Enhancement of Gold Nanowells," Analytical Chemistry **80**, 4945-4950 (2008).
[7]. J. Wessel, "Surface-enhanced optical microscopy," J. Opt. Soc. Am. B **2**, 1538-1541 (1985).
[8]. W. Zhu, M. G. Banaee, D. Wang, Y. Chu, and K. B. Crozier, "Lithographically Fabricated Optical Antennas with Gaps Well Below 10 nm," Small **7**, 1761-1766 (2011).
[9]. K. B. Crozier, A. Sundaramurthy, G. S. Kino, and C. F. Quate, "Optical antennas: Resonators for local field enhancement," Journal of Applied Physics **94**, 4632-4642 (2003).
[10]. E. Cubukcu, E. A. Kort, K. B. Crozier, and F. Capasso, "Plasmonic laser

antenna," Applied Physics Letters **89**, 093120-093123 (2006).
[11]. N. Yu, E. Cubukcu, L. Diehl, M. A. Belkin, K. B. Crozier, F. Capasso, D. Bour, S. Corzine, and G. Hofler, "Plasmonic quantum cascade laser antenna," Applied Physics Letters **91**, 173113-173113 (2007).
[12]. P. J. Schuck, D. P. Fromm, A. Sundaramurthy, G. S. Kino, and W. E. Moerner, "Improving the Mismatch between Light and Nanoscale Objects with Gold Bowtie Nanoantennas," Physical Review Letters **94**, 017402 (2005).
[13]. D. Wang, T. Yang, and K. B. Crozier, "Charge and current reservoirs for electric and magnetic field enhancement," Opt. Express **18**, 10388-10394 (2010).
[14]. Y. Chu, M. G. Banaee, and K. B. Crozier, "Double-Resonance Plasmon Substrates for Surface-Enhanced Raman Scattering with Enhancement at Excitation and Stokes Frequencies," ACS Nano **4**, 2804-2810 (2010).
[15]. Y. Chu, D. Wang, W. Zhu, and K. B. Crozier, "Double resonance surface enhanced Raman scattering substrates: an intuitive coupled oscillator model," Opt. Express **19**, 14919-14928 (2011).
[16]. M. G. Banaee, and K. B. Crozier, "Mixed Dimer Double-Resonance Substrates for Surface-Enhanced Raman Spectroscopy," ACS Nano **5**, 307-314 (2010).
[17]. J. Li, D. Fattal, and Z. Li, "Plasmonic optical antennas on dielectric gratings with high field enhancement for surface enhanced Raman spectroscopy," Applied Physics Letters **94**, 263114-263113 (2009).
[18]. T. J. Seok, A. Jamshidi, M. Kim, S. Dhuey, A. Lakhani, H. Choo, P. J. Schuck, S. Cabrini, A. M. Schwartzberg, J. Bokor, E. Yablonovitch, and M. C. Wu, "Radiation Engineering of Optical Antennas for Maximum Field Enhancement," Nano Letters **11**, 2606-2610 (2011).
[19]. D. Wang, T. Yang, and K. B. Crozier, "Optical antennas integrated with concentric ring gratings: electric field enhancement and directional radiation," Opt. Express **19**, 2148-2157 (2011).
[20]. A. Ahmed, and R. Gordon, "Directivity Enhanced Raman Spectroscopy Using Nanoantennas," Nano Letters **11**, 1800-1803 (2011).
[21]. B. Liu, D. Wang, C. Shi, K. B. Crozier, and T. Yang, "Vertical optical antennas integrated with spiral ring gratings for large local electric field enhancement and directional radiation," Opt. Express **19**, 10049-10056 (2011).
[22]. E. C. Le Ru, and P. G. Etchegoin, "Rigorous justification of the |E|4 enhancement factor in Surface Enhanced Raman Spectroscopy," Chemical Physics Letters **423**, 63-66 (2006).
[23]. Y. Chu, W. Zhu, D. Wang, and K. B. Crozier, "Beamed Raman: directional excitation and emission enhancement in a plasmonic crystal double resonance SERS substrate," Opt. Express **19**, 20054-20068 (2011).
[24]. E. M. Purcell, "Spontaneous Emission Probabilities at Radio Frequencies " Physical Review **69**, 681 (1946).
[25]. A. D. McFarland, M. A. Young, J. A. Dieringer, and R. P. Van Duyne, "Wavelength-Scanned Surface-Enhanced Raman Excitation Spectroscopy," The Journal of Physical Chemistry B **109**, 11279-11285 (2005).
[26]. H. Im, K. C. Bantz, N. C. Lindquist, C. L. Haynes, and S.-H. Oh, "Vertically Oriented Sub-10-nm Plasmonic Nanogap Arrays," Nano Letters **10**, 2231-2236 (2010).
[27]. E. C. Le Ru, P. G. Etchegoin, and M. Meyer, "Enhancement factor distribution

around a single surface-enhanced Raman scattering hot spot and its relation to single molecule detection," The Journal of Chemical Physics **125**, 204701-204713 (2006).

5 Directional Raman scattering from single molecules in the feed gaps of optical antennas

5.1 Introduction

Controlling light from single emitters is an overarching theme of nano-optics [1, 2]. Antennas are routinely used to modify the angular emission patterns of radio wave sources. “Optical antennas” [3-5] translate these principles to visible and infrared wavelengths, and have been recently used to modify fluorescence from single quantum dots [6] and single molecules [7, 8]. Understanding the properties of single molecules, however, would be advanced were one able to observe their vibrational spectra through Raman scattering in a very reproducible manner, but is a hugely challenging task, as Raman scattering cross sections are very weak [9]. The drawback of Raman scattering cross sections being weak is mitigated using the enhanced fields around nanostructures in the method known as surface-enhanced Raman scattering (SERS) [10-12]. Reports of single molecule SERS (SMSERS) [13, 14] generated considerable interest but, with one notable exception [15], those that followed [16-22] have left largely unchanged the method to produce the SMSERS-active substrates, the salt-induced aggregation of Ag nanoparticles. The aggregates that result are extremely heterogeneous and generally fewer than 1% are SMSERS-active [23]. The lack of reproducible substrates has hindered scientific and technological applications of SMSERS, and the realization of a controllable means for SMSERS is needed. Ahmed and Gordon [15] fabricated a single optical

antenna, and reported SMSERS based on the bi-analyte technique with Rhodamine 6G and Nile Blue dyes. In this chapter, we demonstrate SMSERS from an optical antenna chip containing more than a thousand optical antennas. Because of the large number of antennas, statistical analysis is possible, and shows that the fraction of antennas having single molecule sensitivity is near unity. That the antennas are SMSERS-active is proven using two isotopologues of the same molecule at a concentration that is three orders of magnitude lower than that of Ref. [15]. We furthermore directly measure the angular emission profiles of SERS at the single molecule level, showing that directional emission is achieved.

5.2 Design of optical antenna

The SMSERS chip we introduce consists of a square array of optical antennas. Figure 5-1a depicts a portion of the array schematically. Each optical antenna consists of a pair of silver particles surrounded by a silver ring, all on a SiO_2 spacer layer on a silver mirror. The silver particles are separated by a gap of only ~5 nm. As a consequence, very strong field enhancement results upon illumination of the chip with a wave polarized across the gap (Figure 5-1b). This leads to strong excitation of Raman scattering from molecules located in the gap.

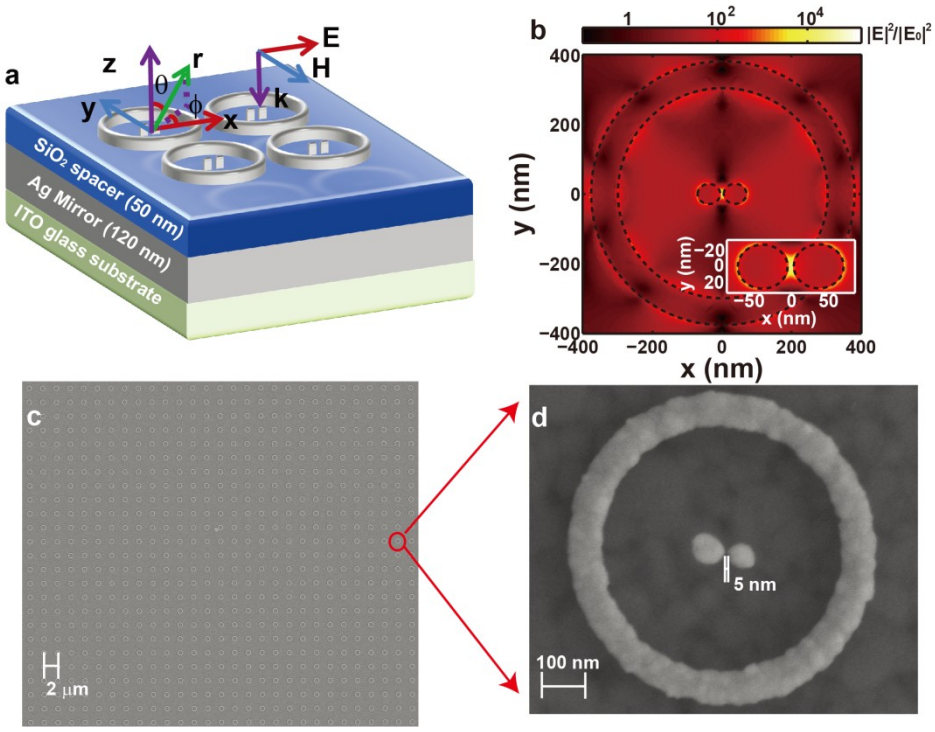

Figure 5-1. (a) Schematic of optical antenna chip for SMSERS. Each antenna consists of pair of Ag particles (5 nm gap) surrounded by an Ag ring, all on an SiO_2 spacer layer on an Ag mirror on ITO-coated glass. Ag rings have inner & outer radii of 300 nm & 380 nm, respectively. Ag particles & rings are 40 nm thick (in z-direction). Ag particles are rods (70 nm long & 60 nm wide in *x*- & *y*-directions) with rounded ends (30 nm radius). Periodicities of the antennas in *x* and *y* directions are both 2 μm. (b) Profile of the simulated intensities of electric field at the wavelength of λ=532 nm on *xy* plane and 20 nm above the top surface of SiO_2 spacer. Intensities of electric field are normalized by that of the incident wave. Polarization and propagation direction of incident wave are given in Fig. 1a. Dashed lines indicate outlines of silver ring and particle pair. Inset: intensities of electric field around particle pair. (c) and (d) Scanning electron microscope images of optical antenna chip. Overall extent of optical antenna array is 100 μm × 100 μm. Inner and outer radii of silver rings are 300 nm and 380 nm, respectively. Left-hand rod of optical antenna is 80 nm long and 70 nm wide. Right-hand rod of optical antenna is 68 nm long and 62 nm wide.

The chip is made using top-down fabrication methods that yield excellent control of the characteristics and positions of the hot spots. Device fabrication starts with a glass substrate coated with a layer of indium tin oxide (ITO). Silver is deposited to a thickness of 120 nm by electron beam evaporation. The spacer is then produced by sputtering SiO_2 to a thickness of 50 nm. Polymethylmethacrylate (PMMA) 495 and PMMA 950 are then

spun on to thicknesses of 200 nm and 100 nm, respectively. Electron beam lithography is then performed, but only the right-hand rod of each antenna is exposed. Following development, silver is evaporated to a thickness of 40 nm, and lift-off performed. PMMA layers are then again spun on, and electron beam lithography performed. This time, an alignment step is performed, and the left-hand rod of each antenna and the rings are exposed. Silver is evaporated and lift-off is performed. The error in aligning the second electron beam lithography step to the first is ±10 nm. To achieve an array of antennas with nanometer-scale gaps, we therefore need to make several devices. We find that, roughly speaking, in one out of six antenna arrays, an alignment accuracy similar to that of Figure 5-1 is achieved. We find that in such devices, the antenna gap sizes vary little across the array. No gap fusion within the antenna array shown in Figure 5-1 is observed. The fabrication method here is different from our previous method [24] for producing nanoscale gaps, in which the lateral oxidation of a Cr layer was employed. SEM images of the chip are shown as Figure 5-1c and Figure 5-1d. It can be seen that the dimensions of the rings, gaps and right part of optical antennas of the fabricated device match those of Figure 5-1a, but that the left-hand rod of each antenna is slightly longer than the right-hand rod. To see what effect this mismatch has, we simulate the intensity enhancement of the optical antenna with parameters shown in Figure 5-1d using the finite element method (FEM). The dielectric permittivity of silver is taken from Ref. [25]. Plane wave illumination from the air side at normal incidence is used at a free space wavelength of λ = 532 nm. The results are shown in Figure 5-2. It can be seen that the field enhancement (1.45×10^5) in the feed gap of optical antenna in Figure 5-2 is very similar to that of Figure 5-1b, differing by <7%.

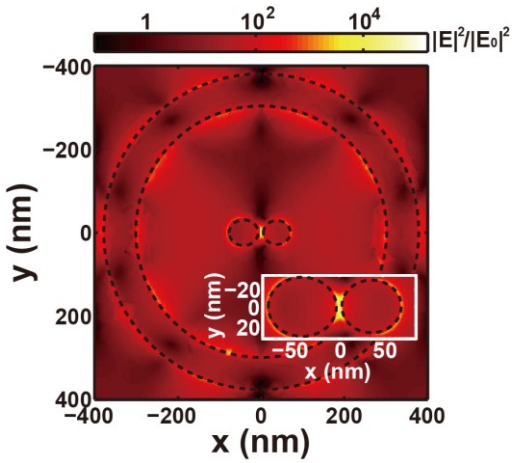

Figure 5-2. Simulated electric field intensity (<|E|^2>) on *xy* plane (20 nm above SiO_2 surface) in response to x-polarized plane wave illumination from air side at normal incidence (Figure 5-1a). Intensities are normalized by intensity of illuminating plane wave. Simulations are performed at a wavelength of λ=532 nm.

The silver mirror, SiO_2 spacer and silver rings in our device are favorable for excitation enhancement, for Raman emission enhancement and for efficient collection. The silver mirror supports image dipoles that couple with the localized surface plasmons excited on the nanoparticle pairs [26, 27]. The silver ring excites surface plasmon polaritons on the mirror that converge to the ring center [28], leading to stronger excitation of the particle pairs. To compare the excitation enhancement provided by our optical antenna chip to that of basic optical antennas on SiO_2 (e. g. no rings and mirrors), we simulate the intensity enhancement of each. The simulated structures have dimensions as given in Figure 5-1. The results are shown as Figure 5-3. It can be seen that the optical antenna incorporating the ring and mirror provides considerably stronger intensity enhancement, with the peak value (1.36×10^5 in the feed gap)

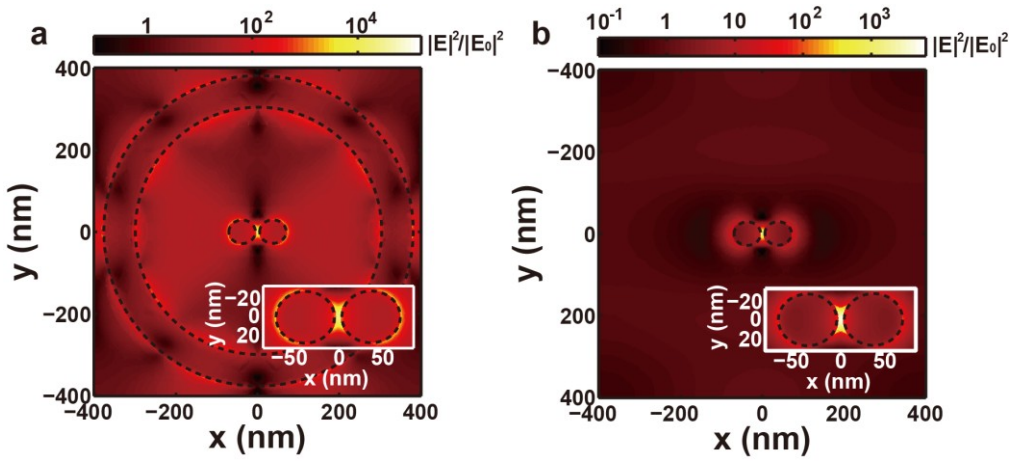

Figure 5-3. Simulated electric field intensity ($<|E|^2>$) on *xy* plane (20 nm above SiO_2 surface) in response to x-polarized plane wave illumination from air side at normal incidence (Figure 5-1a). Intensities are normalized by intensity of illuminating plane wave. Simulations are performed at a wavelength of λ=532 nm. (a) Optical antenna integrated with silver ring and mirror. (b) Basic optical antenna on SiO_2.

Compared with the electric field intensity (6.4×10^3) in the middle of the gap of a the basic optical antenna on SiO_2, the electric field intensity (1.36×10^5) in the middle of the gap of our design in Figure 5-3a is ~21 times larger. The simulation results (not shown here) predict that the electric field intensity (4.5×10^4) in the middle of the gap of an optical antenna, without the silver ring but above a silver mirror, is ~7 times larger than that in the middle of gap of a basic optical antenna. This indicates that the silver mirror and silver ring improve electric field intensity enhancement by ~7 times and ~3 times, respectively. We also simulate a single optical antenna over silver mirror with the same parameters shown in Figure 5-1. This antenna is isolated, i.e. there are no neighboring antennas. The results (not shown here) indicate that the electric field intensity (1.29×10^5) in the middle of the gap of the single antenna is close to that (1.36×10^5) in the middle of the gap of the antenna shown in Figure 5-1 where the neighboring antennas are taken into account. The small variation (6%) indicates that the interaction between the antennas is not strong in this design. In our design, the thickness of the SiO_2

spacer layer [26, 27] and the silver ring dimensions [28] are chosen to achieve optimal local field enhancement.

5.3 Directional far-field radiation patterns

Similar to the findings of previous studies [28, 29], the silver mirror and rings in the chip also collimate the Raman emission, increasing collection efficiency. To quantify the Raman emission process, the Raman molecules are modeled as dipoles oriented in the *x* direction. Figure 5-4a and Figure 5-4b, the simulated far-field power radiation patterns that result when a dipole is placed in the middle of the gap of the optical antenna we introduce (red curves) and in the middle of the gap of a basic optical antenna (blue curve) are shown. In both cases, the dipole is positioned 20 nm above the top surface of the SiO_2 layer.

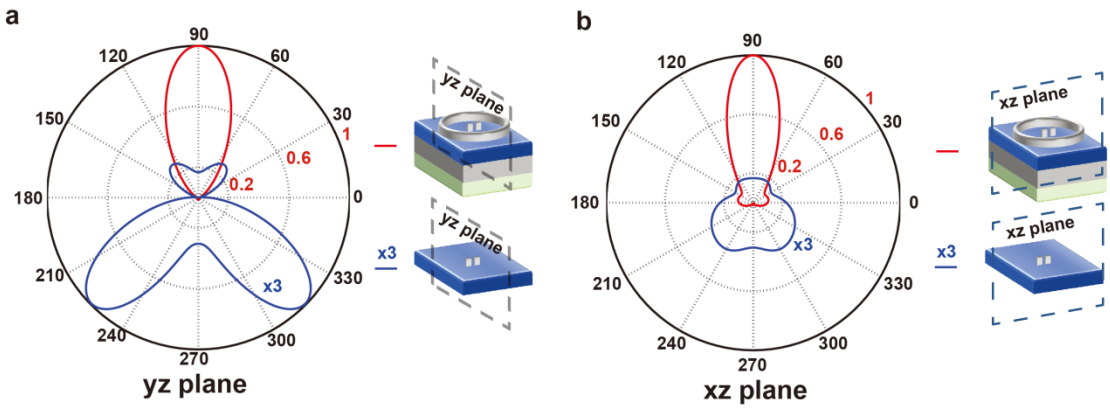

Figure 5-4. Calculated far-field radiation power intensity patterns for device we introduce (red curves) and basic optical antenna design (blue curves). Simulations performed at a wavelength of λ=550.2 nm (620 cm^{-1} Raman line with excitation at λ=532 nm). The radiation power patterns are normalized by the peak power radiated by the optical antenna design we introduce. For comparison purposes, the results for the basic optical antennas (blue curves) have been multiplied by 3×. (a) Calculated radiation patterns on *yz* plane. (b) Calculated radiation patterns on *xz* plane.

It can be seen that, with the proposed device, the emission is directional and largely

normal to the substrate, meaning that its collection efficiency is higher than that of the basic optical antenna, for which much of the emission occurs into the SiO_2. To compare the performance of our design with that of a basic optical antenna, we calculate the full three dimensional far-field power radiation patterns. The results shown in Figure 5-5 predict that, with the antenna chip, the Raman signal collected by a lens (NA = 0.9) is ~7 times larger than would be collected by the lens were the basic antenna used. We also simulate an optical antenna without the silver ring but with the silver mirror (results not shown here). These simulations show that the Raman signal collected by the lens for this device is ~2.5 times larger than the signal that would be collected were the basic antenna used. Therefore, the silver mirror and silver ring contribute to the collimation of Raman emission, and boost collected Raman signals by 2.5 times and 2.8 times, respectively.

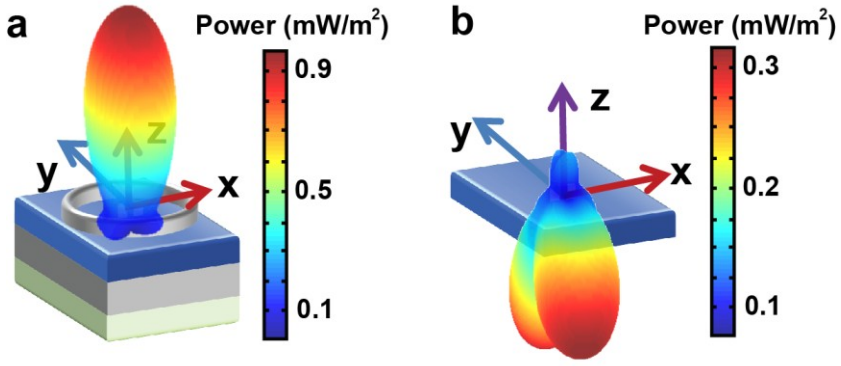

Figure 5-5. Calculated 3D far-field radiated power patterns at a wavelength of λ=550.2 nm (620 cm^{-1} Raman line). (a) Radiation pattern of optical antenna integrated with silver ring (silver color) and SiO_2 mirror (blue) (b) Radiation pattern of basic optical antenna on SiO_2.

With both the excitation and emission enhancements considered, the modeling therefore predicts SERS enhancements for the proposed design that are ~two orders of magnitude larger than those achieved with the basic antenna. The larger enhancement makes our chip a good candidate for SMSERS.

5.4 Single Molecule SERS (SMSERS)

We verify that our chip achieves SMSERS using the isotopologue method [16, 18, 19]. As noted by Dieringer et al [16], the isotopologue method has a number of advantages over the bi-analyte approach with different molecules. For the latter, the proper interpretation of results requires knowledge of the differences in Raman cross sections, absorption spectra and surface binding affinities of the different molecules. For the isotopologue approach, on the other hand, the molecules differ only in the isotopic composition of their atoms. They can therefore be distinguished by their SERS spectra, but their overall Raman cross sections, absorption spectra and surface binding affinities are identical. As we describe in further detail below, we introduce two forms of Rhodamine 6G (d0 and d4) to the chip at a low concentration, scan the chip, and measure SERS from more than a thousand antennas. That the SERS spectrum from each antenna corresponds chiefly to only one isotopologue (and not both) confirms that SMSERS is achieved. The isotopologues are synthesized and characterized using the methods described in previous studies [20, 30]. The electronic absorption of the Rhodamine 6G is on resonance with our laser (λ=532 nm), increasing the Raman signal [16]. One should therefore refer to this method as single-molecule surface-enhanced resonant Raman spectroscopy (SMSERRS). For brevity, however, we follow the convention of Ref. [16] and refer to it as SMSERS.

The confirmation of SMSERS makes use of the fact that the isotopologues can be readily distinguished by the Raman line that appears at 620 cm^{-1} and 610 cm^{-1} for R6G-d0 and R6G-d4, respectively. The fabricated optical antenna chip is soaked in a solution containing the isotopologues (0.2 nM each) for 12 hours, washed in methanol, then blown

dry with nitrogen. The optical antenna chip is then scanned in a Raman microscope (Horiba Jobin Yvon, LabRam), with a step size of 1 μm. In the microscope, a laser beam (λ = 532 nm) is focused onto the chip with a microscope objective (magnification 100×, numerical aperture NA 0.9). The laser power incident on the chip is 0.03 mW. The same objective lens is used to collect the Raman signal into a spectrometer equipped with a thermoelectrically cooled charge coupled device (CCD) sensor. The integration time used to acquire the Raman spectrum at each scan position is 0.5 seconds. An 80 × 80 μm region of the chip containing 1681 optical antennas is scanned. A SERS spectrum is measured at each scan position. Among the data obtained, 1120 antennas yield strong Raman signals for the 620 cm^{-1} and/or 610 cm^{-1} Raman lines. These 1120 events can therefore be divided into three categories: the spectrum is that of R6G-d0, the spectrum is that of R6G-d4, and the spectrum contains both R6G-d0 and R6G-d4 features. In Figure 5-6a, these events are tabulated in a histogram.

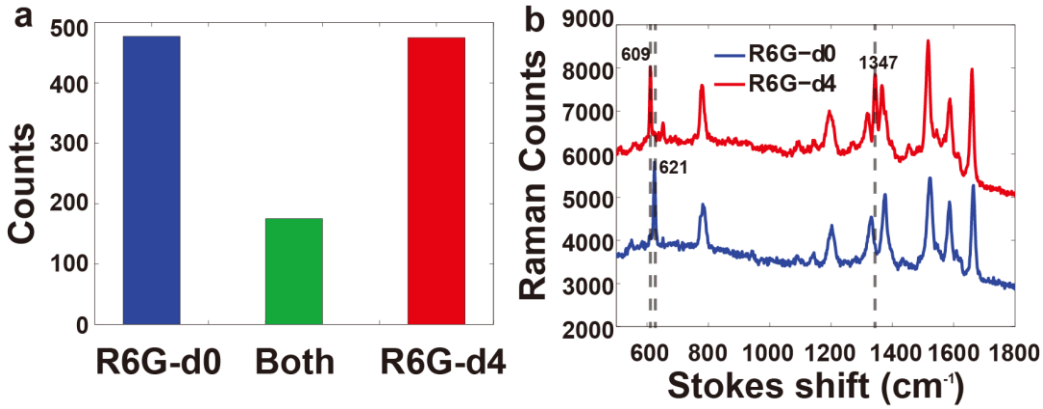

Figure 5-6. Experimental results of SMSERS using the optical antenna chip we introduce. (a) Histogram of single molecule level events: R6G-d0 molecule (blue), both R6G-d0 and R6G-d4 molecules (green), and R6G-d4 molecule (red). (b) Representative Raman spectra of R6G-d0 and R6G-d4 single molecule level events. The R6G-d4 spectrum is shifted in the vertical direction by 2000 counts for display purposes.

It can be seen that a significant number of events (945 out of 1,120 (84%))

demonstrate Raman spectra containing either R6G-d0 or R6G-d4, but not both. As discussed in Ref. [16], the number of molecules within each hot spot follows a Poisson distribution and the probability of observing each isotopologue follows a Binomial distribution. The overall probability is thus the product of the two distributions, and is given as follows (Equation 1 of Ref. [16]):

$$P(n_4, n_0, \alpha) = \frac{e^{-\alpha}\alpha^{(n_4+n_0)}}{(n_4+n_0)!} \times \frac{(n_4+n_0)!}{n_4!\,n_0!}\left(\frac{1}{2}\right)^{(n_4+n_0)} \qquad (5.1)$$

Here, n_0 and n_4 are the numbers of R6G-d0 and R6G-d4 molecules within the hot spots, respectively. α is the average number of molecules within each hot spot. The Poisson-binomial model predicts that 1,120 (of the 1,681) antennas would have one of more molecules in their hot spots, and therefore produce SERS signals, if there were on average 1.097 molecules per hot spot. The measured relative frequencies of the R6G-d0-only, mixed, and R6G-d4-only events are 475:175:470, i.e. a ratio of ~2.7:1:2.7. This confirms that our device achieves SMSERS. Using the Poisson-binomial model, and following the assumption of Ref. [16] that the competition between multiple molecules for the hot spots leads to there being two or fewer molecules per hot spot, a ratio of ~2.3:1:2.3 would result, were there on average 1.097 molecules per hot spot. That the modeled values are close to the experimental values confirms the very high, i.e. near unity, fraction of the optical antennas with SMSERS sensitivity. Differences between the modeled and experimental results could be due to the competition between multiple molecules for the hot spots being even more pronounced than that assumed above, further skewing the distribution and making it deviate from Poisson-binomial behavior. In Figure 5-5b, representative Raman spectra are shown for R6G-d0 and R6G-d4 single molecule events. The Raman peaks in Figure 5-6b shift slightly from their average values measured

from large numbers of molecules. Such peak shifts have also been observed in previous SMSERS studies [16, 18]. They represent further confirmation that SMSERS is achieved.

The Raman intensities of R6G-d0 and R6G-d4 events are shown in a histogram (Figure 5-7). It can be seen that the distributions of Raman intensities of R6G-d0 and R6G-d4 events are very similar. This is to be expected as the R6G-d0 and R6G-d4 molecules have identical binding properties. The variation in Raman signal intensity is likely to be due to the fact that the molecules adsorb to the chip at random locations, and therefore experience very different values of local field enhancement. Because the variation of Raman signals of R6G-d0 events and R6G-d4 events is large, we cannot determine the number of molecules in a given event by intensity.

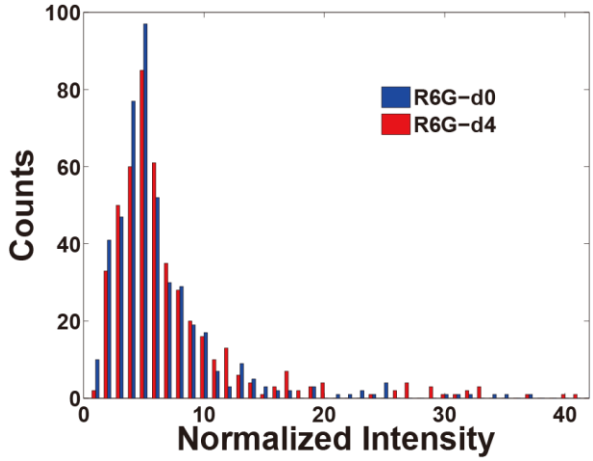

Figure 5-7. Histogram of intensities of Raman signal of R6G-d0 events and R6G-d4 events. Intensities of R6G-d0 events (620 cm^{-1} Raman line, blue bars) and R6G-d4 events (610 cm^{-1} Raman line, red bars) are each normalized by their minimum values.

5.5 Far-field radiation patterns of SMSERS

A central question in the field of nano-optics is whether an antenna can be used to modify the angular distribution of light from a single quantum emitter [31]. Here we show directional emission of Raman from single molecules. We fabricate an optical antenna chip, and soak it in the R6G-d0/R6G-d4 isotopologue solution (0.5 nM of each).

The SEM image of fabricated chip (not shown here) reveals that the optical antennas have gap widths of 15 nm, slightly larger than those of the antennas used in the experiments of Figure 5-7. Simulations of the far-field radiation pattern of the antennas with 15 nm gap are found to be very similar to those with 5 nm gaps (Figure 5-4), however. The measured ratio of 2.3:1:2.3 for R6G-d0-only, mixed, and R6G-d4-only confirms that the SMSERS regime is achieved.

We build a system that enables the angular distribution of emission of each Raman line to be measured at the back-focal-plane of the microscope objective. The Raman-scattered light at the back focal plane of the collection microscope objective lens represents the angular emission pattern of the Raman scattering from R6G molecules. To measure this, we employ the home-built energy momentum spectroscopy [32] setup shown as Figure 5-8a. A collimated continuous-wave laser with a wavelength of 532 nm and a power of 0.45 mW is focused by an objective lens (NA = 0.9) onto the sample. Raman scattering from single R6G molecules is collected by the same objective lens. A 532 nm long-pass filter is placed in the optical path to block the Rayleigh scattered light. Placed after the tube lens, a convex lens (100 mm focal length) acts as a Bertrand lens, creating a first image plane of the objective lens back-focal-plane. A slit, whose position can be scanned, is placed at this back-focal-plane image plane. Another convex lens with focal length of 50 mm creates a second image plane, with a demagnification factor of 3.2 times compared to the first image plane. This enables the image to be commensurate with the size of the CCD in the spectrometer. To reconstruct that emission pattern that originates from a R6G molecule, the scanning slit is closed down to 200 μm to select one vertical portion (column) of the back-focal-plane image. Each pixel in this column is then

dispersed horizontally by the spectrometer's grating onto its CCD. In this way, the spectrum corresponding to each pixel of the column can be found. This procedure is repeated for different horizontal positions of the slit, enabling the 2D SERS emission pattern to be found as a function of wavelength.

The measured far-field emission patterns of the 620 cm^{-1} Raman line of a single R6G-d0 molecule level event and of the 610 cm^{-1} Raman line of a single R6G-d4 molecule level event are shown as Figure 5-8b and Figure 5-8c, respectively. It can be seen that on both cases, the SERS emission is mostly contained in a small range of angles about the $+z$ direction. The emission pattern of Figure 5-8b has full-widths-at-half-maximum (FWHMs) of 41 and 49 degrees in the *xz* and *yz* planes, respectively. These represent substantial directionality, and are close to the predicted values of 40 and 48 degrees for the *xz* and *yz* planes, respectively (Figure 5-4). By comparison, the power radiated by a dipole in free space, oriented in the x-direction, has a $\cos^2\theta$ dependence. Such a dipole would therefore have FWHMs of 90 and 360 degrees in the *xz* and *yz* planes, respectively. The experimental results demonstrate the dramatic modification to the direction of Raman emission from single molecules that occurs when they are placed in the feed gaps of optical antennas surrounded by silver nano rings and above a mirror.

The SERS spectrum is measured by removing the Bertrand lens. In this configuration, tube lens creates a sample image plane at the scanning slit and also at the entrance of spectrometer. The measured Raman spectra shown in Figure 5-8d are measured on the same single molecule level events whose emission patterns are shown as Figure 5-8b and Figure 5-8c. As before, the positions of the Raman lines are used to determine whether the single molecule level events originate from R6G-d0 or from R6G-

d4.

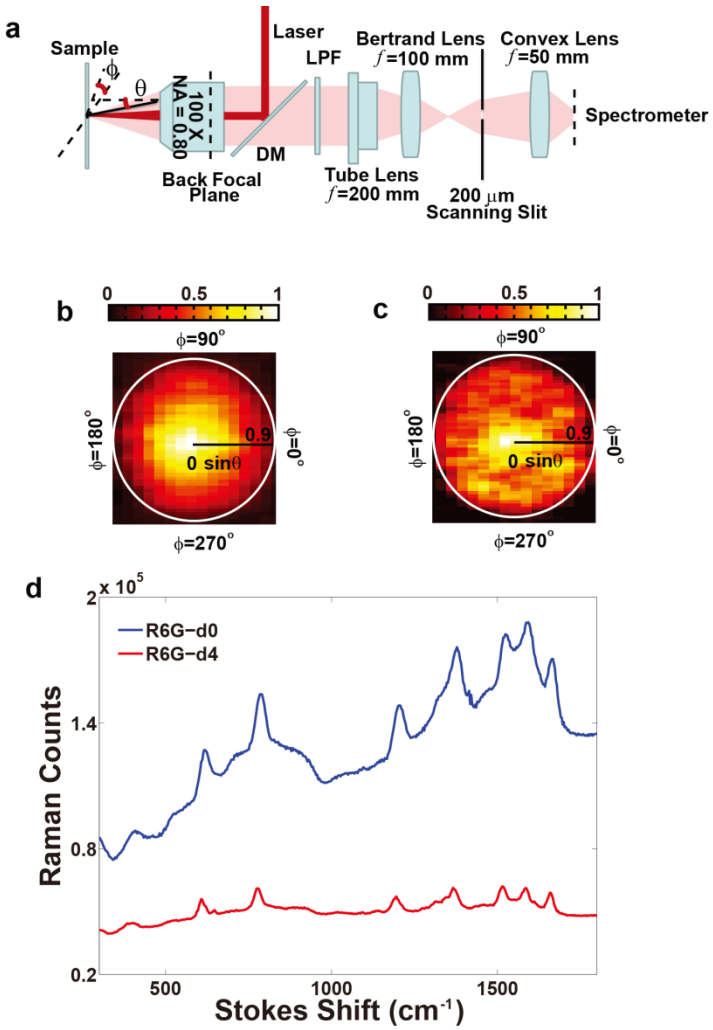

Figure 5-8. Measurement of single molecule Raman emission patterns: set-up and results. (a) Schematic of experimental setup for the measurement of emission patterns. (b) Measured far-field emission pattern of 620 cm^{-1} Raman lines of single R6G-d0 molecule. θ and ϕ are defined in Figure 5-1. The pattern is normalized by the maximum emitted signal. (c) Measured far-field emission pattern of 610 cm^{-1} Raman lines of single R6G-d4 molecule. The pattern is normalized by the maximum emitted signal. (d) Raman spectra measured from the same single molecules whose angular emission patterns are shown in panels (b) and (c).

5.6 Conclusions

In conclusion, we experimentally demonstrate an optical antenna chip that achieves directional SMSERS. SMSERS is one of the few methods of obtaining the vibrational

spectrum of a single molecule and presents opportunities for understanding chemical and biological systems at a fundamental level. Indeed, it is speculated that it may one day enable the observation of a single molecule undergoing a chemical reaction [33]. We anticipate that will be very beneficial for such fundamental scientific studies, but also in technological applications. In addition, we foresee wider applications of antenna approaches to other types of single emitters used in quantum optics and sensing.

5.7 References

[1]. W. E. Moerner, "New directions in single-molecule imaging and analysis," Proceedings of the National Academy of Sciences **104**, 12596-12602 (2007).
[2]. N. Mizuochi, T. Makino, H. Kato, D. Takeuchi, M. Ogura, H. Okushi, M. Nothaft, P. Neumann, A. Gali, and F. Jelezko, "Electrically driven single-photon source at room temperature in diamond," Nature Photonics **6**, 299-303 (2012).
[3]. R. D. Grober, R. J. Schoelkopf, and D. E. Prober, "Optical antenna: Towards a unity efficiency near-field optical probe," Applied Physics Letters **70**, 1354-1356 (1997).
[4]. K. B. Crozier, A. Sundaramurthy, G. S. Kino, and C. F. Quate, "Optical antennas: Resonators for local field enhancement," Journal of Applied Physics **94**, 4632-4642 (2003).
[5]. L. Novotny, and N. van Hulst, "Antennas for light," Nat Photon **5**, 83-90 (2011).
[6]. A. G. Curto, G. Volpe, T. H. Taminiau, M. P. Kreuzer, R. Quidant, and N. F. van Hulst, "Unidirectional Emission of a Quantum Dot Coupled to a Nanoantenna," Science **329**, 930-933 (2010).
[7]. A. Kinkhabwala, Z. Yu, S. Fan, Y. Avlasevich, K. Mullen, and W. E. Moerner, "Large single-molecule fluorescence enhancements produced by a bowtie nanoantenna," Nat Photon **3**, 654-657 (2009).
[8]. K. G. Lee, X. W. Chen, EghlidiH, KukuraP, LettowR, RennA, SandoghdarV, and GotzingerS, "A planar dielectric antenna for directional single-photon emission and near-unity collection efficiency," Nat Photon **5**, 166-169 (2011).
[9]. K. L. Wustholz, C. L. Brosseau, F. Casadio, and R. P. Van Duyne, "Surface-enhanced Raman spectroscopy of dyes: from single molecules to the artists' canvas," Physical Chemistry Chemical Physics **11**, 7350-7359 (2009).
[10]. M. Fleischmann, P. J. Hendra, and A. J. McQuillan, "Raman spectra of pyridine adsorbed at a silver electrode," Chemical Physics Letters **26**, 163-166 (1974).
[11]. D. L. Jeanmaire, and R. P. Van Duyne, "Surface raman spectroelectrochemistry: Part I. Heterocyclic, aromatic, and aliphatic amines adsorbed on the anodized silver electrode," Journal of Electroanalytical Chemistry and Interfacial Electrochemistry **84**, 1-20 (1977).
[12]. M. G. Albrecht, and J. A. Creighton, "Anomalously intense Raman spectra of

pyridine at a silver electrode," Journal of the American Chemical Society **99**, 5215-5217 (1977).
[13]. S. Nie, and S. R. Emory, "Probing Single Molecules and Single Nanoparticles by Surface-Enhanced Raman Scattering," Science **275**, 1102-1106 (1997).
[14]. K. Kneipp, Y. Wang, H. Kneipp, L. T. Perelman, I. Itzkan, R. R. Dasari, and M. S. Feld, "Single Molecule Detection Using Surface-Enhanced Raman Scattering (SERS)," Physical Review Letters **78**, 1667-1670 (1997).
[15]. A. Ahmed, and R. Gordon, "Single Molecule Directivity Enhanced Raman Scattering using Nanoantennas," Nano Letters **12**, 2625-2630 (2012).
[16]. J. A. Dieringer, R. B. Lettan, K. A. Scheidt, and R. P. Van Duyne, "A Frequency Domain Existence Proof of Single-Molecule Surface-Enhanced Raman Spectroscopy," Journal of the American Chemical Society **129**, 16249-16256 (2007).
[17]. E. C. Le Ru, J. Grand, I. Sow, W. R. C. Somerville, P. G. Etchegoin, M. Treguer-Delapierre, G. Charron, N. Félidj, G. Lévi, and J. Aubard, "A Scheme for Detecting Every Single Target Molecule with Surface-Enhanced Raman Spectroscopy," Nano Letters **11**, 5013-5019 (2011).
[18]. S. L. Kleinman, E. Ringe, N. Valley, K. L. Wustholz, E. Phillips, K. A. Scheidt, G. C. Schatz, and R. P. Van Duyne, "Single-Molecule Surface-Enhanced Raman Spectroscopy of Crystal Violet Isotopologues: Theory and Experiment," Journal of the American Chemical Society **133**, 4115-4122 (2011).
[19]. E. J. Blackie, E. C. L. Ru, and P. G. Etchegoin, "Single-Molecule Surface-Enhanced Raman Spectroscopy of Nonresonant Molecules," Journal of the American Chemical Society **131**, 14466-14472 (2009).
[20]. E. Blackie, E. C. Le Ru, M. Meyer, M. Timmer, B. Burkett, P. Northcote, and P. G. Etchegoin, "Bi-analyte SERS with isotopically edited dyes," Physical Chemistry Chemical Physics **10**, 4147-4153 (2008).
[21]. P. G. Etchegoin, M. Meyer, E. Blackie, and E. C. Le Ru, "Statistics of Single-Molecule Surface Enhanced Raman Scattering Signals: Fluctuation Analysis with Multiple Analyte Techniques," Analytical Chemistry **79**, 8411-8415 (2007).
[22]. E. C. Le Ru, M. Meyer, and P. G. Etchegoin, "Proof of Single-Molecule Sensitivity in Surface Enhanced Raman Scattering (SERS) by Means of a Two-Analyte Technique," The Journal of Physical Chemistry B **110**, 1944-1948 (2006).
[23]. J. P. Camden, J. A. Dieringer, Y. Wang, D. J. Masiello, L. D. Marks, G. C. Schatz, and R. P. Van Duyne, "Probing the Structure of Single-Molecule Surface-Enhanced Raman Scattering Hot Spots," Journal of the American Chemical Society **130**, 12616-12617 (2008).
[24]. W. Zhu, M. G. Banaee, D. Wang, Y. Chu, and K. B. Crozier, "Lithographically Fabricated Optical Antennas with Gaps Well Below 10 nm," Small **7**, 1761-1766 (2011).
[25]. P. B. Johnson, and R. W. Christy, "Optical Constants of the Noble Metals," Physical Review B **6**, 4370-4379 (1972).
[26]. Y. Chu, M. G. Banaee, and K. B. Crozier, "Double-Resonance Plasmon Substrates for Surface-Enhanced Raman Scattering with Enhancement at Excitation and Stokes Frequencies," ACS Nano **4**, 2804-2810 (2010).
[27]. T. J. Seok, A. Jamshidi, M. Kim, S. Dhuey, A. Lakhani, H. Choo, P. J. Schuck, S. Cabrini, A. M. Schwartzberg, J. Bokor, E. Yablonovitch, and M. C. Wu, "Radiation Engineering of Optical Antennas for Maximum Field Enhancement," Nano Letters **11**,

2606-2610 (2011).
[28]. D. Wang, T. Yang, and K. B. Crozier, "Optical antennas integrated with concentric ring gratings: electric field enhancement and directional radiation," Opt. Express **19**, 2148-2157 (2011).
[29]. A. Ahmed, and R. Gordon, "Directivity Enhanced Raman Spectroscopy Using Nanoantennas," Nano Letters **11**, 1800-1803 (2011).
[30]. N. Mirsaleh-Kohan, V. Iberi, P. D. Simmons, N. W. Bigelow, A. Vaschillo, M. M. Rowland, M. D. Best, S. J. Pennycook, D. J. Masiello, B. S. Guiton, and J. P. Camden, "Single-Molecule Surface-Enhanced Raman Scattering: Can STEM/EELS Image Electromagnetic Hot Spots?," The Journal of Physical Chemistry Letters **3**, 2303-2309 (2012).
[31]. J.-J. Greffet, "Nanoantennas for Light Emission," Science **308**, 1561-1563 (2005).
[32]. W. Zhu, D. Wang, and K. B. Crozier, "Direct Observation of Beamed Raman Scattering," Nano Letters **12**, 6235-6243 (2012).
[33]. B. Sharma, R. R. Frontiera, A.-I. Henry, E. Ringe, and R. P. Van Duyne, "SERS: Materials, applications, and the future," Materials Today **15**, 16-25 (2012).

6 Wafer-scale metasurface for total power absorption, local field enhancement and single molecule Raman spectroscopy

6.1 Introduction

The ability to detect molecules at low concentrations is highly desired for applications that range from basic science to healthcare. Considerable interest also exists for ultrathin materials with high optical absorption, e.g. for microbolometers and thermal emitters. Metal nanostructures present opportunities to achieve both purposes. Metal nanoparticles can generate gigantic field enhancements, sufficient for the Raman spectroscopy of single molecules. Thin layers containing metal nanostructures ("metasurfaces") can achieve near-total power absorption at visible and near-infrared wavelengths. Previous studies [1-6] have shown that metasurfaces enable efficient optical absorption at visible and infrared wavelengths. With the exception of Ref. [6], however, their fabrication involved electron beam lithography, a time-consuming and costly method that is only suitable over small areas (usually < 1 mm^2). Ref. [6] aimed to address this by instead employing silver nanocubes, but their chemical synthesis is by no means straightforward. Thus far, however, both aims (i.e. single molecule Raman and total power absorption) have only been achieved using metal nanostructures produced by techniques (high resolution lithography or colloidal synthesis) that are complex and/or difficult to implement over large areas.

In this Chapter, we realize metasurfaces with near-complete absorption and record areas (4 inch wafers, i.e. ~80 cm^2) using standard sputtering and evaporation techniques. These consist of silver nanoparticle islands formed over a silver mirror, with an SiO_2 spacer layer, and are termed "SIOM metasurfaces". We show that their reflectance can be tuned by adjusting parameters that include the spacer thickness and the evaporation rate, which in turn modifies the silver nanoparticle island morphology. We discuss the physical interpretation of the perfect absorption phenomenon in terms of equivalent electric and magnetic surface currents. These are enabled by the SIOM metasurface supporting both electric and magnetic resonances. The perfect absorption behavior is accompanied by huge local field enhancement that is advantageous for surface-enhanced Raman scattering (SERS) [7-10]. We perform SERS measurements of molecules adsorbed to the SIOM metasurfaces and determine the enhancement factors (EFs), i.e. the factors by which the Raman signals from molecules on the SIOM metasurface are increased compared to molecules in the pure liquid form (i.e. no metasurface). We find that the SIOM metasurfaces exhibit EFs that are more than one order of magnitude larger than those of silver nanoparticle islands on glass. We furthermore demonstrate, for the first time, single molecule SERS with a metasurface. The large extent of our SIOM metasurface enables the observation of an unprecedented number (>7000) of single molecule SERS events.

6.2 Design and fabrication of SIOM metasurface

The SIOM metasurface we introduce is schematically illustrated as Figure 6-1a.

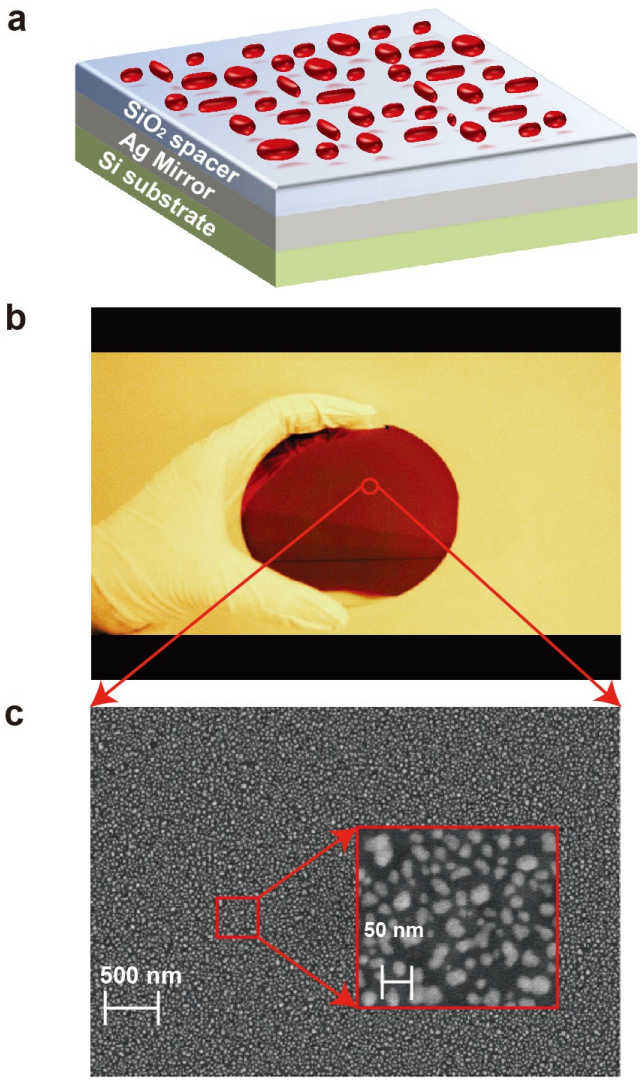

Figure 6-1. (a) Schematic of SIOM metasurface. Silver nanoparticle islands (depicted as red particles) are deposited on a 50 nm-thick SiO_2 spacer above a 120 nm-thick silver mirror. Silicon is used as supporting substrate. b. Image of fabricated SIOM metasurface with a diameter of 4 inches. c. Scanning electron microscope (SEM) image of a portion of SIOM metasurface. Inset: SEM image of metasurface at higher magnification.

The fabrication of SIOM metasurface begins with evaporation (1 Å/sec) of titanium to a thickness of 5 nm on a silicon substrate to form an adhesion layer. After this, silver is deposited to a thickness of 120 nm on the titanium layer by evaporation (1 Å/sec). A 50-nm thick SiO_2 layer is then deposited by sputtering (0.4 Å/sec). Silver is then evaporated at a slow rate (0.2 Å/sec), thereby producing silver nanoparticle islands. The duration of this evaporation step is such that the amount of silver deposited is equivalent to the

amount that would be contained in 6.5 nm thick film, as measured by crystal oscillation monitor. These three steps complete the fabrication of the SIOM metasurface. We note that our approach involves no complex or expensive fabrication procedures, and is inherently suitable for the producing substrates with large areas. Indeed, the SIOM metasurfaces are on 4 inch wafers (Figure 6-1b), only limited by the sizes of the holders in our evaporator and sputterer. We furthermore note that we choose to employ a Si wafer as the underlying substrate for convenience. The silver mirror, however, is of sufficient thickness so that there is almost no penetration of light into the Si substrate. The optical properties of the substrate are therefore unimportant, meaning that even more economical substrate materials (e.g. plastic or steel) could be used.

An SEM image of a portion of the SIOM metasurface is shown in Figure 1c. The SEM image verifies that the silver nanoparticle islands are formed on the SiO_2 layer.

6.3 Perfect optical absorption of SIOM

It is seen from Figure 6-1b that the fabricated SIOM metasurface appears red in color. To understand this phenomenon, we measure its reflectance. In the reflection spectra measurements, the SIOM metasurface is illuminated by light from a halogen lamp focused by a microscope objective (NA=0.15, magnification 5×). The reflected light from the metasurface is collected by the same objective lens and analyzed by the spectrometer equipped with a thermoelectrically-cooled charge couple device (CCD). The reflected light from an area of the same sample containing only the SiO_2 spacer and silver mirror (i.e. no silver nanoparticle islands) is measured as reference. The normalized reflection spectrum is then found by dividing the spectrum measured from the SIOM by the

reference spectrum. This is then multiplied by the theoretical reflection spectrum of the sample containing only the SiO_2 spacer and silver mirror found using the method of Ref. [11]. This yields the SIOM reflection spectrum in absolute terms.

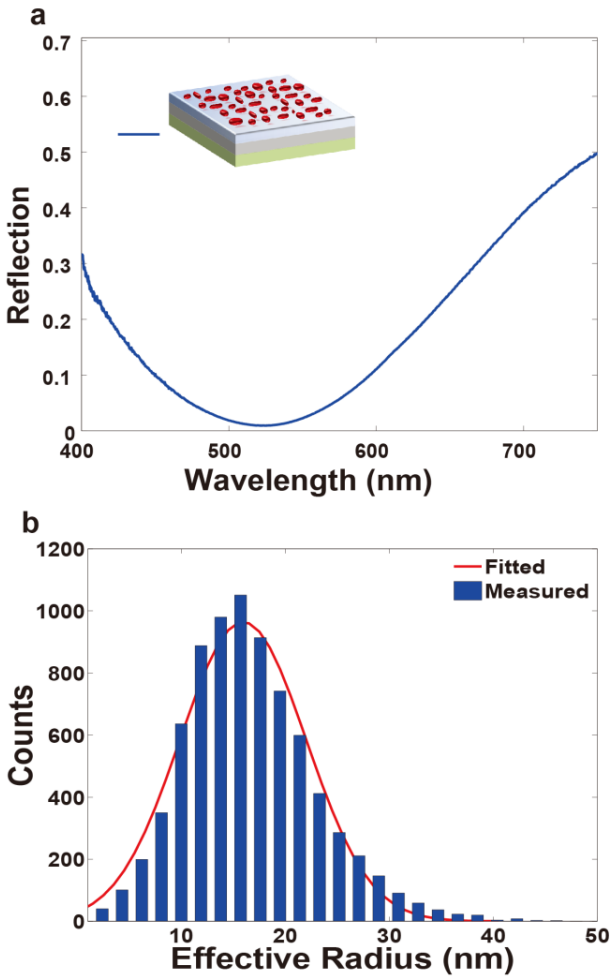

Figure 6-2. (a) Reflection spectra of SIOM metasurface. (b) Histogram of effective radii of silver nanoparticle islands of SIOM metasurface.

The reflection spectrum (Figure 6-2a) shows a dip at $\lambda \approx 525\,nm$ at which the reflectance is very small. As we discuss further below, the dip is related to the excitation of localized surface plasmons on the silver nanoparticle islands, but these are strongly modified by the presence of the silver mirror. As the reflectance is below 10% over a band extending from $\lambda \approx 450\,nm$ to $600\,nm$, the SIOM appears red in color (Figure

6-1b). To understand the origin of the reflection spectrum dip, we analyze the sizes of the nanoparticle islands. We randomly pick a 5 μm × 3.5 μm region from the SEM of the SIOM substrate, import the image into MATLAB (The Mathworks Inc.), and find the effective radius of each silver nanoparticle island within this region. The effective radius is the radius of a circle that would have the same area as the area of the nanoparticle island, as found from analysis of the SEM image. The effective radii found in this way are tabulated in a histogram (Figure 6-2b), and can be seen to follow a Gaussian distribution (red fitted curve) that peaks at an effective radius of 15.4 nm and has a standard deviation of 6 nm. We check other areas of the SIOM substrate and obtain similar results. It is likely that this size dispersion contributes to the broad width of the reflection dip.

From Figure 6-2a, it can be seen that reflectance from the SIOM substrate is very low, being below 1% at a wavelength of λ=525 nm. Indeed, the SIOM metasurface achieves near total power absorption. The perfect absorption phenomenon can be interpreted as arising from the metasurface inducing equivalent magnetic and electric surface currents that produce far-fields that interfere destructively [6]. To explore this interpretation, we randomly choose a $1\ \mu m \times 1\ \mu m$ region (Figure 6-3a) of the SEM of Figure 6-1c, and simulate the fields under plane wave illumination using the finite difference time domain (FDTD) method. The distribution of the sizes of the silver islands of the modeled structure (Figure 6-3a) is close to that shown in Figure 6-2b of the main part of the paper. The simulations take each silver island to have a cross-sectional shape that does not vary in the *z*-direction (normal to the substrate). This cross-sectional shape is imported directly from the SEM image. The silver islands are taken as being 14 nm

thick (the method to estimate this value will be discussed later). The thickness of the SiO_2 is 50 nm and the dielectric permittivity of silver is taken from Ref. [12]. Plane wave illumination from the air side at normal incidence with the electric field polarized along the *x* direction is used (inset of Figure 6-3b). Periodic boundary conditions are applied along the *x*- and the *y*-boundaries of the unit cell. Perfectly matched layers are used at the *z*-boundaries of the simulation region.

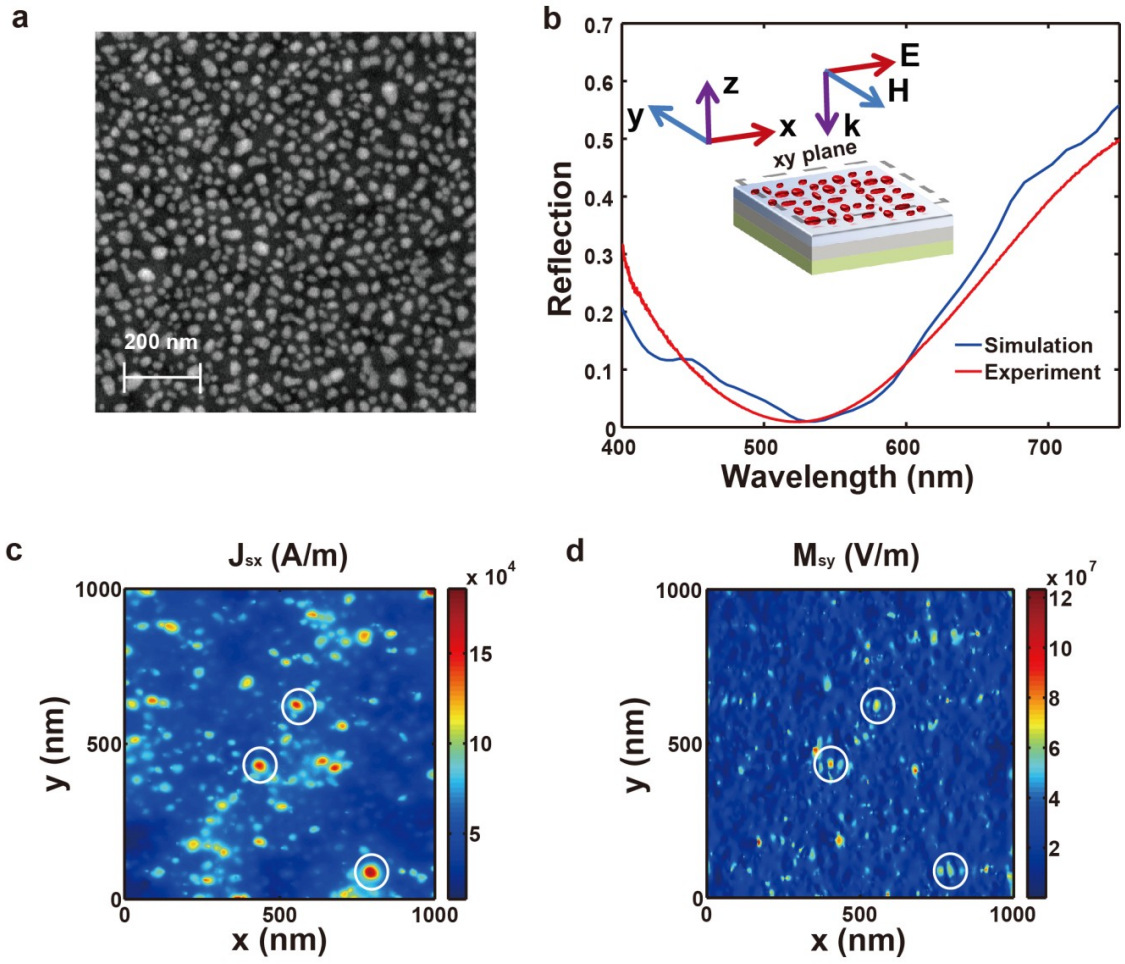

Figure 6-3. Equivalent electric currents and magnetic currents of SIOM metasurface. (a) SEM image of 1 μm × 1 μm area of SIOM metasurface that is simulated. (b) Simulated and experimentally measured reflection spectra of SIOM metasurface. Inset: *xy* plane (6 nm above top surface of silver islands) over which equivalent currents are calculated. (c) Amplitude of *x* component of simulated equivalent electric current density in *xz* plane which is 6 nm above top surface of silver islands. (d) Amplitude of *y* component of simulated equivalent electric current density in *xz* plane which is 6 nm above top surface of silver island.

The simulated reflection spectrum is shown as Figure 6-3b along with the experimentally-measured reflection spectrum (see also Figure 6-2a). It can be seen that the position of the dip (λ=530 nm) of the simulated spectrum is close to that of the experimental one (λ=525 nm). Furthermore, the depth and width of the dip of the simulated spectrum are in reasonable agreement with those of the experimentally-measured spectrum. It is not unexpected that there are some differences due to the approximations made in the simulations, e.g. truncated particles at the edges of the unit cell, periodic boundary conditions, and silver islands with cross-sectional shapes that do not vary in the *z*-direction.

The surface equivalence theorem [11] is used to find the equivalent electric and magnetic current densities over the SIOM metasurface (Figure 6-3a) on an *xy* plane just above the tops of the silver islands:

$$\vec{J}_s(x,y) = \hat{z} \times \vec{H}(x,y) \qquad (6.1a)$$

$$\vec{M}_s(x,y) = -\hat{z} \times \vec{E}(x,y) \qquad (6.1b)$$

where $\vec{J}_s(x,y)$ and $\vec{M}_s(x,y)$ are the equivalent electric and magnetic current densities at position (*x, y*), respectively, $\hat{z}$ is the direction of surface normal, and $\vec{H}(x,y)$ and $\vec{E}(x,y)$ are the magnetic and electric fields at position (*x, y*), respectively. The surface equivalence theorem can be interpreted as a vector form of Huygens' Principle, with the equivalent electric and magnetic currents serving as sources that generate the fields outside the surface. To find the reflectance, we consider the far-fields in the *z*-direction, which can be shown to be given as follows.

$$\vec{E}_j = i\omega u_0 \frac{e^{ikz}}{4\pi|\vec{r}|} \iint \vec{J}_s(x,y)dxdy \qquad (6.2a)$$

$$\vec{E}_m = \frac{e^{ikz}}{4\pi|\bar{r}|} ik\hat{z} \times \iint \vec{M}_s(x,y)dxdy \quad (6.2b)$$

where $\vec{E}_j$ and $\vec{E}_m$ are the electric fields generated by electric currents and magnetic currents, respectively. $\bar{r}$ is the observation point. k is the wave number in free space. The integrations are performed over the surface over which the magnetic and electric currents are specified. From the simulation results, we find that the x component dominates $\iint \vec{J}_s(x,y)dxdy$ and that the y component dominates $\iint \vec{M}_s(x,y)dxdy$ at λ=530 nm. Equations (6.2a) and (6.2b) can therefore be simplified as follows:

$$\vec{E}_j = \hat{x} i\omega u_0 \frac{e^{ikz}}{4\pi|\bar{r}|} \iint J_{sx}(x,y)dxdy \quad (6.3a)$$

$$\vec{E}_m = -\hat{x} \frac{e^{ikz}}{4\pi|\bar{r}|} ik \iint M_{sy}(x,y)dxdy \quad (6.3b)$$

where $J_{sx}(x,y)$ is the x component of $\vec{J}_s(x,y)$ and $M_{sy}(x,y)$ is the y component of $\vec{M}_s(x,y)$. From Equations (6.3a) and (6.3b), it can be seen that the far-fields generated by the electric and magnetic currents destructively interfere if the ratio between total electric currents $\iint J_{sx}(x,y)dxdy$ and total magnetic currents $\iint M_{sy}(x,y)dxdy$ is $\omega\mu_0/k$ (≈377 ohm).

The equivalent magnetic and electric surface currents of modeled structures (Figure 6-3a) are found from the method discussed above. These current distributions are shown as Figure 6-3c and Figure 6-3d. It can be seen that the regions of enhanced electric currents are colocated with those of the enhanced magnetic currents. This originates from the SIOM metasurface simultaneously supporting electric and magnetic resonances; we discuss this point further below. These results show that, at the simulated resonance of λ=530 nm, the total effective magnetic and electric currents, i.e. each integrated over the unit cell, are in a ratio (383+1.2i ohm) that is close to 377 ohm, i.e. the impedance of free

space. The results therefore predict destructive cancellation of the far-fields produced by these currents, leading to the total absorption phenomenon.

The simultaneous existence of magnetic and electric resonances has been previously been studied in relation to total absorption [13]. To further explore the near-total absorption achieved by the SIOM substrate, we study a simplified model consisting of a silver disk (radius 29 nm) formed on a silver mirror, with an SiO_2 spacer layer (50 nm thick) between them. The disks are assumed to be on a square lattice (340 nm period). The disk thickness is taken as 14 nm thick, in order to match the value estimated for the actual SIOM metasurface Plane wave illumination from the air side at normal incidence with the electric field polarized along the *x* direction is used (Figure 6-4a). Periodic boundary conditions are used along the *x* and *y* directions, with a unit cell size of 340 × 340 nm. Perfectly matched layers are used at the z direction boundaries.

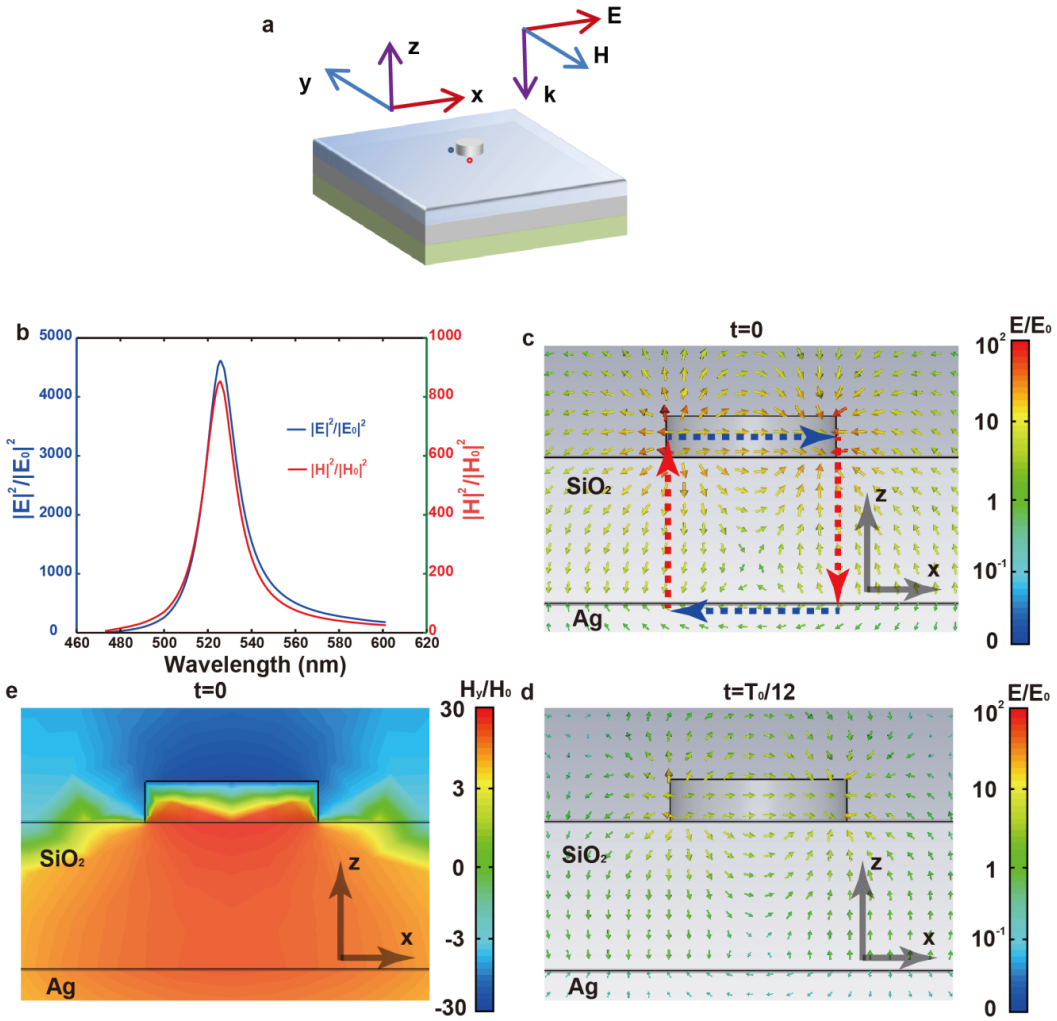

Figure 6-4. Electromagnetic simulation of plasmonic resonance of SIOM metasurface (a) Schematic of simplified SIOM metasurface in the simulation. (b) Blue curve: electric field intensity at monitor point (blue dot of inset), normalized by intensity of illuminating plane wave ($|E|^2/|E_0|^2$). Electric field intensity monitor point is along x axis of silver disk, at 0.5 nm from its outer radius and 5 nm above top surface of SiO_2. Red curve: magnetic field intensity at monitor point (red dot of inset), normalized by intensity of illuminating plane wave ($|H|^2/|H_0|^2$). Magnetic field intensity monitor point is 0.5 nm below center of silver disk, i.e. in underlying SiO_2. (c) Vector plot of instantaneous electric field normalized to incident field on xz plane cross-section through silver disk when it is illuminated at λ=525 nm, at time instant denoted $t = 0$. (d) Vector plot of instantaneous electric field normalized to incident field on xz plane cross-section through silver disk when illuminated at λ=525 nm, at time instant denoted $t = T_0/12$, where T_0 is period. e. Plot of instantaneous magnetic field (y component) normalized to incident field on xz plane cross-section through silver disk, at $t = 0$.. Illumination wavelength is λ=525 nm. Other components of magnetic field are not plotted as they are much weaker than y component.

The electric field intensity monitor point is along x axis of silver disk, at 0.5 nm

from its outer radius and 5 nm above top surface of the SiO_2. The magnetic field intensity monitor point is 0.5 nm below the center of the silver disk, i.e. in the underlying SiO_2. The locations of these monitor points are also indicated in Figure 6-4a. The intensities, normalized to those of the illumination, are plotted as a function of wavelength in Figure 6-4. It can be seen that the silver disk has both electric and magnetic resonances at the wavelength of λ=525 nm. To gain physical insight into the nature of these resonances, the normalized electric fields around the silver disk at two different times are shown as Figure 6-4c and Figure 6-4d. The variation of electric fields in the time domain determines the directions of the induced conduction currents (as indicated by the blue arrows in Figure 6-4c) and displacement currents (as indicated by the red arrows in Figure 6-4c). As shown in Figure 6-4c, the conduction and displacement currents form a loop. The area enclosed by the current loop generates inductance (L) and the gap between the silver disk and mirror introduces capacitance (C). The resultant LC circuit generates a magnetic resonance. When illuminated on resonance, the magnetic field within the current loop is therefore enhanced (Figure 6-4e). As we discuss further below, this facilitates near-perfect absorption.

Using the techniques for the modeled structures in Figure 6-3a, the equivalent currents are calculated across an *xy* plane that is 6 nm above the simplified SIOM metasurface. Similar to the simulation results for the complex SIOM metasurface (Figure 6-3a), the simulations of the simplified structure show that the *x* component of electric currents and *y* component of magnetic currents are much larger than their other components. Therefore, we plot the amplitudes of *x* component of $\vec{J}_s(x,y)$ and *y* component of $\vec{M}_s(x,y)$ in one unit cell of the simplified SIOM metasurface in Figure

6-5a and Figure 6-5b, respectively. As expected, the effective electric currents and magnetic currents are enhanced around the silver island by the magnetic and electric resonances at λ=525 nm. It can be seen that the spatial distributions of the electric and magnetic currents – with the former being enhanced in the region above the disk while the latter is enhanced in a similar way, but with the addition of two lobes – are similar to those of the SIOM metasurface (circled regions of Figure 6-3c-d). We furthermore calculate $\iint J_{sx}(x,y)dxdy$ and $\iint M_{sy}(x,y)dxdy$. These are found to be in a ratio of 381+7i ohm, which is again close to 377 ohm. The simulations therefore predict that the simplified SIOM metasurface acts as an almost perfect absorber. For comparison, we perform similar calculations on a structure that is the same, but without the silver mirror (results not shown). The ratio between the effective magnetic and electric currents at λ=525 nm is 13949i ohm, which is very different from 377 ohm, meaning that perfect absorption is not achieved.

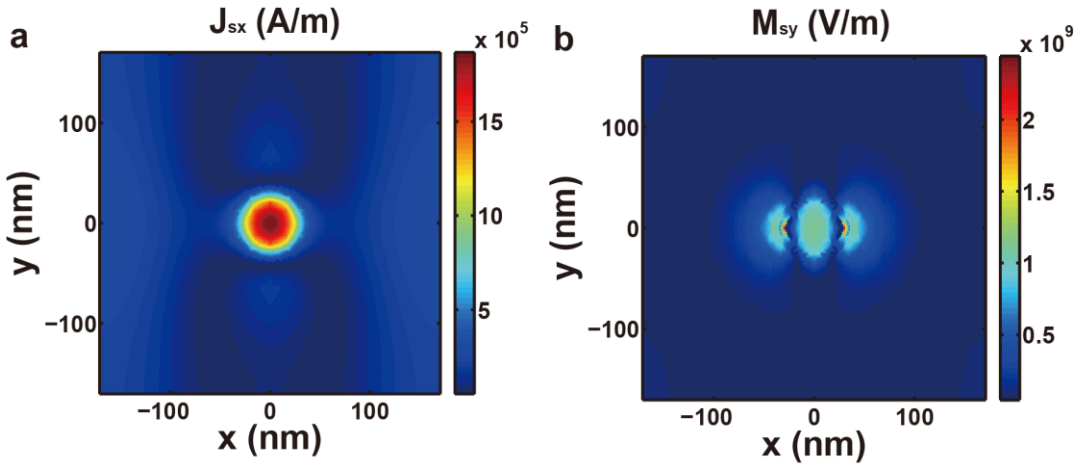

Figure 6-5. Simulated equivalent electric and magnetic currents of simplified SIOM metasurface. (a) Amplitudes of *x* component of effective electric current density in an *xz* plane which is 6 nm above top surface of silver disk. (b) Amplitudes of *y* component of effective electric current density in an *xz* plane which is 6 nm above top surface of silver disk.

6.4 Tunable optical absorption of SIOM

The SIOM metasurface reflectance spectrum is readily tuned by modifying the fabrication process. Varying the evaporation rate presents a means for doing this, as it in turn modifies the sizes of the nanoparticle islands that are produced [14, 15]. To show the tunable optical absorption of SIOM with 50-nm thick SiO_2 spacer by changing the evaporation rate, we fabricate three SIOM samples using silver evaporation rates that vary from 0.2 Å/sec to 0.6 Å/sec.

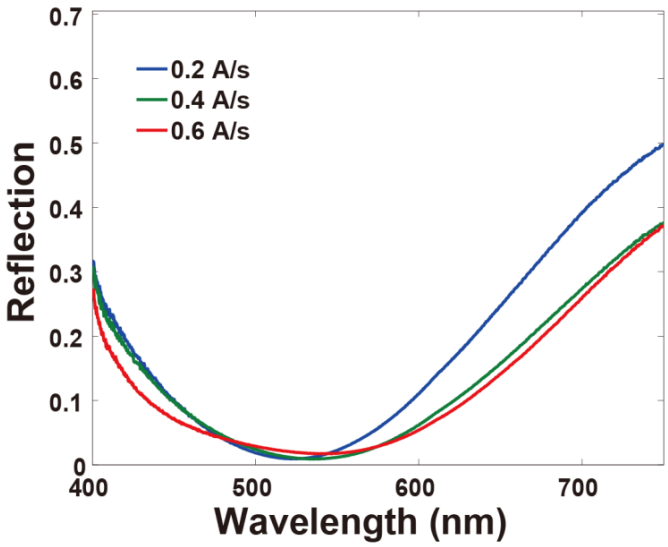

Figure 6-6. Reflection spectra of SIOM substrates with silver evaporation rates of 0.2 Å/sec, 0.4 Å/sec and 0.6 Å/sec.

In Figure 6-6, the reflectance spectra of SIOM metasurfaces produced with different silver evaporation rates are shown. It can be seen that increasing the evaporation rate red-shifts the reflectance dip position, which indicates the silver nanoparticle islands increase in size with evaporation rate. Annealing after deposition is another means for modifying the sizes of the silver nanoparticle islands [16, 17]. One would also expect that modifying the thickness of the SiO_2 layer would permit the reflectance spectrum to be tuned, due to the important role of the nanoparticle island-film coupling in this system. In

Figure 6-7, we show reflectance spectra for SIOM substrates fabricated using methods that are identical, apart from the spacer layer thickness being varied from 30 to 65 nm. It can be seen that the reflectance dip blue-shifts with increasing spacer layer thickness. This is in agreement with the previous theoretical studies [18, 19] that show that the coupling between an optical antenna and mirror (i. e. silver mirror here) reduces with their separation, leading to a blue-shift of the plasmon resonance.

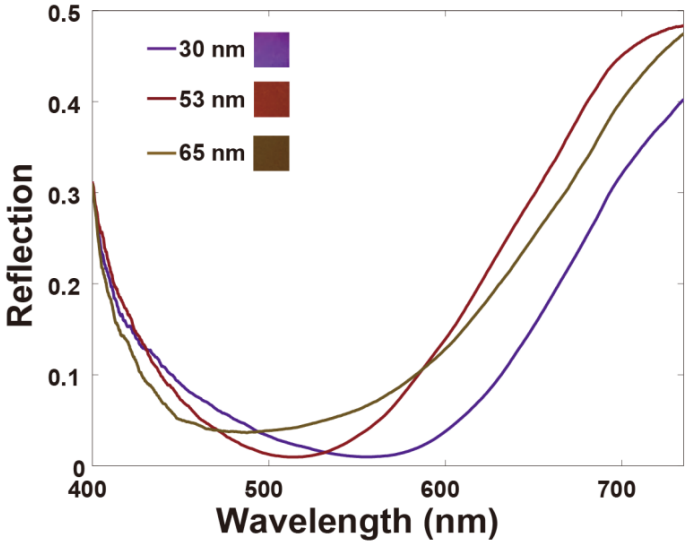

Figure 6-7. Reflection spectra of SIOM metasurfaces having SiO_2 spacer layers with thicknesses of 30 nm, 53 nm and 65 nm. Inset: images of fabricated SIOM with different thicknesses of SiO_2 layer

6.5 SIOM's application for SERS

Because our SIOM metasurface achieve near-total optical absorption in a very thin region at its surface, it is intuitive to expect that huge local field enhancement will occur around the silver island nanoparticles. This makes it an ideal candidate for SERS. SERS substrates patterned with high resolution lithography (e.g. e-beam) achieve very high performance and reproducibility [20-28], but have high cost and small active areas. For many applications, however, large area and low cost are critical. This has motivated the

development of SERS substrates patterned by methods other than high resolution lithography, e.g. with nanomaterials such as nanospheres [29, 30] or nanoshells [31]. Our SIOM metasurfaces, however, present further advantages in this regard, however, as their fabrication does not involve lithography, nor the use of nanomaterials, but rather standard thin film deposition methods. The SIOM metasurface generates larger SERS enhancements than its simpler counterpart that consists of silver islands on an SiO_2 substrate. This can be understood by considering the excitation and scattered fields in the SERS process. The SIOM metasurface achieves near-total absorption, meaning that the coupling between excitation fields and the plasmonic resonance of the silver islands is more efficient for the SIOM metasurface than for the simpler SERS substrates (silver islands on glass). For the SIOM metasurface, therefore, the field enhancement of the excitation is stronger. This is confirmed by simulations of the electric field intensities produced by the SIOM (modeled structure shown in Figure 6-3a) and by its counterpart consisting of silver islands on glass. The results of simulation are shown in Figure 6-8. These plot the field intensity enhancement on a plane that is half-way through the silver islands, i.e. 7 nm above the SiO_2 surface. It is seen that the peak value (1.2×10^4) of the field intensity enhancement of SIOM is ~3.3 times larger than that (3.6×10^3) of the silver islands on SiO_2.

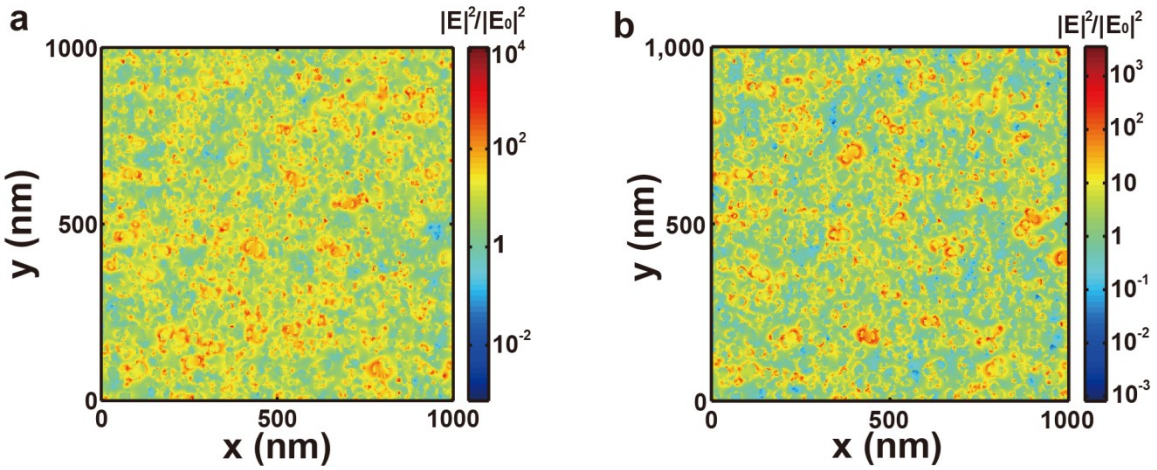

Figure 6-8. Simulated field intensity enhancement (field intensity normalized by the intensity of incident light) of SIOM and silver islands on SiO_2 at *xz* plane (7 nm above the top surface of the SiO_2 layer) at a wavelength of λ=530 nm. (a) Field intensity enhancement of SIOM. (b) Field intensity enhancement of silver islands on SiO_2

In addition to enhancement of the incident field, the silver mirror reshapes the SERS emission patterns so that the emission is mostly radiated into air [25, 32], rather than into the substrate.

For comparison purposes, we characterize the SERS performance not only of our SIOM metasurfaces (Figure 6-1b), but also that of a substrate consisting of silver nanoparticle islands on indium tin oxide coated glass. The latter is fabricated by evaporating silver at the same rate as that used for the SIOM metasurface. This produces silver nanoparticle islands very similar to those of the SIOM metasurface, as confirmed by scanning electron microscopy (not shown here).

The samples (SIOM and silver islands on glass) are immersed in a solution of benzenethiol in ethanol (3×10^{-3} mol/L) for 1 hour. This results in a self-assembled monolayer of benzenethiol on the silver islands. After removal from the benzenethiol solution, the samples are rinsed in ethanol and blown dry with nitrogen. SERS measurements are made with a Raman microscope (Horiba Jobin Yvon, LabRam)

equipped with a spectrometer and a thermoelectrically-cooled charge coupled device (CCD). The excitation laser wavelength is λ=532 nm and the power impinging upon the substrate is 0.03 mW. These parameters are used for the measurements both on the SIOM metasurface and on the silver nanoparticle islands on glass. An objective lens (NA=0.15, magnification 5×) is used to focus the excitation laser on the sample and collect the emitted Raman signals. The signal accumulation time for the CCD detector is 10 seconds. The results (Figure 6-8a) of SERS measurements show that the SERS signals (and hence signal-to-noise ratios) of all Raman lines are much larger for the SIOM metasurface than for the silver island nanoparticles on glass. This indicates that the SIOM metasurface produces considerably stronger SERS enhancements than do the silver nanoparticle islands on SiO_2. To quantify the improvement, we analyze the 1072 cm^{-1} and 1586 cm^{-1} Raman lines. The SERS enhancement factor of these two Raman lines for the SIOM metasurface and the silver nanoparticle islands on glass are calculated by comparing SERS measurements of Figure 4a with measurements made on pure benzenethiol liquid using the technique shown in a previous study [22]. To calculate the SERS enhancement factor, SERS measurements are made of Raman scattering from pure benzenethiol liquid sandwiched between a microscope slide and a coverslip. The benzenthiol thickness (500 μm) is defined using a spacer to separate the slide and coverslip. The SERS enhancement factor is then given by $EF = \frac{I_{SERS}/N_{SERS}}{I_{REF}/N_{REF}}$, where I_{SERS} and I_{REF} are the signal intensities measured in the SERS and Raman experiments, respectively. These intensities are the heights of the Raman lines in the spectra with the background subtracted. N_{SERS} and N_{REF} are the numbers of molecules in the SERS and Raman experiments, respectively. N_{SERS} is given by the area of the exposed silver surfaces of the SIOM substrate or simple silver

islands multiplied by the packing density of benzenethiol (6.8×10^{14} cm^{-2} [33]). To estimate the area of the exposed silver surfaces, we model each silver nanoparticle island as a cylindrical pillar whose radius is chosen to yield a cross sectional area matching that of the silver nanoparticle island, as determined from the SEM image. According to the measurements made using a crystal oscillation monitor, the amount of silver deposited is equivalent to that contained in a 6.5 nm thick film. The heights of the pillars are therefore estimated by equating their volume to that of a 6.5 nm thick film. For the SIOM metasurface shown in Figure 6-1c for example, this yields an estimated height of 14 nm. The estimated surface area of the exposed silver surfaces is then taken as the areas of the tops and sides of the cylinders. N_{REF} is given by the confocal collection volume of the microscope multiplied by the density of pure benzenethiol (9.8 mol/L). The collection volume is found by measuring the Raman signal from a silicon wafer as a function of its position along the optical axis [22].

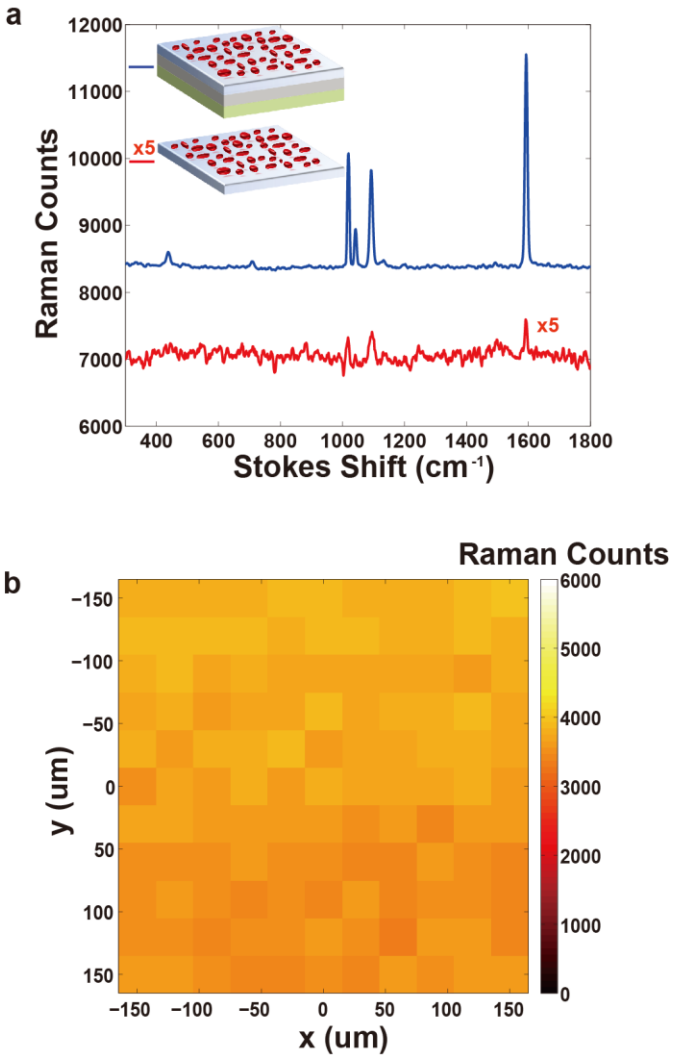

Figure 6-9. SERS measurement. (a) SERS spectra measured from SIOM metasurface (blue line) and silver island nanoparticles on SiO_2 (red line) coated with benzenethiol. For display purposes, Raman spectrum from SIOM metasurface is shifted vertically by 7000 Raman counts and Raman spectrum from silver nanoparticle islands on glass is enlarged by 5 times. (b) Mapping of SERS signal of 1586 cm^{-1} Raman line over SIOM metasurface. Plotted quantity is intensity of 1586 cm^{-1} Raman line with background subtracted.

The experimentally-determined SERS enhancement factors of the 1072 cm^{-1} and 1586 cm^{-1} Raman lines of the SIOM metasurface are 4.3×10^7, and 4.4×10^7, respectively. By contrast, for the same Raman lines, the silver island nanoparticles on glass exhibit measured enhancement factors of 2.5×10^6 and 1.8×10^6. The enhancement factors of the 1072 cm^{-1} and 1586 cm^{-1} Raman lines of the SIOM metasurface are

therefore respectively 17 and 24 times larger than those of the silver island nanoparticles on glass. The more than one order of magnitude boost in enhancement factor results from improvement in the coupling between the incident light and plasmon resonance of the SIOM metasurface. The Raman scattering is furthermore efficiently collected due to the presence of the silver mirror.

We next investigate the uniformity in SERS enhancement with position on the SIOM metasurface. A 300 μm × 300 μm region of the SIOM metasurface is scanned with a step size of 30 μm, with a SERS spectrum obtained at each stage position. The measurement parameters are described in the Methods section. We plot the intensity of the 1586 cm^{-1} Raman line with the background removed as a function of stage position (Figure 6-8b). It can be seen that the SERS enhancement is very uniform, with the standard deviation being only ~4% of the mean. The other Raman lines and the other regions of the SIOM metasurface also show similar results. We anticipate that the very high degree of uniformity of the SIOM metasurface would be advantageous for many applications.

6.6 Single Molecule SERS (SMSERS) using SIOM metasurface

The initial reports of single molecule SERS (SMSERS) [9, 10] garnered considerable interest, but the demonstration of a large area substrate with SMSERS sensitivity has proven elusive. Furthermore, previous reports of SMSERS have been performed almost entirely using aggregates of Ag colloidal nanoparticles that are very heterogeneous, with generally fewer than 1% being SMSERS-active [34]. Here, we demonstrate that our SIOM metasurfaces have SMSERS sensitivity. This is performed

the isotopologue method [35, 36]. We introduce two forms of Rhodamine 6G (R6G-d0 and R6G-d4) to the SIOM substrates at low concentration (0.2 nM). As discussed further below, this allows us to prove that the SERS spectra we then measure are predominantly from single molecules.

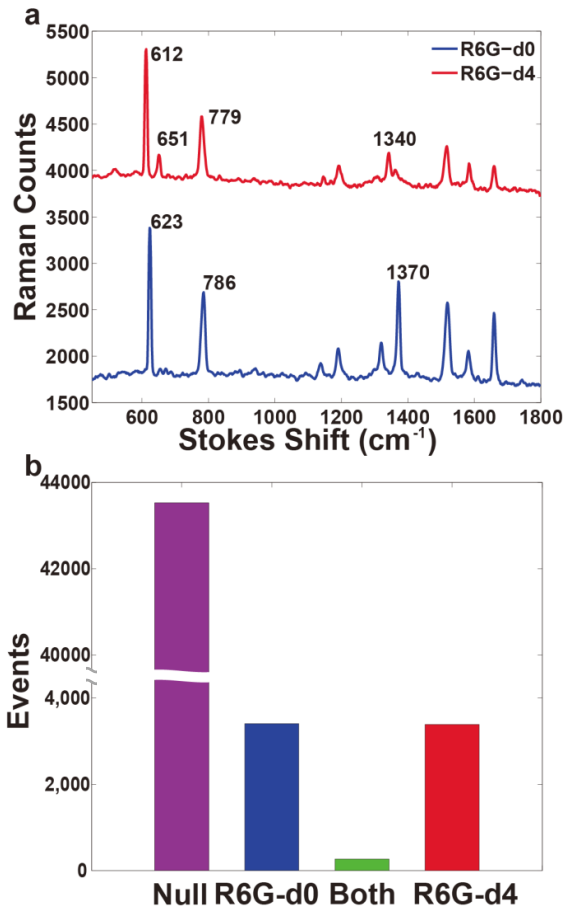

Figure 6-10. Experimental results of SMSERS on SIOM meatsurface. (a). Representative Raman spectra of R6G-d0 molecule and R6G-d4 molecule at single molecule level. R6G-d4 spectrum is shifted vertically by 2000 counts for display purposes. (b) Histogram of single molecule level events: null (purple), R6G-d0 molecule only (blue), both R6G-d0 and R6G-d4 molecules (green), and R6G-d4 molecule only (red).

The isotopologue method we use for verifying that SMSERS is achieved [35] employs two forms of Rhodamine 6G that differ only in the isotopic composition of their atoms, with the hydrogen atoms in R6G-d0 being replaced by deuterium atoms in R6G-

d4. The isotopologues adsorb to the metasurface with identical affinities, yet can be distinguished by shifts in their vibrational features. The Raman line of R6G-d0 at ~620 cm^{-1} shifts to ~610 cm^{-1} in R6G-d4, for example. This presents a means for determining whether a measured SERS spectrum originates from one or from both types of molecules. If the SMSERS regime has been achieved, and the SERS spectra are from predominantly single molecules, then these spectra should indicate the presence of chiefly one isotopologue (R6G-d0 or R6G-d4), with both types of molecules being simultaneously present only infrequently.

For the SMSERS measurement, the SIOM substrate is soaked in a solution containing the isotopologues R6G-d0 and R6G-d4 in methanol (0.2 nM each) for 12 hours, washed in methanol, then blown dry with nitrogen. The SIOM substrate is then scanned in the Raman microscope with a step size of 4 μm across an 896 × 896 μm region of SIOM metasurface. In the microscope, a laser beam (λ = 532 nm) is focused onto the substrate with a microscope objective (NA=0.9, magnification 100×). The laser power incident on the chip is 0.03 mW. The same objective lens is used to collect the Raman signal into a spectrometer equipped with CCD sensor. The integration time of acquiring the Raman spectrum for each scan position is 0.5 seconds. Measurements are made at 50625 stage positions, of which 7059 yield spectra that clearly contain Raman features. The criterion for a spectrum containing Raman features is that the height of the Raman peak (after background subtraction) is larger than the sum of the average value and one standard deviation. The average value and standard deviation are found from analysis of the spectra obtained at all 50625 stage positions. Representative spectra are included as Figure 6-10a. Each measured SERS spectrum is classified into one of three

categories: it contains no R6G features, or it contains only R6G-d0 features, or it contains only R6G-4 features, or it contains both R6G-d0 and d4 features. The results are shown as a histogram in Figure 6-10b. That the measured spectra contain features of both isotopologues simultaneously on an infrequent basis indicates that the SMSERS regime is achieved. This can be further quantified with a Poisson-binomial model[35]. The histogram of Figure 5b shows that the number of events with no molecules (null events), R6G-d0 only, both R6G-d0 and d4, and R6G-d4 events are in a ratio of 43566:3407:267:3385, i.e. a normalized ratio of ~163:12.8:1:12.7. From the SEM of the SIOM metasurface (Figure 6-1c), it can be seen that many nanoparticles would be within the laser spot employed in the SERS measurements. It is entirely possible, therefore, that within the laser spot, there are general several locations of the SIOM metasurfaces at which the enhancement is sufficiently strong so that SMSERS is possible. One may think of the union of these regions as the hot spot region. A Poisson-Binomial model with on average 0.15 molecules within the hot spot region predicts that 86.1% will contain no molecules, 6.7% will contain only R6G-d0 molecules, 6.7% will contain only R6G-d4 molecules, and 0.52% will contain both R6G-d0 and R6G-d4. Such a model would therefore predict that, for the 50625 measurement points, the numbers with no molecules, R6G-d0 only, both R6G-d0 and d4, and R6G-d4 only would be 43573:3394:264:3394, i.e. a normalized ratio of ~165:12.85:1:12.85. This is in very reasonable agreement with the experimentally-measured ratio, confirming the validity of the model. The model further predicts that the 6.7% of events containing only one isotopologue comprises 6.45% having solely one molecule, with the remaining 0.25% having two or more molecules. One may therefore conclude that ~96.3% of SERS spectra containing features of only one isotopologue

originate from a single molecule, with the remaining ~3.7% originating from two or more molecules.

6.7 Conclusions

In conclusion, we demonstrate a visible-wavelength metasurface that achieves near-total power absorption and exhibits single molecule sensitivity. Our SIOM metasurface consists of silver nanoparticle islands over a silver mirror, and is therefore readily fabricated on a wafer-scale using standard thin film depositions. The SIOM metasurface supports magnetic and electric resonances. These can be considered to generate effective electric and magnetic currents that generate far-fields that cancel, leading to zero reflection and complete absorption. We show that the spectral properties of the SIOM metasurface can be tuned by modifying its geometry via changing the fabrication parameters. As one might intuitively expect, the total absorption property is accompanied by very strong local field enhancement. We demonstrate that this is highly advantageous for SERS. Measurements show that our SIOM metasurfaces exhibit SERS enhancement factors that are more than one order of magnitude higher than those of silver nanoparticle islands on glass. The results also demonstrate a very high degree of uniformity over the SIOM substrate, with the standard deviation in SERS signal being only ~4% of the mean. We demonstrate that the high enhancement factor permits the detection of the Raman spectra of single molecules. Due to the uniformity of our SIOM substrate and its large area, we are able to present an unparalleled number (>7000) of single molecule events. We anticipate that, due to their high performance, large area, and low fabrication cost, SIOM metasurfaces could be highly appropriate for many applications in SERS, such as

food safety monitoring [37-39], explosive detection [40, 41], and pharmaceutical quality control [42, 43].

6.8 References

[1]. J. Hao, J. Wang, X. Liu, W. J. Padilla, L. Zhou, and M. Qiu, "High performance optical absorber based on a plasmonic metamaterial," Applied Physics Letters **96**, 251104-251103 (2010).
[2]. Y. Avitzour, Y. A. Urzhumov, and G. Shvets, "Wide-angle infrared absorber based on a negative-index plasmonic metamaterial," Physical Review B **79**, 045131 (2009).
[3]. N. Liu, M. Mesch, T. Weiss, M. Hentschel, and H. Giessen, "Infrared Perfect Absorber and Its Application As Plasmonic Sensor," Nano Letters **10**, 2342-2348 (2010).
[4]. C. Wu, B. Neuner, III, G. Shvets, J. John, A. Milder, B. Zollars, and S. Savoy, "Large-area wide-angle spectrally selective plasmonic absorber," Physical Review B **84**, 075102 (2011).
[5]. A. Tittl, P. Mai, R. Taubert, D. Dregely, N. Liu, and H. Giessen, "Palladium-Based Plasmonic Perfect Absorber in the Visible Wavelength Range and Its Application to Hydrogen Sensing," Nano Letters **11**, 4366-4369 (2011).
[6]. A. Moreau, C. Ciraci, J. J. Mock, R. T. Hill, Q. Wang, B. J. Wiley, A. Chilkoti, and D. R. Smith, "Controlled-reflectance surfaces with film-coupled colloidal nanoantennas," Nature **492**, 86-89 (2012).
[7]. M. Fleischmann, P. J. Hendra, and A. J. McQuillan, "Raman spectra of pyridine adsorbed at a silver electrode," Chemical Physics Letters **26**, 163-166 (1974).
[8]. D. L. Jeanmaire, and R. P. Van Duyne, "Surface raman spectroelectrochemistry: Part I. Heterocyclic, aromatic, and aliphatic amines adsorbed on the anodized silver electrode," Journal of Electroanalytical Chemistry and Interfacial Electrochemistry **84**, 1-20 (1977).
[9]. S. Nie, and S. R. Emory, "Probing Single Molecules and Single Nanoparticles by Surface-Enhanced Raman Scattering," Science **275**, 1102-1106 (1997).
[10]. K. Kneipp, Y. Wang, H. Kneipp, L. T. Perelman, I. Itzkan, R. R. Dasari, and M. S. Feld, "Single Molecule Detection Using Surface-Enhanced Raman Scattering (SERS)," Physical Review Letters **78**, 1667-1670 (1997).
[11]. J. A. Kong, *Electromagnetic Wave Theory* (EMW, Cambridge, 2005).
[12]. P. B. Johnson, and R. W. Christy, "Optical Constants of the Noble Metals," Physical Review B **6**, 4370-4379 (1972).
[13]. G. Dayal, and S. A. Ramakrishna, "Design of highly absorbing metamaterials for Infrared frequencies," Opt. Express **20**, 17503-17508 (2012).
[14]. Y. Nishikawa, T. Nagasawa, K. Fujiwara, and M. Osawa, "Silver island films for surface-enhanced infrared absorption spectroscopy: effect of island morphology on the absorption enhancement," Vibrational Spectroscopy **6**, 43-53 (1993).
[15]. R. F. Aroca, D. J. Ross, and C. Domingo, "Surface-Enhanced Infrared Spectroscopy," Appl. Spectrosc. **58**, 324A-338A (2004).

[16]. Q. Wang, F. Song, C. Ming, H. Zhao, J. Liu, C. Zhang, S. Lin, and E. Y.-B. Pun, "Plasmonic-enhanced quantum efficiency of europium complex using annealed silver island films," J. Opt. Soc. Am. B **28**, 220-224 (2011).
[17]. P. Royer, J. P. Goudonnet, R. J. Warmack, and T. L. Ferrell, "Substrate effects on surface-plasmon spectra in metal-island films," Physical Review B **35**, 3753-3759 (1987).
[18]. G. Lévêque, and O. J. F. Martin, "Tunable composite nanoparticle for plasmonics," Opt. Lett. **31**, 2750-2752 (2006).
[19]. G. Lévêque, and O. J. F. Martin, "Optical interactions in a plasmonic particle coupled to a metallic film," Opt. Express **14**, 9971-9981 (2006).
[20]. K. B. Crozier, A. Sundaramurthy, G. S. Kino, and C. F. Quate, "Optical antennas: Resonators for local field enhancement," Journal of Applied Physics **94**, 4632-4642 (2003).
[21]. M. G. Banaee, and K. B. Crozier, "Gold nanorings as substrates for surface-enhanced Raman scattering," Opt. Lett. **35**, 760-762 (2010).
[22]. Y. Chu, M. G. Banaee, and K. B. Crozier, "Double-Resonance Plasmon Substrates for Surface-Enhanced Raman Scattering with Enhancement at Excitation and Stokes Frequencies," ACS Nano **4**, 2804-2810 (2010).
[23]. W. Zhu, M. G. Banaee, D. Wang, Y. Chu, and K. B. Crozier, "Lithographically Fabricated Optical Antennas with Gaps Well Below 10 nm," Small **7**, 1761-1766 (2011).
[24]. D. Wang, T. Yang, and K. B. Crozier, "Optical antennas integrated with concentric ring gratings: electric field enhancement and directional radiation," Opt. Express **19**, 2148-2157 (2011).
[25]. D. Wang, W. Zhu, Y. Chu, and K. B. Crozier, "High Directivity Optical Antenna Substrates for Surface Enhanced Raman Scattering," Advanced Materials **24**, 4376-4380 (2012).
[26]. T. J. Seok, A. Jamshidi, M. Kim, S. Dhuey, A. Lakhani, H. Choo, P. J. Schuck, S. Cabrini, A. M. Schwartzberg, J. Bokor, E. Yablonovitch, and M. C. Wu, "Radiation Engineering of Optical Antennas for Maximum Field Enhancement," Nano Letters **11**, 2606-2610 (2011).
[27]. E. J. Smythe, M. D. Dickey, J. Bao, G. M. Whitesides, and F. Capasso, "Optical Antenna Arrays on a Fiber Facet for in Situ Surface-Enhanced Raman Scattering Detection," Nano Letters **9**, 1132-1138 (2009).
[28]. W. Zhang, H. Fischer, T. Schmid, R. Zenobi, and O. J. F. Martin, "Mode-Selective Surface-Enhanced Raman Spectroscopy Using Nanofabricated Plasmonic Dipole Antennas," The Journal of Physical Chemistry C **113**, 14672-14675 (2009).
[29]. K. B. Biggs, J. P. Camden, J. N. Anker, and R. P. V. Duyne, "Surface-Enhanced Raman Spectroscopy of Benzenethiol Adsorbed from the Gas Phase onto Silver Film over Nanosphere Surfaces: Determination of the Sticking Probability and Detection Limit Time†," The Journal of Physical Chemistry A **113**, 4581-4586 (2009).
[30]. A. D. Ormonde, E. C. M. Hicks, J. Castillo, and R. P. Van Duyne, "Nanosphere Lithography: Fabrication of Large-Area Ag Nanoparticle Arrays by Convective Self-Assembly and Their Characterization by Scanning UV−Visible Extinction Spectroscopy," Langmuir **20**, 6927-6931 (2004).
[31]. J. B. Jackson, S. L. Westcott, L. R. Hirsch, J. L. West, and N. J. Halas, "Controlling the surface enhanced Raman effect via the nanoshell geometry," Applied Physics Letters **82**, 257-259 (2003).

[32]. A. Ahmed, and R. Gordon, "Directivity Enhanced Raman Spectroscopy Using Nanoantennas," Nano Letters **11**, 1800-1803 (2011).
[33]. A. D. McFarland, M. A. Young, J. A. Dieringer, and R. P. Van Duyne, "Wavelength-Scanned Surface-Enhanced Raman Excitation Spectroscopy," The Journal of Physical Chemistry B **109**, 11279-11285 (2005).
[34]. J. P. Camden, J. A. Dieringer, Y. Wang, D. J. Masiello, L. D. Marks, G. C. Schatz, and R. P. Van Duyne, "Probing the Structure of Single-Molecule Surface-Enhanced Raman Scattering Hot Spots," Journal of the American Chemical Society **130**, 12616-12617 (2008).
[35]. J. A. Dieringer, R. B. Lettan, K. A. Scheidt, and R. P. Van Duyne, "A Frequency Domain Existence Proof of Single-Molecule Surface-Enhanced Raman Spectroscopy," Journal of the American Chemical Society **129**, 16249-16256 (2007).
[36]. S. L. Kleinman, E. Ringe, N. Valley, K. L. Wustholz, E. Phillips, K. A. Scheidt, G. C. Schatz, and R. P. Van Duyne, "Single-Molecule Surface-Enhanced Raman Spectroscopy of Crystal Violet Isotopologues: Theory and Experiment," Journal of the American Chemical Society **133**, 4115-4122 (2011).
[37]. Y. Liu, K. Chao, M. S. Kim, D. Tuschel, O. Olkhovyk, and R. J. Priore, "Potential of Raman Spectroscopy and Imaging Methods for Rapid and Routine Screening of the Presence of Melamine in Animal Feed and Foods," Appl. Spectrosc. **63**, 477-480 (2009).
[38]. L. He, *Application of Surface Enhanced Raman Spectroscopy to Food Safety Issues* (BiblioBazaar, 2012).
[39]. J. Qin, K. Chao, and M. Kim, "Raman chemical imaging system for food safety and quality inspection," Transactions of the ASABE **53**, 1873-1882 (2010).
[40]. C. Cheng, Z. Li, W. Liu, and J. Wu, "Stand-Off Explosives Detection Based on Raman Spectroscopy," CORD Conference Proceedings, 1-4 (2010).
[41]. E. L. Izake, "Forensic and homeland security applications of modern portable Raman spectroscopy," Forensic science international **202**, 1-8 (2010).
[42]. T. Vankeirsbilck, A. Vercauteren, W. Baeyens, G. Van der Weken, F. Verpoort, G. Vergote, and J. P. Remon, "Applications of Raman spectroscopy in pharmaceutical analysis," TrAC Trends in Analytical Chemistry **21**, 869-877 (2002).
[43]. S. Wartewig, and R. H. Neubert, "Pharmaceutical applications of Mid-IR and Raman spectroscopy," Advanced Drug Delivery Reviews **57**, 1144-1170 (2005).